UNIVERSIDAD NACIONAL AUTÓNOMA DE MÉXICO
PROGRAMA DE MAESTRÍA Y DOCTORADO EN INGENIERÍA
INGENIERÍA ELÉCTRICA - SISTEMAS ELÉCTRICOS DE POTENCIA

**MODELADO Y SIMULACION DE GENERACIÓN DISTRIBUIDA
USANDO SISTEMAS HIBRIDOS**

TESIS PARA OPTAR POR EL GRADO DE
DOCTORA EN INGENIERÍA

PRESENTA:
MARIA FERNANDA ALVAREZ MENDOZA

TUTOR PRINCIPAL
DR. CÉSAR ANGELES CAMACHO, INSTITUTO DE INGENIERÍA, UNAM
COMITÉ TUTOR
DR. PAUL ROLANDO MAYA ORTIZ, FACULTAD DE INGENIERÍA, UNAM
DR. CLAUDIO RUBÉN FUERTE ESQUIVEL, FACULTAD DE INGENIERÍA ELÉCTRICA, UMSNH
DR. HENRIK MADSEN, DTU COMPUTE, DTU
DR. JOSÉ JUAN MANUEL RAMÍREZ ARREDONDO, CINVESTAV

CIUDAD DE MÉXICO, MÉXICO. DICIEMBRE 2017

UNIVERSIDAD NACIONAL AUTÓNOMA DE MÉXICO
MASTER AND DOCTORATE PROGRAM IN ENGINEERING
ELECTRIC ENGINEER - POWER ELECTRIC SYSTEMS

**DISTRIBUTED GENERATION MODELING AND SIMULATION
IMPLEMENTING HYBRID SYSTEMS**

DISSERTATION IN FULFILLMENT OF THE REQUIREMENTS
FOR THE DEGREE OF
DOCTOR OF PHILOSOPHY IN ENGINEER

PRESENTED BY:
MARIA FERNANDA ALVAREZ MENDOZA

THESIS ADVISOR
DR. CÉSAR ANGELES CAMACHO, II-UNAM

COMMITTEE MEMBERS
DR. PAUL ROLANDO MAYA ORTIZ, FACULTAD DE INGENIERÍA, UNAM
DR. CLAUDIO RUBÉN FUERTE ESQUIVEL, FACULTAD DE INGENIERÍA ELÉCTRICA, UMSNH
DR. HENRIK MADSEN, DTU COMPUTE, DTU
DR. JOSÉ JUAN MANUEL RAMÍREZ ARREDONDO, CINVESTAV

MEXICO CITY, MEXICO. DECEMBER 2017

COMMITTEE MEMBERS:

President   Dr. PAUL ROLANDO MAYA ORTIZ
Secretary   Dr. CLAUDIO RUBÉN FUERTE ESQUIVEL
1st vocal   Dr. CÉSAR ÁNGELES CAMACHO
2nd vocal   Dr. HENRIK MADSEN
3rd vocal   Dr. JOSÉ JUAN MANUEL RAMÍREZ ARREDONDO

This dissertation was made in the Engineering Institute, UNAM.

THESIS ADVISOR:

Dr. César Angeles Camacho

_____
Signature

Abstract

Generation technologies within everyone's reach have provoked a change from the hierarchical central generation, into a decentralized one through distributed generation (DG); mostly based on renewable energy sources (RES). As is known, distributed resources (DR) impacts voltage and frequency, and deviations out of tolerance limits are financial damage to the customers. This research, propose an energy management system (EMS) with several approaches to overcome intermittence and create a semi-dispatchable generation supply. The EMS, considers the grid code and the possibility to optimize the power factor at the point of common coupling (PCC), without disturbing the frequency of the network.

The power generation model is a hybrid system based on wind power, solar power and fuel-cell hydrogen technologies. Stochastic models provides probabilistic information of short-term forecast applied to wind speed and radiation, integrated to know the one hour-ahead wind and photovoltaic power generation, and in consequence the output power generation by the hybrid system. The EMS are modelled by applying time series analysis through the root mean square algorithm with forgetting factor and by using model predictive control to integrate the system. This study uses historic wind speed data from Mexico City and loads curves based on average households and mini-store on a daily basis. The behavior of a 13 node IEEE distribution test network with several EMSs connected as distributed generation is shown.

The effectiveness of the proposed EMS, is tested by mass connecting them as distributed generation in a test distribution network. Results shows the power dispatch of each generation developed, the general behavior of the network with embedded generation and compare the final results with the obtained ones from the same grid with centralized generation. Study cases and obtained results at each development stage are presented and analyzed. Results show that time series analysis improve the efficiency of EMS when connected as distributed generation. The developed models, allows a flexible sources integration, avoiding disturbing the distribution network at connection point. Furthermore, the implementation of the developed approaches management systems improve power factor, voltage magnitude and power losses as observed and analyzed. Also is to consider that the grid frequency will not be disturbed as consequence of sudden generation power changes.

Resumen

Las tecnologías de generación al alcance de todos han provocado un cambio en la jerarquía de generación central a una descentralizada, a través de la generación distribuida (DG); basado principalmente en fuentes de energía renovables (RES). Como es sabido, los recursos distribuidos (DR) afectan el voltaje y la frecuencia, y desviaciones fuera de los límites de tolerancia afectan financieramente a los clientes. Esta investigación, propone un sistema de gestión energética (EMS) con varios enfoques para superar la intermitencia y crear un suministro de generación semi-despachable. El EMS considera el código de la red y la posibilidad de optimizar el factor de potencia en el punto de acoplamiento (PCC), sin alterar la frecuencia de la red.

El modelo de generación de potencia propuesto, es un sistema híbrido basado en energía eólica, energía solar y tecnologías de hidrógeno de celda de combustible. Los modelos estocásticos proporcionan información probabilística de predicción a corto plazo de la velocidad del viento y radiación solar, integrados para conocer la generación de potencia eólica y fotovoltaica con una hora de anticipación, y en consecuencia, la generación de potencia del sistema híbrido. El EMS se modela aplicando análisis de series de tiempo a través del algoritmo de la media cuadrática con factor de olvido, y utilizando modelado de control predictivo para integrar el sistema. Este estudio utiliza datos históricos de la velocidad del viento y radiación solar de la Ciudad de México y curvas de demanda diaria basadas en hogares promedio y mini-tiendas. Se muestra el comportamiento de una red de prueba de distribución de IEEE de 13 nodos con varios EMS conectados como generación distribuida.

La efectividad del EMS propuesto se comprueba mediante la conexión masiva de dicho EMS como generación distribuida en una red de distribución de prueba. Los resultados muestran el despacho de energía de cada sistema híbrido, el comportamiento general de la red con generación incorporada y se comparan los resultados finales con los obtenidos en cada fase de desarrollo de la misma grilla con generación centralizada. Se presentan y analizan los casos de estudio y los resultados obtenidos en cada etapa de desarrollo del sistema de gestión energética. Los resultados muestran que el análisis de series de tiempo mejora la eficiencia del EMS cuando está conectado como generación distribuida. Los modelos desarrollados, permiten una integración flexible de fuentes de generación, evitando perturbar la red de distribución en el punto de conexión. Además, la implementación de los enfoques de sistema de gestión desarrollados, mejora el factor de potencia, la magnitud del voltaje y las pérdidas de potencia, así como se puede observar y analizar en los resultados obtenidos. También se debe tener en cuenta que la frecuencia de la red no se verá afectada como consecuencia de cambios bruscos en la potencia de generación.

Dedication

To my parents and sister *for their unconditional support, for encouraging me to keep going with my decisions and for the great moments given to me.*

To my co-workers and friends *for their friendship and good times.*

Acknowledgement

To Dr. César Angeles Camacho for his support and guidance.

To the National Autonomous University of Mexico for the means given to make this possible.

To the National council of science and technology CONACYT, for the financial support through doctoral grant CVU 595035.

Table of Contents

List of figures

List of tables

Nomenclature

Overhead line

δ Penetration depth in meters

ϵ Permittivity

ϵ_0 Permittivity of free space

ϵ_r Relative permittivity of the medium

$\hat{P}_{ii}$ Self-potential coefficients

$\hat{P}_{ij}$ Mutual potential coefficients

λ_{in} Flux linking conductor i and n in [Wb-t/m]

μ_0 absolute permeability = $4\pi \cdot 10^{-7}$ in H/m

σ Earth conductivity in Siemens

C_{abc} Phase capacitance

D_e Equivalent depth of the fictitious return path of the earth current

D_{in} Distance between conductors i and n in meters

d_{kl} Horizontal distance between the k-th and the l-th conductors in meters

D_{ni} Distance between conductors n and i in meters

f Frequency in Hz

GMR_i Geometric mean radius of conductor i in meters

h_k Height of the k-th conductor above ground in meters

L_{in} Inductance of between conductor i and n in [H/m]

N_{in} Incidence matrix

P_{abc} Phase potential coefficient

q_n Charge density on conductor n in cb/m

R_k Conductor resistance in [Ω/m]

RD_n Radius of conductor n in meters

S_{ii} Distance between conductor i and its own image

S_{ij} Distance between conductor i and image of conductor j

V_{ig} Voltage drop between i and ground

V_{ij} Voltage drop between conductors i and j

Y_{bus} Bus admittance matrix

Y_{shunt} Shunt admittance

Z_m Mutual impedance in [Ω/m]

Z_s Series impedance in [Ω/m]

Underground cable

C_{pg} Capacitance from phase to ground

d_c Phase conductor diameter

d_s Diameter of shielding

D_{ij} Distance between i and j

D_{nm} Center-to-center distance between phase conductors

d_{od} Nominal diameter

GMR_c Conductor's geometric mean radio

GMR_s Neutral strand geometric mean radio

GMR_{cn} Geometric mean radio of concentric neutral

k_s Number of concentric neutral strands

R_b Radius of a circle passing through the centers of the neutral strands

r_c Conductor resistance

r_s Resistance of a solid neutral strand

r_{shield} Shield resistance of a tape-shielded cable

T_c Thickness of the copper tape shield

z_{ii} Self-impedance

z_{ij} Mutual-impedance

Transformer

C Transformer matrix connection

E_H Rated voltages on side HV

E_L Rated voltages on side LV

HV High voltage side

kVA Rated power in VA

LV Low voltage side

N_H number of turns of HV winding

N_L number of turns of HL winding

N_{HL} Transformation relation

RT Percentage of impedance

t_{HL} Transformation relation in per unit

XT Percentage of reactance

Y_m Mutual admittance between windings

Y_{nodal} Nodal admittance matrix

Y_{prim} Primitive admittance matrix

Y_p Self-admittance of primary winding

Y_s Self-admittance of secondary winding

Z_H Winding impedance

Zb_H Primary nominal base impedance

Zb_L Secondary nominal base impedance

Power flow

ΔP_A Active power mismatch at phase A

ΔQ_A Reactive power mismatch at phase A

P_{Aa} Active power transmitted from A to a

P_D^A Active power drawn by the load at A

P_g^A Active power injected by the generator at phase A

Q_{Aa} Reactive power transmitted from A to a

Q_D^A Reactive power drawn by the load at A

Q_g^A Reactive power injected by the generator at phase A

Forecast

Δt Age of the data

λ Forgetting factor

μ Correction for the mean value

ω Weight

Θ Weight of past observations

θ Vector of weight of past observations

ε White noise

X Matrix of past observations

Y_{t+1} Forecast one step ahead

Y_t Historic data

Wind turbine

ρ Air density

P Active power

V Voltage

V_w Wind speed

Electrolyzer

F	Faraday constant
H	Hydrogen
I	Electric current
O	Oxygen
p	Ambient pressure
P_{el}	Electrolyzer power
R	Ideal gas constant
T	Temperature
t	time
V_g	Gas volume
V_{H_2}	Volume of hydrogen
z	Number of excess electrons

Fuel cell

E	Open circuit voltage
H_{2used}	Volume of hydrogen required by the fuel cell
n	Number of cells
P_{fc}	Fuel cell power
V_c	Cell voltage
V_{act}	Activation voltage
V_{ohm}	Ohmic voltage
V_{trans}	Transport voltage

Hybrid system setup and predictive control

M	Number of points in average filter
N	Future outputs for a horizon
P_{t+k}^{ref}	Power reference trajectory
P_{elmax}	Activation vector of electrolyzer
P_{fcmax}	Activation vector of FC

Forecast and MPC implementation

Γ_{el}	Threshold of low level percent of storage
Γ_{fc}	Threshold of min percent of storage for FC
φ	Storage level
φ_0	Last value of storage level

φ_{max} Max limit of storage

φ_{min} Min limit of storage

l_{el} Impulse response of electrolyzer

l_{fc} Impulse response of FC

l_{st} Impulse response of storage

P_{el}^{nom} Electrolyzer nominal power

P_{fc}^{nom} Fuel cell nominal power

P_{t+k}^{w} Forecasted wind power

P_o Balance power in HS

P_w Actual + Forecasted wind power

P_{φ} Power flow to/from storage elements

Acronyms

AC	Alternating current
ACF	Autocorrelation function
AEMS	Advance energy management system
AR	Autoregressive
CSP	concentrated solar power
CFE	Comisión Federal de Electricidad (Federal Electricity Commission)
DC	Direct current
DG	Distributed generation
DER	Distributed energy resource
DR	Distributed resource
EMS	Energy management system
ESD	Energy storage device
ESS	Energy storage system
FC	Fuel cell
GHGs	Greenhouse gases
GMR	Geometric mean radio
HS	Hybrid system
SO	System operator
KCL	Kirchhoff's current law
KVL	Kirchhoff's voltage law
MPC	Model predictive control
MPP	maximum power point
N-R	Newton-Raphson
PCC	Point of common coupling
PEMFC	Proton exchange membrane fuel cell
PF	Power factor
PV	Photovoltaic
RES	Renewable energy sources
RLS	Recursive least square
SWT	Small wind turbine
URD	Underground residential distribution
VSC	Voltage-source converter
WT	Wind turbine

CHAPTER 1

INTRODUCTION

1.1 Introduction

New tendencies in current environmental education are addressed to sustainable development by establishing environmental protection standards. In this framework, new technologies for power generation with zero or very low pollutant levels have been developed based on renewable energies. Renewable generation presented as hybrid systems (HS), are implemented to improve the efficiency of individual generation technologies by complementing each other. Because of renewable generation characteristics like size, cost, resource, etc., and development of energy management systems (EMS), consumers are starting to integrate into the electric market. Consumers are taking a prosumer role, empowering them to gain greater control over their electric consumption and power generation through small wind turbines (SWT), photovoltaic (PV) panel arrangement, storage system, and other technologies; supporting the environmental awareness. As a result, the electric generation trend is changing from a hierarchical way of central generation, in which electric networks are operated and controlled; to a distributed way. This has resulted in an increasing need for modeling and simulating HS connected as distributed generation to explore and mitigate its technical impact into the distribution networks.

The hybrid system by definition contains a combination of two or more power generation both renewables and/or based on fossil fuel. The mixture of renewable energy sources improves the system efficiency and availability of the energy supply. Hybrid energy systems go from small systems designs, which supply one or many households, to very large isolated networks. Generally, these are implemented in distant areas, isolated of large centralized networks; every day, they are more common as distributed generation (DG), changing the way that the network is designed and operated.

When renewable energy sources (RES) are integrated into a network, intermittency is a challenge to overcome in electric generation, been this the case of wind and photovoltaic power. In this context, initially, this research proposes a hybrid system as an approach to overcome the volatility of wind power, with no frequency disturbance to the network at the connection point, by employing storage technology, forecasts, and model predictive control (MPC) algorithms. Two proposed hybrid systems, suitable for distributed generation are used in the present research. The first one consists of a small wind turbine (SWT), an electrolyzer, hydrogen storage and a polymer electrolyte membrane fuel cell (PEMFC), which are embedded in one complete system. The second one adds a small photovoltaic power plant. It is important to notice that the HS model is a modular one and can be built-up using different kind and sizes of renewable generators.

Both HS proposed, when connected to the distribution grid within the local load, can emulate a prosumer systems, which can supply or sink power from the grid. The prosumer systems are typically located at the user's sites where the energy generated is fed into the local distribution grid or self-consumed, but their integration with the local distribution network poses a challenge for the system operators (SO). Considering the consumers' point of view in the actual trend and focusing on the prosumer needs, a prosumer EMS is proposed here, adopting two different approaches suitable for distributed generation; first a management subjected to a designated value approach, and second, a prosumer method for demand-side management. The prosumer EMS's are integrated by an SWT, a PV array, a PEMFC, an electrolyzer and a storage system. These approaches, were developed with a power factor correction respond at the connection point and zero frequency disturbance considering the grid code; furthermore, allows the user to have visibility into and control over the energy use and performance of individual equipment, creating opportunities for energy and capital expenditure savings.

The system is configured to be installed hypothetically in the City of Mexico, for the simulation, it uses historic wind speed and radiation data from Mexico City; the forecasts are obtained using the recursive least square algorithm with a forgetting factor. The proposed approaches provide probabilistic information for short-term wind and PV power generation and electric generation as the outcome of the systems. A method for a semi-dispatchable electric generation based on time series analysis is presented and the power models controlled by MPC.

Once the models developed are coded and results validated, the technical impact of distributed generation on the grid is analyzed considering the approaches proposed here, as well as the conditions established by the Mexican grid code. Several distribution networks with different condition and sizes have been simulated in the three-phase frame-of-reference. Also, networks with several HS as a distributed generation has been simulated. Results from the different cases of study shown the advantage of HS with an EMS system as the controller, to appreciate the advantage level on the grid with and without the implementation of the proposed approaches.

As far as the author of this research is aware, a project of this type has not been done. Certainly there are a number of isolated projects and much information about levelized costs, but the technical side and the effects of distributed generation into the distribution network have not been studied in great depth.

1.2 Background

Distribution networks have many technical problems derived from the increasing integration of DG, there have been studies like [1] which describes modern wind power systems, and connection requirements of a wind turbine, also discuss the possible control methods for wind turbines to meet the required specifications. The problems produced by large-scale DG are given because of DG introduces "meshed" power flows that interfere with the effectiveness of standard voltage regulation [2]. In [3] a methodology has been proposed for optimally allocating wind-based DG units in the distribution system to minimize annual energy loss. It is demonstrated on isolated power systems that by injecting power within instants after the loss of a generating unit, can backup conventional generation assets during the activation of their primary reserve [4]; where results show that fast-acting storage, can mitigate the impact of these sources on the dynamic performance.

So far, many studies have demonstrated the noticeable issues expected from DG like voltage, angle and frequency stability as in [5], [6], where one of the issues was the imbalances expected in networks with DG. Another issue presented in [7], was the frequency stability in isolated systems where it becomes a significant concern. Other studies focus on the stability problems of grid-connected inverters as [8], where complex controllers (e.g., multiple rotating dq-frames or resonant- based) are often required to compensate low-frequency grid voltage background distortion, and an LCL-filter is usually adopted for the high frequency one.

Some studies have identified the need of reserves as in [9], arguing that prediction errors for consumption or production by distributed generation will require energy reserves; also a shortage in production in the synchronous system (e.g., due to the loss of another generator) will immediately result in a drop in frequency; at the same time in [9], it is said that distributed generation and load may actually have advantages compared to large conventional power stations for maintaining primary reserve.

Recently, a wide variety of studies have been performed on optimal energy management in renewables energy systems. The literature on optimal semi-dispatchable management applied to hybrid systems as DG is still lacking. However, several works analyze the integration of energy systems with storage for energy management dispatchability during peak demand [10]. Many energy management approaches use energy storage system (ESS) for concentrated solar power (CSP) to shift the generation to hours with high energy prices as in [11].

DG with a demand-side management strategy has a direct impact in the electricity consumption as seen in [12], without considering low voltage at the point of common coupling (PCC); with this problematic in mind, [13] evaluates three different compensators for a close-loop PCC voltage controller, mainly with reactive power compensation. Furthermore, optimization strategies carried out on a hybrid system still consider the need for fossil power plants [14], [15].

For energy management in renewables, intermittency is a challenge to overcome, and a way to deal with it, is to combine renewable power generation with forecast, in order to plan more accurately the energy management and participation in market regulation like in [16], [17]. In other studies, a fast-acting storage in the distribution network has been implemented, like in [4]. Most systems have in common the use of different storage technologies; an ESS has been proposed for reducing the variability in [18], in which the design of a supercapacitor required as ESS for a wind farm, through a statistical approach is proposed, implementing optimistic random wind power input.

Wind power uncertainty has been a research topic as in [19], where wind power forecast uncertainty is investigated in the operation schedule of the generating units, also called unit commitment. Forecasting has become more widely used as a tool to facilitate the fluctuating generation integration into electric power systems. Many studies are focused on modeling wind power forecast, where different models using ARMA, artificial neural networks and fuzzy logic models are explained [20], [21] and compared [22] . Others focus on solar radiation forecast using the three solar components (beam, diffuse and global) as in [23], and using a set of forecasts instead of a single forecast [24] are developed.

1.3 Research motivation

The actual policies for low pollutant generation technologies, the development of more efficient and lower cost of renewable generation devices, has made the final users to take part in the electric sector as prosumer at distribution network. However, the use of renewable energy as a primary source, has the intermittence as the natural disadvantage of the generated power in many occasions, depending on the renewable resource employed and the first characteristic required to be improved. Moreover, acknowledging that the distribution network was not meant to have generation; all of this has created the need for investigating the impact of clean generation technologies on the behavior and operation of the distributions grids.

The performance of a HS derives from the separate behavior of the generator systems involved; they are coupled to cover the innate separately deficiencies. The modeling and simulation of HS to mitigate energy sources intermittence by means of forecast algorithms, alongside modular power generation models aimed to prosumr needs, acknowledging grid code, no frequency disturbance, and power factor stability at the point of common coupling is required.

Hybrid systems operation required the implementation of EMS as the controller to integrate into a more efficient way the of clean generation technologies as a DG in the grid.

On the other hand, the integration of alternative generation at the distribution network implies disturbance to the frequency and the daily load curve in the grid management, mainly caused by the uncertainty of the energy sources such as wind and sun, being these the popular ones. This problem is complicated by the relationship between intermittence sources and stability, more explicitly the active power-frequency relationship. This problem is complicated by the relationship between intermittence sources and stability, more explicitly the active power-frequency relationship. Making clear the need to research the impact of mass DG integration to the net, with EMS that regard their disturbance in the grid.

The motivation of this research is the need of a tool to research the impact of mass DG integration to the net, with an EMS that regard their disturbance in the grid. The tool is based on a modular way to couple different renewable technologies in a HS. To contribute in a more efficient way to the mitigation of the disturbance, the tool is equipped with forecast algorithm for renewable energies.

Note that the hybrid models, having different types of power generators based on renewable energy with forecast method integration, open the doors to find new research areas.

1.4 Problem statement

The need to generate more electricity at the same rate as population growth is clear; the implementation of new technologies and new forms of renewable energy generation presents a challenge for conventional networks that must show their compatibility with the new technologies. Concluding in a shortage of future power grid analysis.

The lack of energy management algorithms for renewable generation technologies that consider grid code policies, as to not disturb net frequency and support power factor stability at the connection point; alongside, the impact of mass HS embedded as DG in the grid, is one of the needs

that will be addressed as part of this doctoral research project. Considering short-term forecast implementation as to inform the hour prior power generation to the SO, and the flexibility of the algorithm to interact with different generation and storage technologies.

1.5   Hypothesis

It is well known that the operation of conventional distribution networks can be affected by the incorporation of distributed generation based on renewable energies, based on this two hypothesis come out on this project,

Prosumer management systems used alongside HS, may mitigate the adverse impact of renewables energies integrated into distribution network and even improve the grid behavior.

The forecast of renewable energies could improve the design of hybrid systems to mitigate the disturbances created by renewable energies, and even convert non-dispatchable into semi-dispatchable power generation.

1.6   Objectives of the research

1.6.1 Main objective

Conduct research on the steady-state impact of massive integration of distributed renewable generation into distribution networks considering forecast and applying an energy management to hybrid systems. In this research project, an aspect of paramount importance is the development of a modular based tool to overcome renewable energy intermittency, to obtain semi-dispatchable generation with zero frequency disturbance and power factor improvement at the connection point.

1.6.2 Specific objectives

- Renewable generation modeling of a small wind turbine, photovoltaic panel, and PEMFC, alongside electrolyzer hydrogen generation.

- Development and coding of wind speed and radiation forecast algorithm.

- Modeling small generation of wind and photovoltaic, implementing the previous developed wind and radiation forecast algorithms.

- Development and coding a prosumer energy management system algorithm for HS, integrating renewable generation models with hydrogen storage.

- Development of a multiphase continuous power flow analysis software for unbalanced distribution networks, implementing overhead lines, underground cables and transformer models.

- Validate the models created through commercial software to the possible extent.

- Implementation of prosumer EMS proposed approaches as mass distributed generation in an unbalanced distribution network, using real historic household and mini-store load data.

- Analysis and discussion of results at different research stages: i) intermittence mitigation and semi-dispatchable HS output power. ii) Prosumer energy management systems. iii) Impact of developed algorithms into a distribution network when connected in high volume as DG.

1.7 Dissertation achievements

A forecast algorithm was developed based on time series analysis to generate a stochastic wind power model. Historic data from meteorology stations, which was collected from the automatic stations of the Mexican national weather system located in Mexico City were used to obtain a wind power model and validate the algorithm. Furthermore, to recreate the output power of a wind-FC HS, a smooth algorithm was developed like a first approach, by means of the forecasted power, to remove the intermittence contained in the wind power, aimed to be implemented in the energy management algorithm through MPC. The MPC is programmed and used for several operational modes of the HS, one of these functions is to generate its power trajectory taking into account the relation active power – power factor, instead of smoothing the power supplied. At this point, it was achieved HS power semi-dispatchability and at the same time, no frequency disturbance in the distribution network if the HS is to be connected as distributed generation.

Additionally, a simple PV model was built, validated and implemented alongside a forecast model for radiation, to recreate a PV stochastic model. The PV stochastic model was merged with the initial HS to form a generation system with a better response.

Afterwards, a prosumer EMS was generated using model predictive control. A cost function was deduced representing the inside energy management of the HS. The MPC implements the developed stochastic wind and radiation power models, FC model, electrolyzer model and hydrogen storage with smoothing characteristics integrated into the algorithm, recreating a prosumer HS. The prosumer algorithm was developed adopting two approaches, i) considering the grid code, zero frequency disturbance and with a power factor correction respond, and ii) a prosumer method for demand-side management. The prosumer algorithm was applied in study cases to test and to analyze the respond with different energy management priorities.

Separately, the multiphase power flow program to compute continuous power flow analysis was developed using MATLAB ®. At this stage, the multiphase power flow with an incorporation of different generations was validated with the commercial program NEPLAN ®. The continuous power flow software is deduced by Newton-Raphson (N-R) method. The overhead line model considers the physical characteristics of distribution lines as distances between cables taking into account the pole configuration, radio, resistance, geometric mean radio (GMR), and type of conductor and line length. Once the three-phase line was accomplished, the two- and single-phase line model including the self and mutual inductance and disposition (the distance of physical configuration) of the line is deduced. The multiphase overhead line models were incorporated into the algorithm, to achieve a multiphase power flow program. From here, the underground cable modeling for a distribution network was developed, taking into account the physical

characteristics, type of cable and layout setup. The transformers modeled for the different connections: Delta-Delta, Delta-Wye, Wye-Delta and Wye-Wye, and implemented on the power flow.

Finally, the different semi-dispatchable prosumer systems proposed are coupled in high volume as distributed generation into a test network to study the actual impact in a distribution network, considering households and mini-stores load curves. A study case is recreated with the purpose to show the respond of the developed generation approaches.

The findings from this dissertation were documented and published as observed in next Section.

1.8   Publications

1.8.1   Journals

- **Alvarez-Mendoza F.**, Bacher P., Madsen H. and Angeles-Camacho C., "Stochastic model of wind-fuel cell for a semi-dispatchable power generation", *Applied Energy*, Vol. 193, 1 May 2017, pp. 139–148. ELSEVIER SCI. ISNN 0306-2619. doi: http://dx.doi.org/10.1016/j.apenergy.2017.02.033.

- Suarez-Velazquez G., Angeles-Camacho C., **Alvarez-Mendoza F.** and Acha E., "On the modeling of grid-connected fuel cell generator and their impact on low-voltage AC microgrids", *Journal of Modern Power Systems and Clean Energy*, (Submitted). MPCE. ISNN 2196-5420.

- **Alvarez-Mendoza F.**, Bacher P., Angeles-Camacho C. & Madsen H., "Semi-Dispatchable Generation with Wind-Photovoltaic-Fuel Cell Hybrid System to Reduce Frequency Disturbance", *Electric Power Systems Research Journal*, (Submitted), 2017. ISSN: 0378-7796.

- **Alvarez-Mendoza F.**, & Angeles-Camacho C., "Hybrid system generator for prosumer into smart-grid", (In process), 2017.

1.8.2   Congresses and Conferences

- **Alvarez-Mendoza F.**, Bacher P., Angeles-Camacho C. and Madsen H., "Advanced Energy Management to Avoid Power Uncertainty and Frequency Affectation from Hybrid Systems", WWEC 2017, 16th World Wind Energy Conference & Renewable Energy Exhibition. Sweden, June 2017.

- **Alvarez-Mendoza, F.**, Bacher, P., Angeles-Camacho, C. and Madsen, H., "Semi-Dispatchable Generation with Wind-Photovoltaic-Fuel Cell Hybrid System to Reduce Frequency Affectation," in Conference proceedings. International Conference & Workshop REMOO-2017. Energy for Tomorrow, 2017, pp. 536–548, Venice, Italy, 2017. ISBN: 978-3-9818275-5-2.

- Mejia, A., Mestizo-Lopez, A., **Alvarez-Mendoza, F.** and Angeles-Camacho, C., "Voltage Stability Analysis of the Electric Grid with DFIG Wind Farm Equivalent Integrated", WWEC 2015, 14th World Wind Energy Conference & Renewable Energy Exhibition. Israel, October 2015.

- **Alvarez-Mendoza, F.** and Angeles-Camacho, C., "Advanced Model of a Wind-Hydrogen System with Integrated Fuel Cell", WWEC 2014, 13th World Wind Energy Conference & Renewable Energy Exhibition and 8th China (Shanghai) International Wind Energy Exhibition. China, April 2014.

1.9   Thesis structure

This thesis is structured in a step-by-step way for a better understanding of the reader. First, the purpose of this research is explained including the problematic, objectives, and achievements. The second chapter shows the development of an advanced energy management system (AEMS) model with semi-dispatchable generation employing an accomplished forecast algorithm with smoothing operation mode; the chapter explains the models implemented for forecast, wind power generation, electrolyzer model and fuel cell model. In the third chapter, a prosumer management system is proposed implementing SWT, PV, PEMFC, electrolyzer and hydrogen storage through MPC; the prosumer system is created considering grid code specifications, power factor stability with two different approaches and it is aimed to be integrated as DG. Afterwards, in chapter four, it is presented the integration of the different management systems developed and proposed throughout this doctoral project into a test distribution network, by means of a multiphase continuous power flow software separately coded. Finally, conclusions and future work are placed in the fifth chapter.

1.10   References

[1]   Z. Chen, "Issues of Connecting Wind Farms into Power Systems," in *2005 IEEE/PES Transmission & amp; Distribution Conference & amp; Exposition: Asia and Pacific*, pp. 1–6.

[2]   P. P. Barker and R. W. De Mello, "Determining the impact of distributed generation on power systems. I. Radial distribution systems," in *2000 Power Engineering Society Summer Meeting (Cat. No.00CH37134)*, vol. 3, pp. 1645–1656.

[3]   Y. M. Atwa and E. F. El-Saadany, "Probabilistic approach for optimal allocation of wind-based distributed generation in distribution systems," *IET Renew. Power Gener.*, vol. 5, no. 1, p. 79, 2011.

[4]   G. Delille, B. Francois, and G. Malarange, "Dynamic Frequency Control Support by Energy Storage to Reduce the Impact of Wind and Solar Generation on Isolated Power System's Inertia," *IEEE Trans. Sustain. Energy*, vol. 3, no. 4, pp. 931–939, Oct. 2012.

[5]   N. D. Hatziargyriou and A. P. Sakis Meliopoulos, "Distributed energy sources: technical challenges," in *2002 IEEE Power Engineering Society Winter Meeting. Conference Proceedings (Cat. No.02CH37309)*, vol. 2, pp. 1017–1022.

[6]   J. W. Smith and D. L. Brooks, "Voltage impacts of distributed wind generation on rural distribution feeders," in *2001 IEEE/PES Transmission and Distribution Conference and Exposition. Developing New Perspectives (Cat. No.01CH37294)*, vol. 1, pp. 492–497.

[7]   J. A. P. Lopes, N. Hatziargyriou, J. Mutale, P. Djapic, and N. Jenkins, "Integrating distributed generation into electric power systems: A review of drivers, challenges and opportunities," *Electr. Power Syst. Res.*, vol. 77, no. 9, pp. 1189–1203, 2007.

[8]   M. Liserre, R. Teodorescu, and F. Blaabjerg, "Stability of photovoltaic and wind turbine grid-connected inverters for a large set of grid impedance values," *IEEE Trans. Power Electron.*, vol. 21, no. 1, pp. 263–272, Jan. 2006.

[9]   M. Bollen and F. Hassan, *Integration of distributed generation in the power system*. New Jersey: John Wiley & Sons, Inc., 2011.

[10]   J. B. Garrison and M. E. Webber, "An integrated energy storage scheme for a dispatchable solar and wind powered energy system," *J. Renew. Sustain. Energy*, vol. 3, no. 4, pp. 1–12, 2011.

[11]   R. Sioshansi and P. Denholm, "The Value of Concentrating Solar Power and Thermal Energy Storage," *IEEE Trans. Sustain. Energy*, vol. 1, no. 3, pp. 173–183, Oct. 2010.

[12]   A. Pina, C. Silva, and P. Ferrão, "The impact of demand-side management strategies in the penetration of renewable electricity," *Energy*, vol. 41, no. 1, pp. 128–137, May 2012.

[13]   B. K. Perera, P. Ciufo, and S. Perera, "Point of common coupling (PCC) voltage control of a grid-connected solar photovoltaic (PV) system," in *IECON 2013 - 39th Annual Conference of the IEEE Industrial Electronics Society*, 2013, pp. 7475–7480.

[14]   H. M. I. Pousinho, J. Contreras, P. Pinson, and V. M. F. Mendes, "Robust optimisation for self-scheduling and bidding strategies of hybrid CSP–fossil power plants," *Int. J. Electr. Power Energy Syst.*, vol. 67, pp. 639–650, 2015.

[15]   X. Wang, A. Palazoglu, and N. H. El-Farra, "Operational optimization and demand response of hybrid renewable energy systems," *Appl. Energy*, vol. 143, pp. 324–335, 2015.

[16]   F. Bouffard and F. D. Galiana, "Stochastic security for operations planning with significant wind power generation," 2008, pp. 1–11.

[17]   Y. Zhao, L. Ye, Z. Li, X. Song, Y. Lang, and J. Su, "A novel bidirectional mechanism based on time series model for wind power forecasting," *Appl. Energy*, vol. 177, pp. 793–803, Sep. 2016.

[18]   K. W. Wee, S. S. Choi, and D. M. Vilathgamuwa, "Design of a Least-Cost Battery-Supercapacitor Energy Storage System for Realizing Dispatchable Wind Power," *IEEE Trans. Sustain. Energy*, vol. 4, no. 3, pp. 786–796, Jul. 2013.

[19]   J. Wang *et al.*, "Wind power forecasting uncertainty and unit commitment," *Appl. Energy*, vol. 88, no. 11, pp. 4014–4023, Nov. 2011.

[20]   M. Lei, L. Shiyan, J. Chuanwen, L. Hongling, and Z. Yan, "A review on the forecasting of wind speed and generated power," *Renew. Sustain. Energy Rev.*, vol. 13, no. 4, pp. 915–920, 2009.

[21]   X. Wang, P. Guo, and X. Huang, "A Review of Wind Power Forecasting Models," *Energy Procedia*, vol. 12, pp. 770–778, 2011.

[22]   I. J. Ramirez-Rosado, L. A. Fernandez-Jimenez, C. Monteiro, J. Sousa, and R. Bessa, "Comparison of two new short-term wind-power forecasting systems," *Renew. Energy*, vol. 34, no. 7, pp. 1848–1854, 2009.

[23]   J. Alonso-Montesinos and F. J. Batlles, "Solar radiation forecasting in the short- and medium-term under all sky conditions," *Energy*, vol. 83, pp. 387–393, 2015.

[24]   J. Thorey, V. Mallet, C. Chaussin, L. Descamps, and P. Blanc, "Ensemble forecast of solar radiation using TIGGE weather forecasts and HelioClim database," *Sol. Energy*, vol. 120, pp. 232–243, 2015.

CHAPTER 2

STOCHASTIC MODEL OF WIND-FUEL CELL FOR A SEMI-DISPATCHABLE POWER GENERATION

Renewable energies are increasingly being used to generate electricity. Integration to the network, however, requires adjusting the new technologies in order to meet the established norms. Wind and photovoltaic renewable energy generation technologies are up to now the most developed, however in both, intermittence is the major issue to attend for grid connection.

The issue with intermittence in wind power supplied to the network can be smoothed when a forecast model is implemented. The approach suggested in this study uses an energy storage device (ESD) to stabilize the inherent variations and to balance the deviations of the actual wind power to better meet the planned network infeed. The purpose of the ESD is to reduce the intermittence with the implementation of a filter and be able to meet the short-term planned production of a hybrid system (HS) at the distribution level. To keep a stable frequency in the network, what matters for the operation of the transmission system is not so much the variation in production but the unpredictability of the production [1], which is study in this work.

This chapter, as shown in the following sections, presents the ability to change the output power of the HS from a non-dispatchable to a semi-dispatchable generation giving the capability to inform the system operator (SO) to program the power dispatch. The flexibility of power dispatch depends greatly on the short-term prediction and the storage characteristics to reduce the variations of the power generated by the wind turbine.

Unlike other studies, in here its proposed an advance energy management system (EMS) to overcome the effect on the frequency when the HS, relying solely on clean energy sources without depending on fossil power plants, is connected as distributed generation (DG).

2.1 Hybrid system setup

The proposed HS, according with the historic wind measurements from meteorological stations in Mexico City, is composed by a 5 kW Iskra small wind turbine [2], a 2.4 kW PEMFC [3], an electrolyzer from the brand Proton OnSite with a net production rate of 18.8 standard liter per minute [4], and a 16,500 liters hydrogen storage [5]; the devices modeling is subsequently illustrated. In order to achieve the desired output power from the HS, it is proposed the use of a forecasting method as explained in this section.

The control is recreated in a computational form, in which the HS output is reflected in the activation, the power regulation and the interaction between the HS elements as seen in Fig. 2.1, where the continuous, dashed and pointed arrows represent the electric, control data, and hydrogen flow respectively. The HS is supposed to connect to the distribution network, taking into account the power level used by normal households in Mexico City at different times of the year

[6]. The HS can be adjusted to work as a constant power generator or to meet a signal reference output power, based on the daily historic load of the household(s). This can make the user change the consumption habits in order to have a better response to the system and to decrease the total cost of their electric consumption [7], [8].
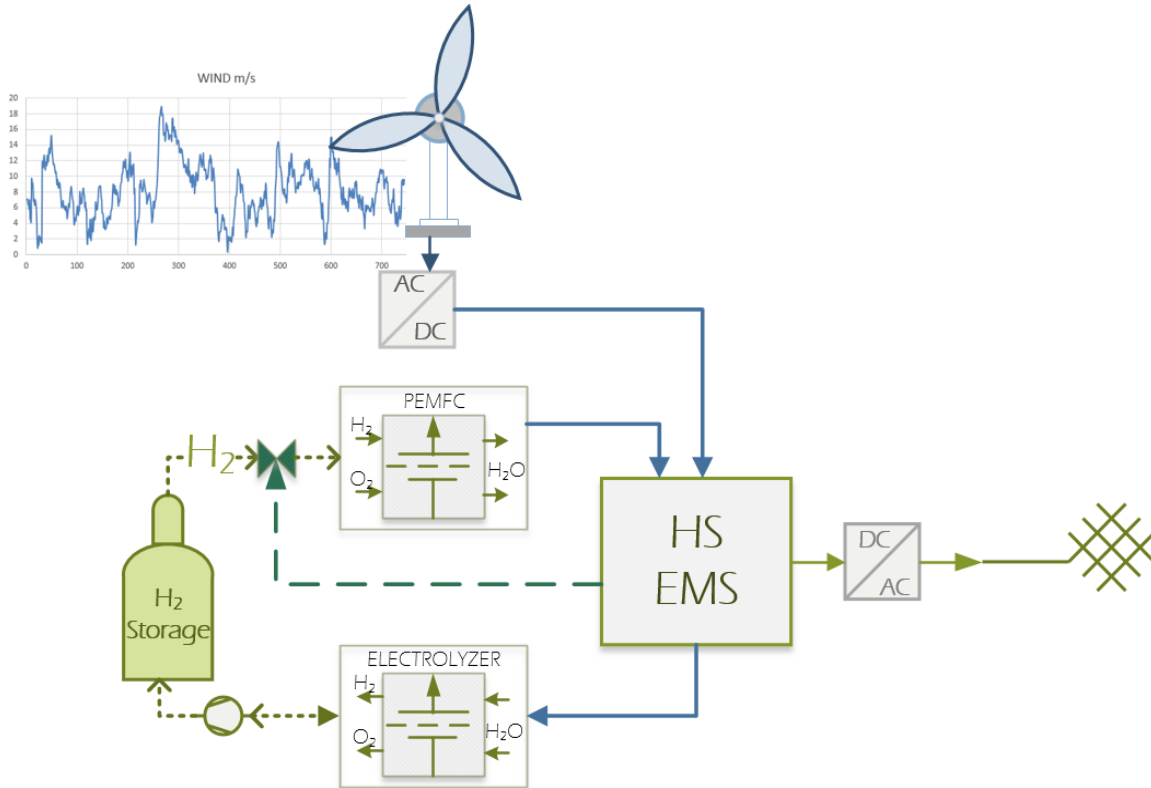
Fig. 2.1. Wind-FC hybrid system.

Fig. 2.1 shows the flow of the main energies that sustain the HS where the left side is the hydrogen flow and the right side is the electric power flow with the input and outputs of the systems. This figure also shows the electric conversion AC/DC and DC/AC taking into account that the FC has a DC output. The power will be controlled, regulated and distributed to the network and electrolyzer with the purpose of storing energy in the form of hydrogen.

In order to implement a controller one must understand and describe the models used in the system. Therefore, in the following section the basic operation of the HS components will be introduced.

2.2   Implemented models philosophy

The interaction between the HS elements described in Section 2.1 is done through a developed MPC algorithm. In consequence, the development of a wind and radiation forecast algorithm, alongside the modeling of the different implemented generation devices is presented.

2.2.1 Forecast model

Energy forecasting is particularly meaningful when considering wind power because of dispatch planning and market operations [9], the focus in this thesis is dispatch planning.

There are two approaches for wind speed forecasting, namely weather based and time series based. While the former uses hydrodynamic atmospheric models which incorporate physical phenomena such as frictional, thermal and convective effects, the latter uses only historical wind speed data recorded at the site to build statistical models from which forecasts are derived [10].

The sample data used for the forecast, was a three months data with a 10 min resolution (12,960 measurements) from a one year data recollected from Mexico City; the complete study was made for a whole year. Even though the collected measurements data covers a year, in this study only the first week of results was shown so the reader can truthfully see the behavior of the hybrid system and the output power in a clear way.

Timescales

One of the largest challenges of wind power, as compared to conventionally generated electricity, is its dependence on the volatility of the wind. This behavior happens on all time scales, but two of them are most relevant: One is for the turbine control itself (from milliseconds to seconds), and the other one is important for the integration of wind power in the electrical grid, and therefore determined by the time constants in the grid (from minutes to weeks) [11]. One can distinguish the following types of forecast applications:

- Allocation of reserves based on the expected wind power feed.

- Optimization of the scheduling of conventional power plants by functions such as economic dispatch etc. The prediction horizons can vary between 3-10 hours depending on the size of the system and the type of conventional units included (i.e. for systems including only fast conventional units, such as diesel gensets or gas turbines, the horizon can be below 3 hours).

- Even longer time scales would be interesting for the planning of large power plant components, wind turbines or transmission lines. However, the accuracy of weather predictions decreases strongly looking at 5-7 days in advance.

Wind speed variations in each of the time scales have implications on the operation of the utility system as indicated in Table 2.1 [10].

Table 2.1. Forecast timescale and implication

Time scale	Implication
Minutes/hours	Regulation/load-following
Day(s)	Day-ahead scheduling/unit commitment
Months	Resource allocation
Year(s)	Economic viability

Regressive methods

Regression has two meanings: one arises from the joint probability distribution of two random variables; the other is born of the need to adjust some function to a set of data. The classical regression model is used to describe a static relation between a dependent variable Y_t and p independent variables $X_{1t}, \ldots, X_{pt}$. In time series analysis, the observations occur successively in time and most frequently with an equidistant time distance [12].

In general form the regression model is written as

$$Y_t = f(X_t, t; \theta) + \varepsilon_t \tag{2.1}$$

where the function has $p + 1$ independent variables $X_t = \left(X_{1t}, \ldots, X_{pt}\right)^T$ plus t, but with unknown parameters $\theta = (\theta_1, \ldots, \theta_m)^T$. The independent variable t is introduced to indicate that the model class described by (2.1) contains models where f is a function of t.

A general linear model is a particular case of the regression model (2.1) where the function f is linear in the parameters θ. Some examples of general linear model are shown in Table 2.2 [12].

Table 2.2. General linear models

Model	Mathematical model
Constant mean	$Y_t = \theta_0 + \varepsilon_t$ $x_t = 1, \theta = \theta_0$
Simpler linear regression	$Y_t = \theta_0 + \theta_1 z_t + \varepsilon_t$ $x_t = (1, z_t)^T, \theta = (\theta_0, \theta_1)^T$
Quadratic	$Y_t = \theta_0 + \theta_1 z_t + \theta_2 z_t^2 + \varepsilon_t$ $x_t = (1, z_t, z_t^2)^T, \theta = (\theta_0, \theta_1, \theta_2)^T$
With two independent variables	$Y_t = \theta_0 + \theta_1 z_{1t} + \theta_2 z_{2t} + \varepsilon_t$ $x_t = (1, z_{1t}, z_{2t})^T, \theta = (\theta_0, \theta_1, \theta_2)^T$
Mixed	$Y_t = \theta_0 + \theta_1 \sin(wt) + \theta_2 \xi_t + \theta_3 z_{1t} + \theta_4 z_{2t} + \theta_5 z_{1t} z_{2t} + \varepsilon_t$ $\xi_t = \begin{cases} 0 & t \leq 200 \\ 1 & t \geq 200 \end{cases}$ (step variable) $x_t = (1, \sin(wt), \xi_t, z_{1t}, z_{2t}, z_{1t} z_{2t})$ $\theta = (\theta_0, \theta_1, \theta_2, \theta_3, \theta_4, \theta_5)$

A useful procedure for the selection of a model, when having only one prediction variable, is to plot the response variable against the prediction variable. If the graph reveals a linear trend, then a linear regression model must be assumed. If any curvature is evident, a quadratic or higher-order model must be assumed to fit the data.

After the model selection, the estimation of parameters is obtained. The process of estimation is concerned with the design of a rule or algorithm, the estimator, to extract useful signal information from random data. The method of least squares is about estimating parameters by minimizing the squared discrepancies between observed data, on the one hand, and their expected values on the other. Fig. 2.2 shows a formal description of the estimation problem [13].
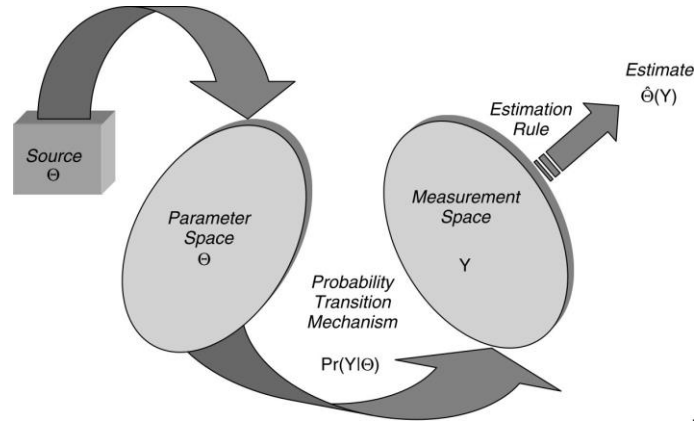
Fig. 2.2. Estimation problem.

In least square estimates, let us assume that the parameters in the regression model (2.1) are unknown. Then they may be estimated from the following N observations of the dependent and independent variables

$$(y_1, x_1), (y_2, x_2), \ldots, (y_N, x_N) \tag{2.2}$$

based on these observations it is wanted an estimate $\hat{\theta}$ of θ such that $f(x_t; \hat{\theta})$ describes the observations as well as possible [12].

The least squares estimates are found from

$$\hat{\theta} = \arg\min_{\theta} S(\theta) \tag{2.3}$$

where

$$S(\theta) = \sum_{t=1}^{N} [y_t - f(x_t; \theta)]^2 = \sum_{t=1}^{N} \varepsilon_t^2(\theta). \tag{2.4}$$

Stochastic process

A statistical phenomenon that evolves in time according to probabilistic laws is called a stochastic process. We will often refer to it simply as a process, omitting the word "stochastic". The time series to be analyzed may then be thought of as a particular realization, produced by the underlying probability mechanism, of the system under study. In other words, in analyzing a time series we regard it as a realization of a stochastic process [14].

A stochastic process is a function having two arguments, $\{X(t, \omega), \omega \epsilon \Omega\}$, where Ω is the sample space, or the ensemble, of the process. This implies that Ω is the set of all the possible time series that can be generated by the process. For a fixed t we say that $X(t, \cdot)$ is a random variable, and for fixed $\omega \epsilon \Omega$ its called a realization of the process [12].

For example, taking a set of observations (other realizations of the underlying stochastic process), which might have been generated by the same system, in the same $N = 70$ batches as the batch data in Fig. 2.3. Thus, Fig. 2.4 shows the yields from batches $t = 21$ to $t = 30$ (thick line), together with other time series that might have been obtained from the population of time series defined by the underlying stochastic process. It follows that we can regard the observation z_t at a given time t, say $t = 25$, as a realization of a random variable z_t with probability density function $p(z_t)$. Similarly, the observations at any two times, say $t_1 = 25$ and $t_2 = 27$, may be regarded as realization of two random variable z_{t1} and z_{t2} with joint probability density function $p(z_{t1}, z_{t2})$. In general, the observations making up an equispaced time series can be described by an N-dimensional random variable $(z_1, z_2, \ldots, z_N)$ with probability distribution $p(z_1, z_2, \ldots, z_N)$ [14].
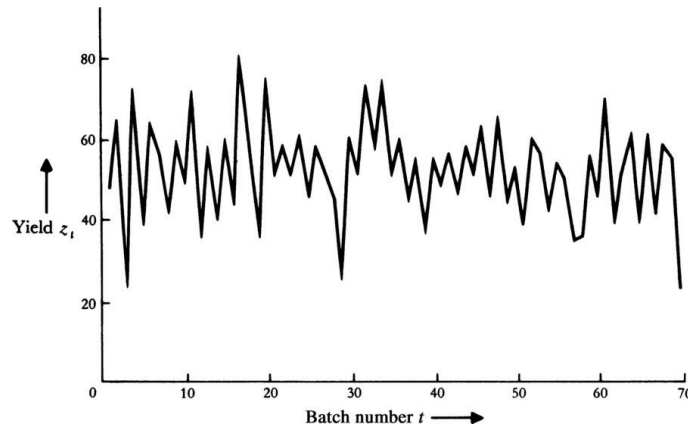
Fig. 2.3. Yields of 70 consecutives batches from a chemical process[14].
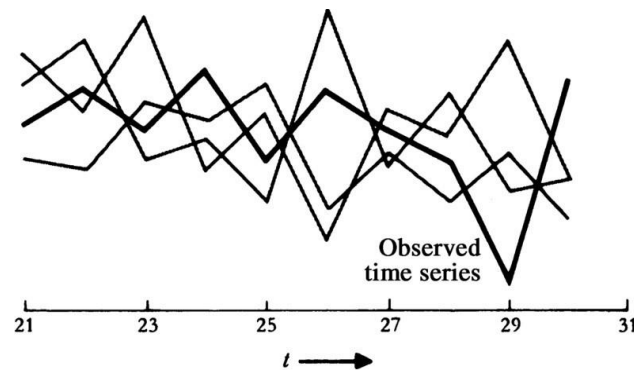
Fig. 2.4. Observed time series (thick line), with other time series representing realizations of the same stochastic process [14].

Autoregressive (AR) model

A stochastic model that can be extremely useful in the representation of certain practically occurring series is the autoregressive model. In this model, the current value of the process is expressed as a finite, linear aggregate of previous values of the process and a random shock a_t [14].

In this model, the current value of the process was expressed as a finite, linear aggregate of previous values of the process. The AR model is a classic forecast model implemented in time series analysis. An AR(ρ) model relates ρ historic observations to the value Y_{t+1}

$$Y_{t+1} = \mu + \sum_{i=0}^{\rho-1} \Theta_i Y_{t-i} + \varepsilon_{t+1} \qquad (2.5)$$

$$Y_{t+1} = \hat{Y}_{(t+1|t)} + \varepsilon_{t+1} \qquad (2.6)$$

from (2.5), μ is a term correcting the mean value, Θ_i is the coefficient of each past observation Y_{t-i} describing its influence on the next value Y_{t+1}, and finally ε_t is assumed to be white noise [14], [15]. This is an iterative process, meaning that a six-steps-ahead forecast is required to calculate (2.6), to upgrade Y_t plugging in the last forecast value generated, and to repeat the process:

$$\hat{Y}_{t+k|t} = \mu + \sum_{i=0}^{\rho-1} \hat{\theta}_i \hat{Y}_{t+k-(i+1)|t} \qquad (2.7)$$

$\hat{Y}_{t+k-(i+1)|t}$ is equal to the observation if the observation exists; otherwise, it is equal to the prediction. An AR process is a linear process characterized by a finite number of terms.

Recursive least square with forgetting factor [12]

Notice that the k-step AR(ρ) model can be written as

$$Y_{t+k} = (Y_t, Y_{t-1}, \dots, Y_{t-\rho+1}) \begin{pmatrix} \Theta_0 \\ \vdots \\ \Theta_{\rho-1} \end{pmatrix} + \varepsilon_{t+k} \qquad (2.8)$$

which, by introducing the standard notation using X as the regressor vector, becomes

$$Y_{t+k} = X_t^T \hat{\theta}_t + \varepsilon_{t+k} \qquad (2.9)$$

Recursive least square (RLS) with forgetting factor is based on the AR process and allows the parameter vector θ to change over time. For the weighted least squares estimator, the weighted estimation is calculated as

$$\hat{\theta}_t = \hat{\theta}_{t-1} + R_t^{-1} X_{t-k} [Y_t - X_{t-k}^T \hat{\theta}_{t-1}] \qquad (2.10)$$

where

$$R_t = \lambda R_{t-1} + X_{t-k} X_{t-k}^T \qquad (2.11)$$

this is a recursive implementation of a weighted least squares estimation, where the weights are exponentially decaying over time. With X_t as the regressor vector, θ_t as the coefficient vector and Y_t as the dependent variable (observation at time t), the k-step prediction at t is

$$\hat{Y}_{t+k|t} = X_t^T \hat{\theta}_t \tag{2.12}$$

the parameter λ is the forgetting factor, describing how fast historical data are down-weighted. The weights are equal to

$$\omega(\Delta t) = \lambda^{\Delta t} \tag{2.13}$$

Δt is the age of the data [16]. If $\lambda(t)$ is constant $\lambda(t) = \lambda$, then the memory is of the form

$$T_0 = \frac{1}{1-\lambda}. \tag{2.14}$$

Typical values for λ are in the range from 0.90 to 0.995. The forgetting factor can be chosen based on assumptions of the dynamics, or it can be a part of the global optimization [12].

2.2.2 Wind turbine model

In a typical domestic system the wind turbine is coupled directly to a three-phase synchronous permanent magnet AC generator mounted on the same shaft. To save capital costs, domestic installations do not have variable pitch rotor blades so the rotor speed varies with the wind speed. The generator output voltage and frequency are proportional to the rotor speed and the current is proportional to the torque on the shaft. The output is rectified and fed through a buck-boost regulator to an inverter which generates the required fixed amplitude and frequency AC voltage as shown in Fig. 2.5.
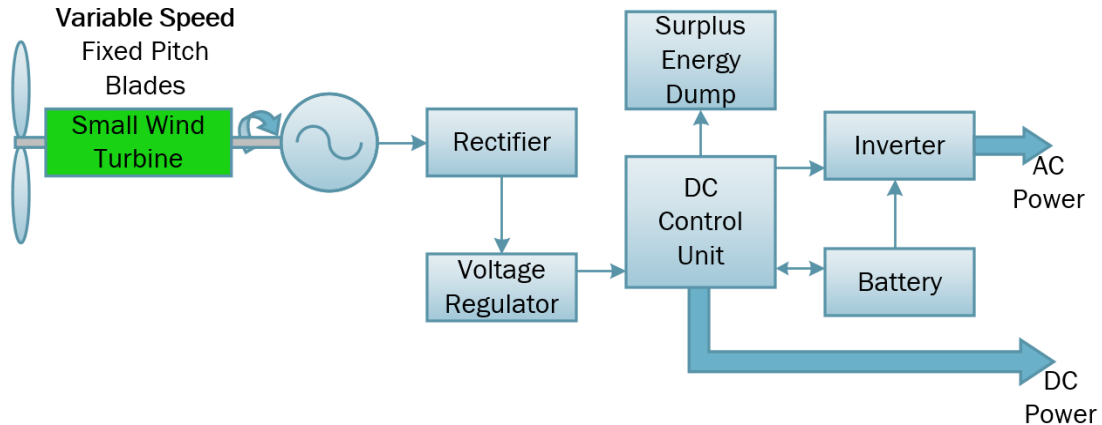
Fig. 2.5. Domestic system of small scale wind power.

Permanent magnet excitation is generally used in newer smaller scale turbine types, since it enables higher efficiency in addition to smaller wind generator blade diameter. Though recent research has considered larger scale patterns, the economics of huge volumes of large volume material has constrained their practical use. The primary benefit from permanent magnet synchronal generators (PMSG) is that they do not require any external excitement current. A major cost benefit in using the PMSG is a diode bridge rectifier that may be used at the generator devices since no external excitation current should be used. A variety of research has been performed using a diode rectifier [17].

The wind turbine captures the wind's kinetic energy in a rotor consisting of two or more blades mechanically coupled to an electrical generator. Aerodynamic power available in the wind can be calculated as (2.15) [18], [19], [20]. The wind power is the flow speed of the kinetic energy by second and varies as the cube of the wind speed. The model of low power wind turbine distribution needs the following characteristics: wind speed, direction, air density, hub height, swept area, rated power, boot speed and cutting speed, magnetizing reactance, resistances of the turbine, and curve point values of speed versus output power. The aforementioned data are required in order to calculate the speed wind correction depending on the height of the installation, the coefficient power curve, and finally the active power generated. In addition, the calculation involves the reactive power required, taking into account that a wind machine type 1 or 2, is implemented; these machines do not have compensation and are used in low tension [21]–[25].

$$P_w = 0.5 C_p \rho A V_w^3 \tag{2.15}$$

P_w is the extracted power from the small wind turbine (SWT) in [W], ρ is the air density [1.225 kg/m³ at sea level], A is the wind turbine swept area [m²], V_w is the wind speed [m/s], and C_p is the power coefficient representing the wind turbine efficiency.

Wind speed measurements are made at the height of the anemometer which is different to the actual wind turbine height. To compute V_w the wind shear has to be considered; which is, a difference in wind speed and/or direction over a relatively short distance in the atmosphere. Atmospheric wind shear is normally described as either vertical or horizontal wind shear. Vertical wind shear is a change in wind speed or direction with change in altitude. Horizontal wind shear is a change in wind speed with change in lateral position for a given altitude

All wind speed data is calculated from those which will be directly experienced by the wind turbines. Wind speeds are therefore related directly to those at hub height and calculated to be at height assuming reference conditions. Reference conditions are those used when reporting the measured and/or warranted sound power levels of the wind turbines and assume a ground roughness length [24]. If the wind speed measurements were made at a height above ground level different to the installation, a correction algorithm must be implemented to compute the V_w at the proposed turbine height as follows.

$$V_{cor} = V_w \cdot \frac{ln\left(\frac{H_1}{z}\right)}{ln\left(\frac{H_2}{z}\right)} \tag{2.16}$$

where V_{cor} is the wind speed to be calculated, V_w represents the measured wind speed, z the roughness length, H_1 is the height of the wind speed to be calculated, and H_2 denotes the height of the measured wind.

The roughness length z, indicates the factor of change of the surface. A change from a smooth to a rough site will increase the surface frictional stress and consequently lead to the wind at the surface slowing down. This increased shear will thus lead to the effect being slowly passed upwards through the surface boundary layer until the wind throughout the layer is slowed down. The boundary layer gets back into equilibrium with the surface. A rough to a smooth surface change will lead to a speeding up of the wind throughout the profile. To reach equilibrium there

must be a sufficiently long stretch of ground [26]. The roughness class can be taken from Appendix A.

The air density (ρ) is derived from the measurement of air temperature and air pressure using (2.17). At high temperatures it is recommended also to measure relative humidity and to correct for it. The air temperature sensor shall be mounted at least 10 m above ground level. It should be mounted on the meteorological mast close to hub height to give a good representation of the air temperature at the SWT rotor center [27].

$$\rho = \rho_{ref} \cdot e^{\left[\left(-\frac{h}{8435}\right)-\left(\frac{T-15}{288}\right)\right]}$$
(2.17)

ρ_{ref} is the reference air density (normally 1.225 kg/m^3), h is the height above sea level, and T denotes the air temperature averaged in °C.

The power coefficient (C_p) tells you how efficiently a turbine converts the energy in the wind to electricity by dividing the electrical power output with the wind energy input to measure how technically efficient a wind turbine is. In other words, we take the power curve, and divide it by the area of the rotor to get the power output per square meter of rotor area. For each wind speed, we then divide the result by the amount of power in the wind per square meter.

C_p is the fraction of the upstream wind power, which is captured by the rotor blades. The remaining power is discharged or wasted in the downstream wind, theoretically maximum value of C_p is 0.59. To compute C_p the SWT power curve is required, found in the SWT datasheet as the one in Fig. 2.6, and the swept area is calculated by (2.18).
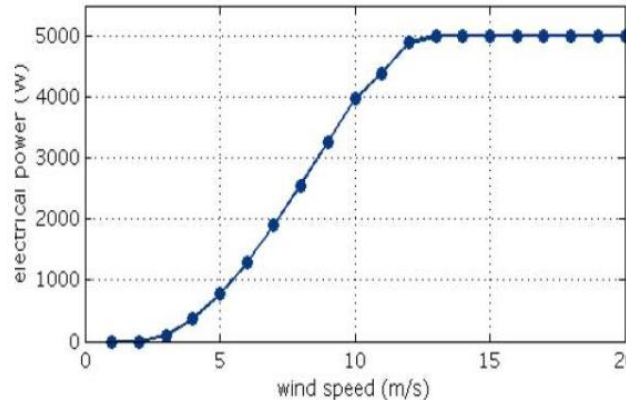
Fig. 2.6. Power curve and energy yield for a 5 kW Iskra wind turbine.

$$P_{dis} = \frac{P_{VelTurb}}{A}$$
(2.18)

P_{dis} is the available power by square meter, $P_{VelTurb}$ denotes the power according to the wind speed, and A is the swept area of the SWT. Subsequently, $P_{VelTurb}$ is divided by the nominal wind power (P_{nom}) to determine the power coefficient curve in respect to the peripheral speed (λ_{curve}) expressed as follows [28]

$$C_p/\lambda_{curve} = \frac{P_{dis}}{P_{nom}}. \tag{2.19}$$

To calculate P_{nom} is considered (2.15) with nominal values as $C_p = 1$, $\rho = 1.225 \text{ kg/m}^3$ and $A = 1 \text{ m}^2$ for the different speed values.

The turbine reactive power is calculated, to be considered in the power flow analysis when the HS is connected to the grid. Most available SWT have permanent magnet generator, thus, the system does not consume reactive power from the grid; instead, wind turbine generation can be used to supply local reactive power consumption [29], [30]. Reactive power of wind turbine generation depends on the inverter configuration, in which there are extensive researches concerning the reactive power control at the inverter as in [31]–[33]; been out of this research scope. To include the reactive power of the turbine in the model, given the existence of a steady-state model of an induction machine and the application of Boucherot's theorem [25], the expression for the reactive power by the wind turbine is

$$Q_w = \frac{V^2(X_c - X_m)}{X_c X_m} + \frac{X(V^2 - 2RP_w)}{2(R^2 + X^2)} + \frac{X^2\sqrt{(V^2 - 2RP_w)^2 - 4P^2(R^2 + X^2)}}{2(R^2 + X^2)} \tag{2.20}$$

where V is the voltage, X_c is the capacitor bank reactance, X_m represents the magnetizing reactance, X is the sum of the stator and rotor reactances, R is the sum of the resistances of the stator and rotor, and P_w is the wind active power.

2.2.3 Electrolyzer model

Hydrogen production through water electrolysis is a method of storing wind energy, and it is of great importance to understand that the hydrogen is fundamental to the implementation of this hybrid system, since it is the energy carrier that allows the hybrid system to work autonomously for long periods of time. The hydrogen can be stored and distributed to be used a posteriori to generate electricity via the FC; the only by-product of this combustion is water, so no additional pollution is generated [34].

The hydrogen production by electrolysis of water is reached by the decomposition of water into oxygen and hydrogen gas, thanks to an electric current passed through the water. The reaction has a standard potential of 1.23 V, meaning it ideally requires a potential difference of 1.23 volts to split water. The chemical representation is given by

$$2H_2O \rightarrow 2H_2 + O_2 \ . \tag{2.21}$$

The basic operation of the electrolyzer can be demonstrated by a small experiment, which is shown in Fig. 2.7 [35]. The water is electrolyzed into hydrogen and oxygen by passing an electric current through it.
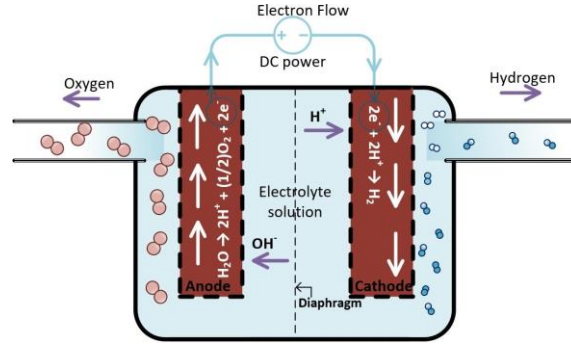
Fig. 2.7. Water electrolysis experiment.

The electrolysis is fundamental for the production of pure hydrogen, and this must be taken into account in the hybrid system model, by implementing the laws of Faraday electrolysis.

Faraday's first law of electrolysis. The mass of the substance altered at the electrode during the electrolysis is directly proportional to the amount of electricity transferred to that electrode. The quantity of electricity indicates the amount of electrical charge, typically measured in coulombs [36].

Faraday's second law of electrolysis. When the same quantity of electricity is passed through several electrolytes, the mass of the substances deposited are proportional to their respective chemical equivalent or equivalent weight [36].

The first law can be used to obtain the amount of hydrogen generated according to a DC current in a certain amount of time, being relevant to the operation of the fuel cell. It can be expressed in mathematical form as follows

$$V_g = \frac{R_g \cdot I \cdot T \cdot t}{F \cdot p \cdot z}$$ (2.22)

the gas volume in liters is represented by V_g, R_g is the ideal gas constant equal to 0.0820577 (L·atm/mol·K), I means the current in amperes, T is the temperature in °K, t is the time in seconds, z is the number of excess electrons and takes the value of 2 for H_2 and 4 for O_2, p represents the ambient pressure in atmospheres and F represents the Faraday constant equal to 96485.33 in C/mol.

Electrolysis has the advantages of being static, simple and able to operate for long periods without attention, while generating hydrogen to be used in a fuel cell.

Considering Faraday's law of electrolysis (2.22) and the fact that the power required by the electrolyzer can be computed by means of the power equation $P_{el} = V_c \cdot I$, where I is the current, V_c represents the cell voltage and P_{el} is the power required for the electrolyzer, the volume of hydrogen generated from a certain amount of power can be expressed as

$$V_{H_2} = \frac{P_{el} \cdot R \cdot T \cdot t}{2 \cdot F \cdot p \cdot V_c}$$ (2.23)

V_{H2} is the volume of hydrogen produced by the cell. Implementing (2.23) the volume of hydrogen produced by the electrolyzer with P_{el} input power is deduced. Considering that the model applied to the HS will calculate the power required for the electrolyzer in the function of the wind power forecast, (2.23) is reorganized as

$$V_{H_2} = P_{el} \cdot l_{el} \tag{2.24}$$

where $l_{el} = \frac{R \cdot T \cdot t}{2 \cdot F \cdot p \cdot V_c}$.

2.2.4 Fuel cell model

The PEMFC is the type of cell that was used to develop the model, and is characterized by an efficient production of energy with high power density represented in Fig. 2.8. Since the cell separator is a polymer tape the cell operates at a relatively low temperature, which potentially allows quick start-up and issues such as sealing, assembly and operation are less complex than in other cell types. The need for handling corrosive acids or bases in this system is removed [37].
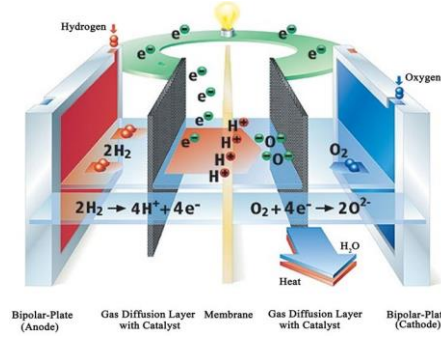
Fig. 2.8. Schematic of representative PEMFC.

The cell has internal electrical losses such as ohmic, activation and mass transport [37],[38].

The ohmic losses are caused by ionic resistance in the electrolyte and electrodes, electronic resistance in the electrodes, current collectors and interconnects, and contact resistances. Ohmic losses are proportional to the current density, depend on materials selection and stack geometry, and on temperature.

The activation-related losses stems from the activation energy of the electrochemical reactions at the electrodes. These losses depend on the reactions at hand, the electro-catalyst material and microstructure, reactant activities (and hence utilization), and weakly on current density.

Mass-transport-related losses are a result of finite mass transport limitations rates of the reactants and depend strongly on the current density, reactant activity, and electrode structure.

The cell voltage, is calculated based on the reversible open circuit voltage E and the voltage losses, as follows

$$V_c = E - \Delta V_{ohm} - \Delta V_{act} - \Delta V_{trans} \tag{2.25}$$

the internal losses in the fuel cell are neglected in this model, because their values tends to be very small and therefore do not significantly alter the result, as demonstrated in [39]. For the cell voltage, a value between 0.6V - 0.7V can be assumed [40]. In this research, a value of 0.68 is assumed in accordance with the efficiency of the FC.

The operation of the fuel cell can be understood to be essentially the reverse process of electrolysis of water, as this technology recombines the hydrogen with oxygen to generate electrical power and water.

Individual fuel cell units are combined as modules in series or parallel configurations to provide desired voltage and output power. The mechanical arrangement must ensure not only electrical contact among units, but also adequate circulation of gases, allowing catalyst reactions to take place at the correct temperatures and humidity levels [38]. The electric power generated by a FC is defined as

$$P_e = V_c \cdot I \cdot n \tag{2.26}$$

in which V_c is the voltage cell, I represents the current cell, and n is the number of fuel cells integrating the stack.

To know the amount of hydrogen needed by the fuel cell, one must know the number of fuel cells that make up the stack of the final FC array. By means of (2.22) and (2.26), the hydrogen used by the stack, in mol/s [38], [41], is deduced as

$$H_{2used} = \frac{P_{fc} \cdot n}{2 \cdot V_c \cdot F} \tag{2.27}$$

another way to calculate the hydrogen used is in kg/s, while considering the molar mass of the hydrogen and the Faraday constant (F), deduced as

$$H_{2used} = l_{fc} \cdot P_{fc} \tag{2.28}$$

l_{fc} is determined by $1.05 \times 10^{-8} \frac{n}{V_c}$.

In order to design the MPC, the impulse response function for the fuel cell is needed. Taking into account that the FC is an electrochemistry element, its dynamic is very fast as demonstrated in [42], [43]. To compute the impulse response of the FC the function in Fig. 2.9 is implemented to obtain $l_{fc,k}$ for future used in the MPC. The same function is required to obtain the impulse response for the electrolyzer and storage, $l_{el,k}$, and $l_{st,k}$ respectively.
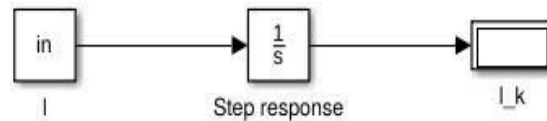
Fig. 2.9. Step response function.

2.3 Hybrid system EMS strategy

Depending on the objective function, various MPC strategies can be implemented. Model predictive control has the inherent advantages like the use for controlling a great variety of processes, including systems with long delay times or of non-minimum phases or unstable ones [44], [45]. In addition, the MPC introduces feedforward control to compensate measurable disturbances, allowing its application to this work to be more satisfactory [46].

Fig. 2.10 shows the basic MPC structure, been the HS EMS; the future outputs for a horizon N are predicted at each instant t. The predicted outputs for $k = 1,\ldots,N$ depend on the known values up to instant t and on the future control signals, $k = 0,\ldots,N-1$, which are to be sent to the system. The future control signals are calculated by optimizing a criterion in order to keep the process close to the reference trajectory $P_{t+k|t}^{ref}$, which is computed as the result of

$$P_{t+k|t} = \hat{P}_{t+k|t}^{w} + P_{fcmax,k} - P_{elmax,k} \tag{2.29}$$
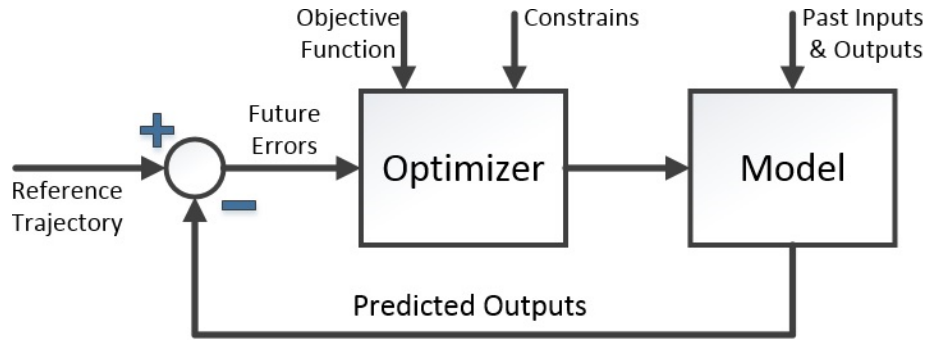
Fig. 2.10. MPC structure.

$\hat{P}_{t+k|t}^{w}$ represents the forecasted wind power, P_{fcmax} is the activation vector of the FC and P_{elmax} is the activation vector of the electrolyzer, where the last two are computed according to the priority given in the different scenarios. Equation (2.29) is then filtered through a moving average filter, which operates by averaging a number of points from the input signal to produce each point in the output signal [47]. In equation form it is written as

$$P_{t+k|t}^{ref}[k] = \frac{1}{M} \sum_{j=0}^{M-1} P_{t+k|t}[k+j] \tag{2.30}$$

where M is the number of points in the average. Afterwards, $P_{t+6|t}^{ref}$ is reported, and $P_{t+k|t}^{ref}$ for $k = 1,\ldots,N$ is used in the MPC.

$P_{t+k|t}$ is computed considering that the activation vector of the FC and electrolyzer depend on the priority given by the behavior of the HS. Afterwards, the forecast signal is filtered as to remove the high frequency changes and leave a smooth signal to be used as the reference trajectory.

The MPC manages the electric power of the HS and takes into account the output power, the filtered forecast and the actual wind power, so that the control decides how much power the FC is going to produce and how much power will be directed to the electrolyzer for saving energy for future fluctuations, thus, the output power will be almost without frequency changes and minimizing in a great extent the intermittence and variability of the wind power.

2.4 Forecast and MPC implementation in the hybrid system management

The purpose is to report to the SO how much power will be delivered to the grid one hour-ahead. Along the scenarios a priority is given and a constraint or condition will be added to compute $P_{t+k|t}$, changing the characteristics from (2.29) and recreating $P_{t+k|t}^{ref}$.

The reported data will be the trajectory followed by the HS by means of the MPC and will have the principal characteristic of being smooth in time as to avoid any operational instability like voltage or frequency in the grid because of the influence of the wind power. Furthermore, when a trajectory is applied to the control of the HS and successfully reached, it can be demonstrated that wind power as non-dispatchable energy, when implemented in a HS, can be converted to a semi-dispatchable electric source, making the management and distribution of energy more flexible.

Initially an algorithm to find the optimal forgetting factor (λ), by simply fitting a sequence of λ values from 0.96 to 1 was implemented, and the λ value which minimized the root mean square error (RMSE) was found for each horizon and forecast, as seen in Fig. 2.11.
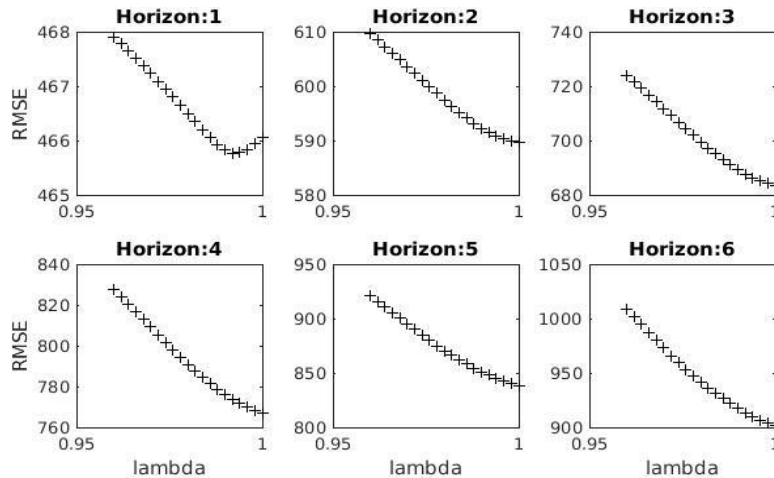
Fig. 2.11. Optimal forgetting factor.

The aforementioned optimal λ is implemented to compute the forecast for the different horizons applying RLS with the forgetting factor as explained in Section 2.2.1, which results in the forecast

for the different horizons k as shown in Fig. 2.12. The algorithm implemented to forecast one hour-ahead, with a resolution of 10 minutes, is called a six-steps-ahead forecast.
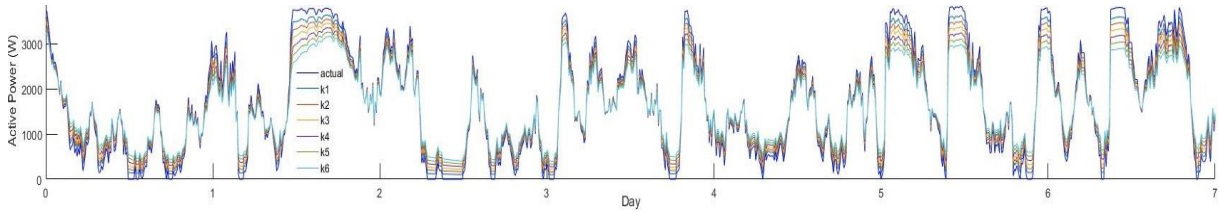
Fig. 2.12. Actual and k-step ahead forecast.

The time-series models are updated in each iteration of the process as described later in this section, taking into account the new data measured every 10 min. The expressions obtained for each horizon ($k = 1,\dots,6$) are

$$Y_t = 161.2 + 0.8324Y_{t-1} + 0.0461Y_{t-2} \tag{2.31}$$
$$Y_{t+1} = 248.3 + 0.8275Y_t - 0.00922Y_{t-1} \tag{2.32}$$
$$Y_{t+2} = 342.65 + 0.8228Y_{t+1} - 0.0698Y_t \tag{2.33}$$
$$Y_{t+3} = 439.93 + 0.7703Y_{t+2} - 0.0835Y_{t+1} \tag{2.34}$$
$$Y_{t+4} = 525.09 + 0.6905Y_{t+3} - 0.0641Y_{t+2} \tag{2.35}$$
$$Y_{t+5} = 634.7 + 0.7555Y_{t+4} - 0.1978Y_{t+3}. \tag{2.36}$$

The autocorrelation function (ACF) analysis result of the short term forecast is shown in Fig. 2.13, indicating that the used model is suitable for this study purpose.
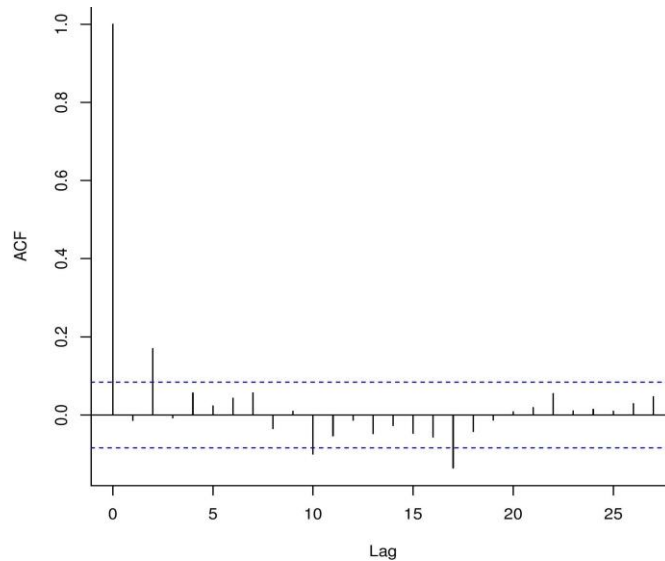
Fig. 2.13. ACF of the residuals.

Fig. 2.14 shows the RMSE as a function of the horizon k (10-min steps). The black curve is the RMSE for persistence and the red curve is for RLS. It is observed some improvement of the RLS over the persistence, but it is beyond the scope of the study to investigate the impact of using the forecasts compared to persistence.
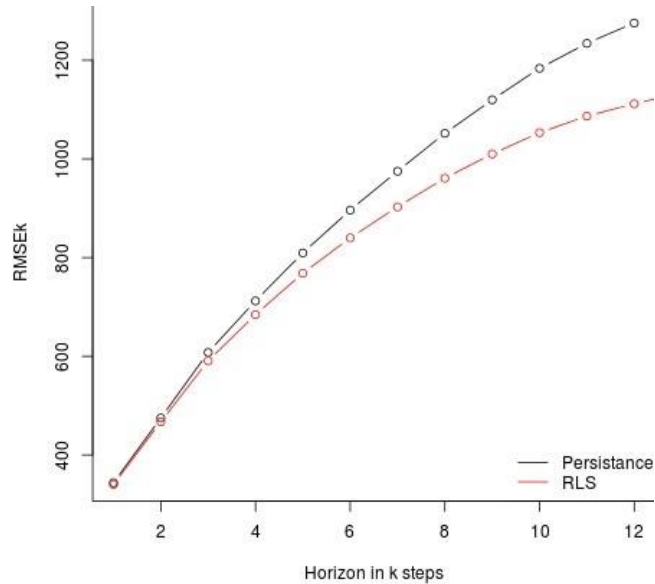
Fig. 2.14. RMSE as function of the horizon.

The forecast is done using the following steps which are repeated every 10 minutes

- Update historic data
- Run one-hour-ahead forecast
- Compute the 'new trajectory'
- Update the 'last trajectory', adding the last 10 minutes of the 'new trajectory' at the end of the last one, as to always have a one-hour-ahead forecast generation
- Report the new one hour-ahead updated trajectory to the system operator.

Different EMS scenarios were tested to be applied in the interaction of the inner elements of the hybrid system, with a variety of priorities for the output power; using the proposed developed MPC method.

This section presents and explains the different scenarios of control with the more significant outputs within the ones implemented, and based on these scenarios a decision about which one is more convenient to implement can be taken, depending on the purpose of the HS, the priorities and needed output power.

The computational process for all scenarios is shown in Fig. 2.15 in a generalized way, in which constraints change in their decision making depending on the priority for the HS of the case. The flowchart presents a never ending iterative process, updating the historical wind measurements and managing the HS energy round-the-clock.

With the computed forecast and the application of the models for the different elements that integrate the HS, the objective function can be deduced and implemented to be minimized in the MPC
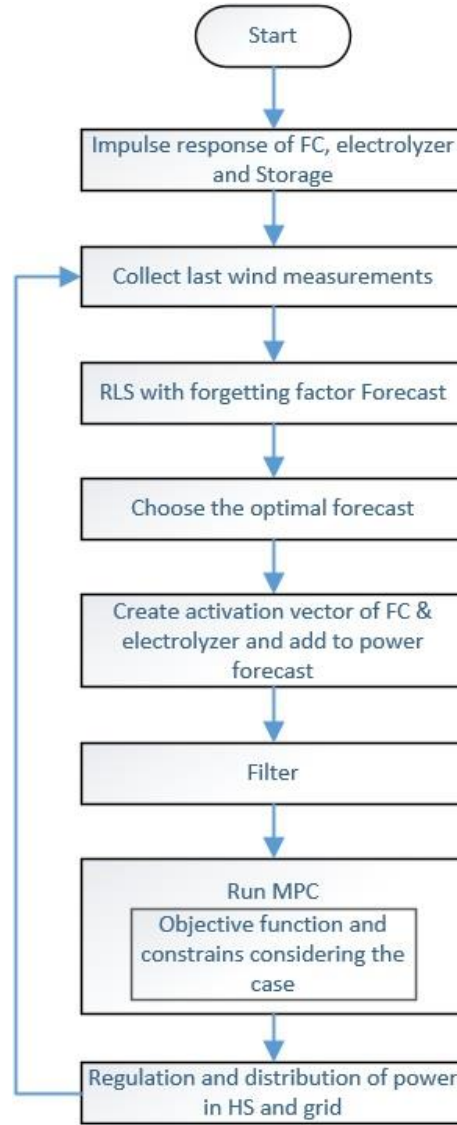
Fig. 2.15. HS operation flowchart.

$$\min_{P_{\theta,k}} \quad \left\| P_{w,k} - P_{t+k|t,k}^{ref} + P_{\phi,k} \right\|$$

$$subject\ to \quad \phi = \sum_{k=0}^{N} -l_{fc}P_{fc,k} + l_{el}P_{el,k} + l_{st,k}\phi_0$$

$$\phi_{min} \leq \phi \leq \phi_{max}$$
$$-P_{ele}^{nom} \leq P_{\phi,k} \leq P_{fc}^{nom}$$
$$P_{\phi,k} = P_{fc,k} - P_{el,k}$$
$$0 \leq P_{el,k}$$
$$0 \leq P_{fc,k}$$

(2.37)

the MPC minimizes an objective function subjected to constraints and manages the power flow of the HS, where $\| \quad \|$ is the vector norm or ℓ^2-norm, P_ϕ is the power flow to/from the elements connected to the storage calculated by the MPC, $P_{t+k|t}^{ref}$ is the reference trajectory based on the forecasted wind power computed with (2.30), P_{fc} is the power to be generated by the FC, P_{el} is the power destined to the electrolyzer, ϕ represents the level of storage and ϕ_0 represents the last measure of H_2 stored, ϕ_{max} and ϕ_{min} are the physical limits of the storage, l_{el}, l_{fc} and l_{st} represent the impulse response of the electrolyzer, FC and storage respectively based on the aforementioned models.

The constraints for the FC and electrolyzer are vectors with the physical nominal values of the elements represented by P_{fc}^{nom} and P_{ele}^{nom} respectively and implemented in the MPC. $P_{w,k}$ represents the vector with the actual power ($k = 0$) and forecasted wind power ($k = 1,\ldots,N$) meaning $P_w = \left[P_{k=0}^w, \hat{P}_{t+k|t}^w\right]$. Fig. 2.16 is explained for a better understanding of P_w, where $t = 27h30min$ represents the actual instant, been the $k = 0$ point. The continuous line before the actual point is the historic data incorporated in the time series analysis, and the dashed line after it, is the hour-ahead forecast representing the six steps-ahead, mentioned in Section 2.2.1 and Section 2.3.
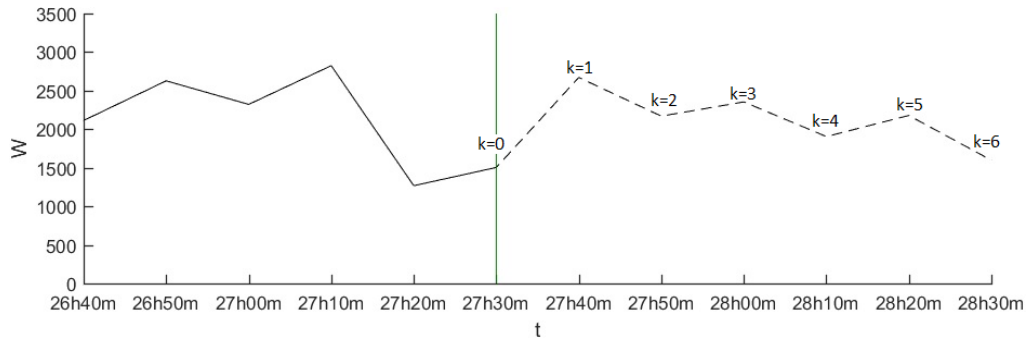
Fig. 2.16. P_w forecast at $t = 27h30min$.

2.5 Energy management system scenarios

Two scenarios are implemented to validate the algorithm proposed in this work. The scenarios establish priorities and have the main purpose of zero network frequency disturbance and as a second purpose, possession of a more stable and semi-dispatchable power generation.

  i)   The purpose of the first scenario MPC as an EMS, is smoothing the wind power, employing the power generated by the FC in a prioritized way as an electric generation source.
  ii) The second scenario focuses on having an as much as possible constant output power, from the HS and the probable "sacrifices" to accomplish it, regarding the wind power surplus.

Fig. 2.17 displays the actual active wind power available, in which it is noticeable the intermittence with abrupt ramps; i.e. sudden changes from 20 W to 3200 W.
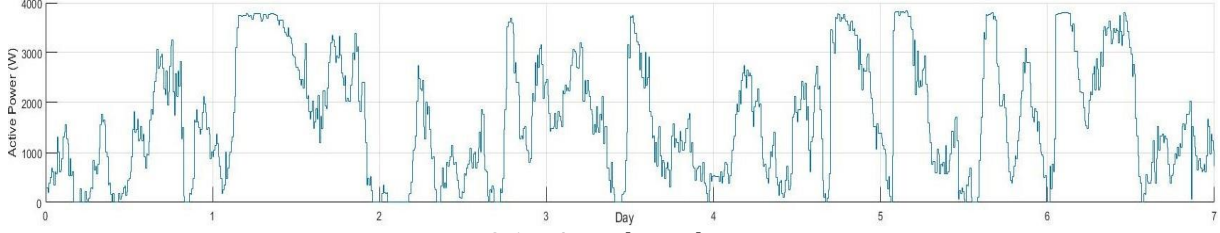
Fig. 2.17. Actual wind power.

2.5.1 Smoothing the wind power

In this scenario, the priority is to smooth the wind power generated by the turbine, managing the output power of the whole HS at every moment. To compute $P_{t+k|t}^{ref}$ from (2.29), first one must calculate P_{elmax} and P_{fcmax} considering the restrictions of the electrolyzer and the FC.

To calculate the vector P_{elmax}, both physical and characteristic constraints for the scenario are considered. In this scenario, the hydrogen level in the tank will be at least lower than an upper threshold level (Γ_{elup}) when charging or until the maximum of the tank is reached because of surplus of wind power, and above a lower threshold (Γ_{eldown}) of the tank, described mathematically as

$$P_{elmax} = \begin{cases} \hat{P}_{t+k|t}^w & \phi \leq \phi_{max}\Gamma_{elup} \\ 0 & \phi > \phi_{max}\Gamma_{elup} \end{cases} |\phi \leq \phi_{max}\Gamma_{eldown}. \tag{2.38}$$

The hydrogen storage will be charged when the tank presents a specified level of hydrogen, represented by the lower threshold (Γ_{eldown}), bearing in mind a base amount of hydrogen in case of contingency because of the uncertainty of the wind speed. The base amount will be assumed as the hydrogen required to generate maximum power from the FC in the next two hours, ensuring a smooth change in the output power without affecting the frequency of the network. In the charging period, the electrolyzer will use the wind power to produce hydrogen until the storage level reaches a specified upper threshold (Γ_{elup}) in which it stops charging. In this work, Γ_{elup} represents the hydrogen required for the FC to work eight hours ahead at maximum power.

Storage plays a great role when it comes to maintaining a stable output power of the HS for long periods of time. The activation and deactivation of the electrolyzer is the principal factor for maintaining a desired storage level. As seen in Fig. 2.18, a global flow chart explains how it was applied in the model, giving an idea of how it can be modified depending on the priority of the storage required from the HS.

To ensure constant smooth output power from the HS, constraints were applied on the activation of the FC. As a result the FC generates more frequently and compensates the variability in the wind power, according to the amount of hydrogen stored. When there is no wind, the output power is determined by the nominal FC value. Given the uncertainty in the wind speed this constraint was necessary to attain the designated power value without having to ask for backup from the grid. Therefore, the nominal value of the FC must be implemented in the MPC and in the activation of the FC. To compute $P_{t+k|t}^{ref}$ from (2.30), the activation vector of the FC is then calculated by

31
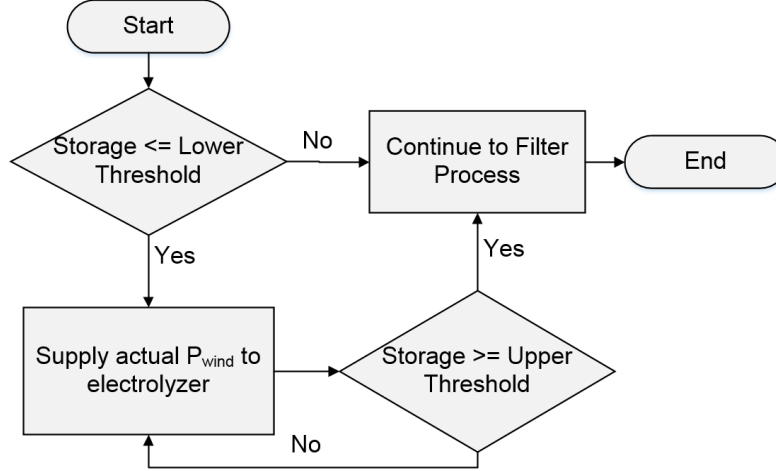
Fig. 2.18. Activation of electrolyzer.

$$P_{fcmax} = \begin{cases} P_{fc}^{nom} - \hat{P}_{t+k|t}^{w} & P_{fcmax,k} > 0 \\ 0 & P_{fcmax,k} \leq 0 \end{cases} \quad |\phi_{max}\Gamma_{fc} \leq \phi \tag{2.39}$$

where the nominal power of the FC is represented by P_{fc}^{nom}, and Γ_{fc} is the threshold of minimum percent of hydrogen stored for the FC to generate power; in case that the threshold cannot be met, the value of P_{fcmax} will be zero. Furthermore, P_{fcmax} is computed taking into account P_{fc}^{nom} to ensure that the max value asked from the FC will not be greater than the nominal power of the FC and to help linearize the output power of the HS.

The maximum power of the HS in this scenario will be determined as the sum of the wind power and the power from the FC given by $P_{fc,k} = P_{fc}^{nom} - \hat{P}_{t+k|t}^{w}$.

The sum of the power generated by the FC and forecast for the wind turbine will be filtered using (2.30) which will smooth the flickers, resulting in the reference for the MPC (2.37); simultaneously, this reference will be the output power of the HS.

2.5.2 Prioritizing constant output power level of the hybrid system

When the priority is to have an as much as possible constant output power from the HS, the resulting analysis of the previous scenario is of great importance. Because of the intermittence of wind speed, the appearance of many sags in the power forecast and actual power is common. To maintain a linear output power means the need to "sacrifice" other characteristics as, in this case, the magnitude of power supplied from the HS to the distribution network given by

$$P_{t+k|t}^{ref}[k] = \frac{a}{M} \sum_{j=0}^{M-1} P_{t+k|t}[k+j] \tag{2.40}$$

where a will take values between 0 and 1.

In this scenario, the filter at the control part of the model was modified from (2.30) as to have more energy stored and to decrease the output magnitude to 60% ($a = 0.6$) of the original power value. Thus the residual 40% will be supplied to the electrolyzer and consequently will generate hydrogen to store. The updated filtered signal will be the output power of the HS for the next hour.

2.6   Results and discussion

Each subsection from Section 2.5 focuses on the required characteristics needed to smooth and flatten the output power of the HS in order to overcome the intermittence of wind power.

When the HS is connected to the network, it will not destabilize the frequency as demonstrated in this section. The obtained results show the first week behavior of the HS, for the reader to notice in a clear way the dispatchability and reduction of intermittence in comparison to a system without the application of the proposed model as the actual wind power.

2.6.1   Active power delivered from the HS

The designed HS system is to be connected to the distribution network as mentioned before. From results, it can be seen how the unpredictability from the wind power (Fig. 2.17) is solved as shown in the HS active output power obtained with the proposed AEMS model (Fig. 2.19). The network frequency will not be affected considering that the HS output power can be dispatched according to the final user needs and the information can be sent to the SO with one hour prior.
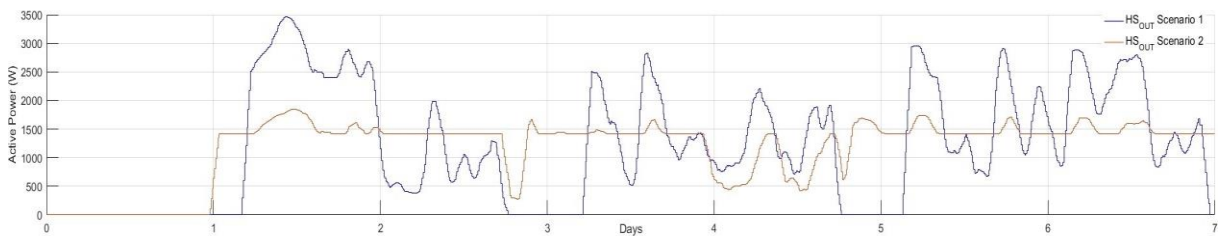
Fig. 2.19. Total power generated by the HS in both scenarios

Fig. 2.19 presents the HS output power for both scenarios. Results from the first scenario show that because of the periods of charge, the HS output power has periods of no power delivered to the network, the implementation of the constraints required to activate the electrolyzer, are also the moments of no power generated by the HS resulting from the electrolyzer consuming all the power generated by the wind turbine with the purpose of storing energy as hydrogen. Note in Fig. 2.19 that the response obtained from the second scenario, when compared to the first scenario, is flatter, more stable and more constant as it was expected.

Observing the results of the different scenarios, the HS output power can be adjusted to meet a specific load which modifies the trajectory followed by the MPC and the constraints applied. In addition, because of the flexibility of the MPC, the constraints that rule the charge and discharge of the hydrogen storage can be modified considering the purpose of the HS.

The reduction of volatility of the power delivered to the distribution network is noticeable, comparing the wind power from Fig. 2.17 and the output power of the HS from Fig. 2.19.

The output power of the HS is the sum of wind power with the power generated by the FC, as shown in Fig. 2.20, where the color at the base represents the power delivered from the wind turbine, and the color on top is the power delivered by the FC, showing how the wind power and FC complement each other.
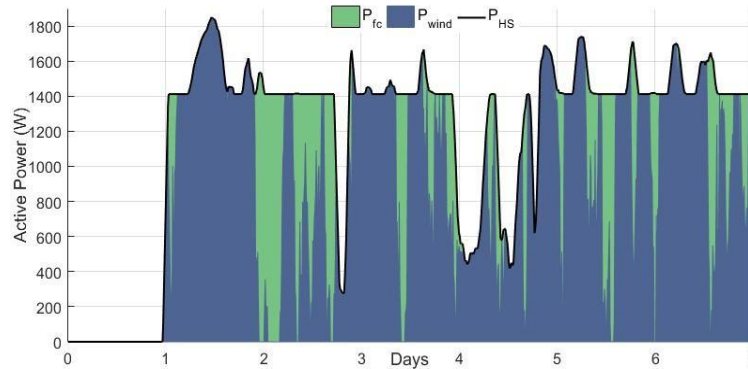
Fig. 2.20. Resources dispatch of the P_{HS} delivered to the grid.

2.6.2 Hydrogen storage behavior

The behavior of the hydrogen generated by the electrolyzer and consumed by the FC in the different scenarios can be seen in Fig. 2.21, where it can be noticed that when the electrolyzer works the hydrogen tank is charged and when the FC works the storage level of hydrogen will decrease.
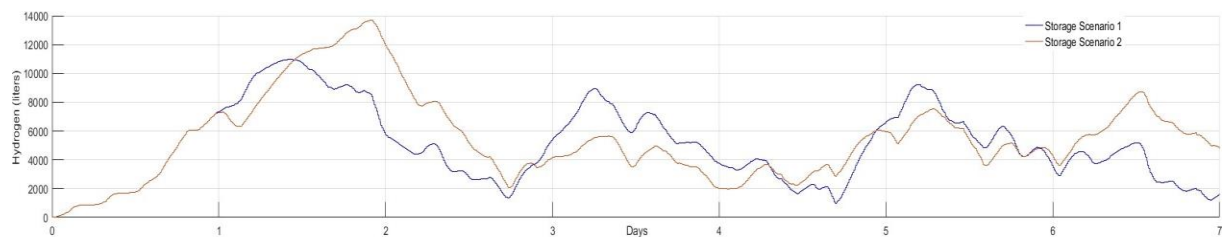
Fig. 2.21. Behavior of hydrogen storage in the different scenarios.

The storage constantly maintains a minimum level of hydrogen as shown in Fig. 2.21; thanks to this, the FC can work longer permitting a smooth or flat output from the HS.

Comparing the production and consumption of hydrogen from both scenarios, results show that there is 1.74% less production of H_2 and 9.93% less consumption of it in the second scenario at the end of the week. However, the storage of the second scenario presents 17.65% more hydrogen in comparison with the first scenario where it is almost empty as seen in Fig. 2.21. These results are a consequence of the level of power required in each scenario. The second delivers a lower level of active power to possess a more constant output at all time, in contrast to the first scenario, which due to the level of power delivered needs periods of zero output power as to generate H_2 to storage.

The storage from the first scenario always has a good level of hydrogen ready to be used by the FC in a more efficient way as in Fig. 2.21, but clearly because of the charging periods of hydrogen, the output power drops to zero at the output of the HS.

The hydrogen consumption is constant, and therefore, the tank will not reach a high level of storage, tending instead to maintain a lower mean of hydrogen, as shown in Fig. 2.21.

2.6.3 Findings of the method

Taking into account the importance of charging periods for the storage of hydrogen and of keeping an output power level as linear as possible, decreasing the output power level to generate hydrogen was required for longer periods of time and for the FC to work as backup power to have an almost linearized power level at the output of the HS.

The FC can act as a means of contingency to smooth the output power thanks to the hydrogen stored in the tank, and because of the decision making based on the forecast that gives information about future possible fast changes in wind power, it is possible the use of the FC as a measure for preventing disturbance of the frequency of the network.

The surplus of energy from the high peaks of wind power is saved as hydrogen for future implementation, making smooth wind power and semi-dispatchable HS generated power possible.

2.7   References

[1]   M. Bollen and F. Hassan, *Integration of distributed generation in the power system*. New Jersey: John Wiley & Sons, Inc., 2011.

[2]   Intelligent Energy - Europe, "Catalogue of european urban wind turbine manufacturers potx," 2011. [Online]. Available: http://123doc.org/document/1227748-catalogue-of-european-urban-wind-turbine-manufacturers-potx.htm. [Accessed: 25-Sep-2017].

[3]   Ballard, "Datasheet: FCgen-1300 - Ballard - PDF Catalogue | Technical Documentation | Brochure." [Online]. Available: http://pdf.directindustry.com/pdf/ballard/fcgen-1300/22779-383681.html. [Accessed: 25-Sep-2017].

[4]   FuelCellStore, "Datasheet: Electrolyzer specifications S20, S40." [Online]. Available: http://www.fuelcellstore.com/hydrogen-generator-s40. [Accessed: 25-Sep-2017].

[5]   Hb. Technologies, "Datasheet: HBank Technologies - Fuel Cell Application." [Online]. Available: http://www.hbank.com.tw/fc/16500.html. [Accessed: 25-Sep-2017].

[6]   G. Ramos Niembro, R. Fiscal Escalante, M. Maqueda Zamora, J. Sada Gámiz, and H. Buitrón Sánchez, "Variables que influyen en el consumo de energía eléctrica," *boletín iie*, vol. 23, pp. 11–18, 1999.

[7]   L. Jiang, S. Luo, and J. Li, "Intelligent electrical event recognition on general household power appliances," *2014 IEEE 15th Work. Control Model. Power Electron.*, pp. 1–3, 2014.

[8]   A. H. Mohsenian-Rad, V. W. S. Wong, J. Jatskevich, R. Schober, and A. Leon-Garcia, "Autonomous demand-side management based on game-theoretic energy consumption scheduling for the future smart grid," *IEEE Trans. Smart Grid*, vol. 1, no. 3, pp. 320–331, Dec. 2010.

[9]   G. Santamaría-Bonfil, A. Reyes-Ballesteros, and C. Gershenson, "Wind speed forecasting for

wind farms: A method based on support vector regression," *Renew. Energy*, vol. 85, pp. 790–809, Jan. 2016.

[10]   R. G. Kavasseri and K. Seetharaman, "Day-ahead wind speed forecasting using f-ARIMA models," *Renew. Energy*, vol. 34, no. 5, pp. 1388–1393, 2009.

[11]   G. Giebel, R. Brownsword, G. Kariniotakis, M. Denhard, and C. Draxi, "Report: The state of the art in short-term prediction of wind power," Denmark, 2011.

[12]   H. Madsen, *Time series analysis*, Technical. Copenhagen: Chapman & Hall/CRC, 2008.

[13]   J. V. Candy, *Model-based signal processing*. Santa Barbara, California: John Wiley & Sons, Inc. - IEEE Press, 2005.

[14]   G. E. P. Box, G. M. Jenkins, G. C. Reinsel, and G. M. Ljung, *Time series analysis : forecasting and control.*, 5th ed. New Jersey, USA: John Wiley & Sons, Inc., 2015.

[15]   T. Hastie, R. Tibshirani, and J. Friedman, *The elements of statistical learning*. New York, NY: Springer New York, 2009.

[16]   L. B. Rasmussen, P. Bacher, H. Madsen, H. A. Nielsen, C. Heerup, and T. Green, "Load forecasting of supermarket refrigeration," *Appl. Energy*, vol. 163, pp. 32–40, 2016.

[17]   S. Sumathi, L. Ashok Kumar, and P. Surekha, *Solar PV and wind energy conversion systems*. Cham: Springer International Publishing, 2015.

[18]   M. R. Patel, *Wind and solar power systems : design, analysis, and operation*. New York, NY: CRC Press, 2006.

[19]   T. Ackermann, *Wind power in power systems*, 2nd ed. Germany: John Wiley & Sons, Inc., 2012.

[20]   L. L. Lai and T. F. Chan, *Distributed generation : induction and permanent magnet generators*. London: John Wiley & Sons, Inc.-IEEE Press, 2007.

[21]   Danish wind industry association, "Descripción de las variaciones del viento: distribución de Weibull," *motiva*, 2014. [Online]. Available: http://drømstørre.dk/wp-content/wind/miller/windpower web/es/tour/wres/weibull.htm. [Accessed: 25-Sep-2017].

[22]   Asociación danesa de la industria eólica, "La rosa de los vientos," *2014*, 2014. [Online]. Available: http://intranet2.minem.gob.pe/web/archivos/dge/publicaciones/uso/1/01/02/08/es/tour/wres/rose.htm. [Accessed: 25-Sep-2017].

[23]   J. Machowski, J. W. Bialek, and J. R. Bumby, *Power system dynamics : stability and control*, 2nd ed. England: John Wiley & Sons, Inc., 2008.

[24]   TNEI-Services, "Appendix 8.6 Wind speed calculations," in *HMP standford hill wind energy development*, 2010, p. 7.

[25]   A. E. Feijoo and J. Cidras, "Modeling of wind farms in the load flow analysis," *IEEE Trans. Power Syst.*, vol. 15, no. 1, pp. 110–115, 2000.

[26]   M. Ragheb, "Report: Wind shear, roughness classes and turbine energy production," Illinois, USA, 2017.

[27]   International Electrotechnical Commission, *International Standard: IEC 61400-12-1 Wind turbine generator systems*. 2017, p. 860.

[28]   Danish wind industry association, "Wind Energy Concepts," 2003. [Online]. Available: http://drømstørre.dk/wp-content/wind/miller/windpower

web/en/stat/unitsw.htm#roughness. [Accessed: 25-Sep-2017].

[29]   M. Alimuzzaman and M. T. Iqbal, "Design of a control system for active and reactive power control of a small grid- connected wind turbine," *www.ijesci.org Int. J. Energy Sci.*, vol. 3, no. 5, pp. 304–310, 2013.

[30]   Peiyuan Chen, P. Siano, B. Bak-Jensen, and Zhe Chen, "Stochastic optimization of wind turbine power factor using stochastic model of wind power," *IEEE Trans. Sustain. Energy*, vol. 1, no. 1, pp. 19–29, Apr. 2010.

[31]   J. Hu, L. Shang, Y. He, and Z. Q. Zhu, "Direct active and peactive power regulation of grid-connected DC/AC converters using sliding mode control approach," *IEEE Trans. Power Electron.*, vol. 26, no. 1, pp. 210–222, Jan. 2011.

[32]   P. CortÉs, J. RodrÍguez, P. Antoniewicz, and M. Kazmierkowski, "Direct power control of an AFE using predictive control," *IEEE Trans. Power Electron.*, vol. 23, no. 5, pp. 2516–2523, Sep. 2008.

[33]   A. Bouafia, F. Krim, and J. P. Gaubert, "Fuzzy-logic-based switching state selection for direct power control of three-phase PWM rectifier," *IEEE Trans. Ind. Electron.*, vol. 56, no. 6, pp. 1984–1992, Jun. 2009.

[34]   J. Twidell and A. D. Weir, *Renewable energy resources*, 2nd ed. London: Taylor & Francis, 2006.

[35]   D. M. F. Santos, C. A. C. Sequeira, and J. L. Figueiredo, "Hydrogen production by alkaline water electrolysis," *Quim. Nova*, vol. 36, no. 8, pp. 1176–1193, 2013.

[36]   R. G. Ehl and A. J. Ihde, "Faraday's electrochemical laws and the determination of equivalent weights," *J. Chem. Educ.*, vol. 31, no. 5, p. 226, May 1954.

[37]   EG&G Technical Services Inc., *Fuel cell handbook.*, 7th ed. Virginia: U.S. Department of Energy, 2004.

[38]   C. Kunusch, P. Puleston, and M. Mayosky, *Sliding-Mode Control of PEM Fuel Cells*. London: Springer London, 2012.

[39]   C. Kunusch, P. F. Puleston, M. A. Mayosky, and J. J. Moré, "Characterization and experimental results in PEM fuel cell electrical behaviour," *Int. J. Hydrogen Energy*, vol. 35, no. 11, pp. 5876–5881, 2010.

[40]   J. Larminie and A. Dicks, *Fuel cell systems explained*, 2nd ed. UK: John Wiley & Sons, Inc., 2003.

[41]   N. Sammes, Ed., *Fuel Cell Technology*. London: Springer London, 2006.

[42]   Q. Yan, H. Toghiani, and H. Causey, "Steady state and dynamic performance of proton exchange membrane fuel cells (PEMFCs) under various operating conditions and load changes," *J. Power Sources*, vol. 161, no. 1, pp. 492–502, Oct. 2006.

[43]   A. Kannan, A. Kabza, and J. Scholta, "Long term testing of start–stop cycles on high temperature PEM fuel cell stack," *J. Power Sources*, vol. 277, pp. 312–316, 2015.

[44]   E. F. Camacho, C. Bordons, M. J. Grimble, and M. A. Johnson, *Model predictive control*. London: Springer London, 2007.

[45]   R. Halvgaard, N. K. Poulsen, H. Madsen, J. B. Jorgensen, F. Marra, and D. E. M. Bondy, "Electric vehicle charge planning using economic model predictive control," in *2012 IEEE International Electric Vehicle Conference*, 2012, pp. 1–6.

[46]   J. Maciejowski, *Predictive control with constraints*. Harlow, England ; New York: Prentice

Hall, 2002.

[47] S. W. Smith, *The scientist and engineer's guide to digital signal processing*, 2nd ed. San Diego, USA: California Technical Pub, 1999.

CHAPTER 3

HYBRID GENERATION OPERATION CONTROL FOR PROSUMER BEHAVIOR

In this chapter, a prosumer control system is proposed as an approach to reducing final user's load and in bringing active power to a designated value. The proposed control is suitable for distributed generation, by implementing a wind turbine, a set of photovoltaic cells, an electrolyzer, hydrogen storage and a polymer electrolyte membrane fuel cell embedded in a HS. The wind speed forecast algorithm implemented in the previous chapter, is applied to solar radiation data from the same place. This approach provides complete control of the prosumer energy system, thanks to the probabilistic information from short-term wind and radiation forecast generation. A prosumer control method based on model predictive control to manage the generation system is presented.

3.1   Introduction

Today's electric networks are undergoing drastic changes, going from being operated and controlled in a hierarchical way to operate as open markets. Technological developments and policy measurements intended to combat climate change, electrical markets, and network architectures are some of the driving forces [1]. Therefore, there has been an increasing interest in microgrids; as a consequence, the distribution systems are exposed to the impact of distributed generation (DG) units together with energy storage and controllable loads. Emerging technologies such as DG units, hybrid electric vehicles, and demand response introduce considerable complexity to grids in the operation and control at low (LV) and medium voltage (MV).

To confront these complexities, a change in the current electricity market is foreseen with various makers, and the prosumer concept is one of the main focuses to be implemented [2], [3]. The aim of this chapter is to introduce a prosumer control system, carried out in a power generation system based exclusively on renewables for demand-side management and constant power generation with power factor adjustment. The proposed prosumer considers the grid code to maintain a stable power factor and frequency at the connection bus of the distribution network.

Unlike other studies, a flexible prosumer control for resource management and frequency stability based on forecast analysis is proposed, depending exclusively on renewable energies.

In this chapter, the concepts and mathematical models required for the generation system and prosumer control development will initially be found. Afterwards, it will be explained the methodology and structure of the prosumer EMS, with the elements involved at each stage. Two different scenarios will then be established with their required constraints for analyzing the response and have a final discussion.

3.2   Prosumer

A prosumer can be defined as one who is both producer and consumer, and prosumption involves a combination of production and consumption [4]. In addition, [5], [6] argue that consumers are a phenomenon of the industrial age. As society moves forward, the number of pure consumers will decline. They will be replaced by "prosumers", people who produce many of their own goods and services. Prosumer as a concept is sufficiently provocative to merit the attention of consumer behavior scholars and marketing practitioners. Prosumption has its most obvious and direct relevance to the economy [7].

Power system participants have been strictly producers or consumers of electricity. Today, distributed renewable energy sources, storage, and demand response allow the consumer to produce and to store energy [8]. This new emerging entity is called the "prosumer", an economically motivated entity that

- Consumes, produces, and stores power
- Operates or owns a power grid, and hence transports electricity, and
- Optimizes the economic decisions regarding its energy utilization.

The prosumer may consist of a combination of components: energy sources, loads, storage, and an electric grid. The prosumer also contains controls to operate its system and other economic decision-making systems. The prosumer has a set of functions associated with interactions to the external world, such as consuming or producing energy and participating in the market.

Components such as the external energy source or any combination of the components can be seen as prosumers acting as loads, energy sources, transmission, or storage [8]. The concept of prosumer can be extended and used to model the entire existing electricity infrastructure as shown in Fig. 3.1.
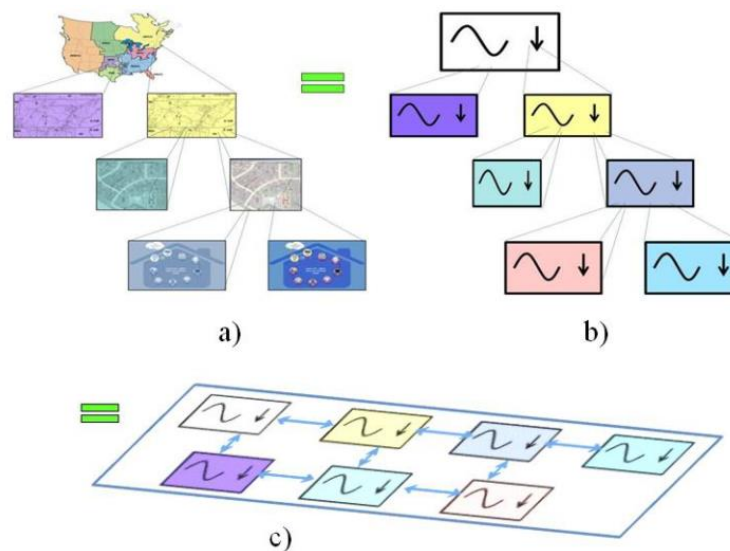
Fig. 3.1. Logical equivalence of electric power systems' prosumers: a) existing hierarchical industry paradigm, b) all power systems modelled as prosumers, and c) prosumers seen as same level entities [8].

It is critically important to note that the prosumer abstraction shown in Fig. 3.1 allows us to claim the following: a) Any power system can be represented as a prosumer; b) Prosumers currently organized in a hierarchical structure interact only with other prosumers; c) Prosumers can interact with all the other prosumers at the same level, and d) Because prosumers can contain all the components of electric power systems (production, storage, transportation, and consumption), all the interactions associated with electricity can be modelled through interactions between prosumers [8].

An architecture based on prosumer interaction can, therefore, be proposed. In this architecture, all prosumers are located at the same level interacting through common interfaces. Thus, the production and the storage of electricity shifts to the low voltage network [9]. Such a network will be characterized by many electricity producing and consuming households, so-called prosumers. Prosumers have the capacity to attain a certain level of self-sufficiency and can participate more actively in the network than today's households if connected to the grid. The emerge of electricity prosumption will change the structural attributes of the network [10] and lead to various forms as shown in Fig. 3.2.
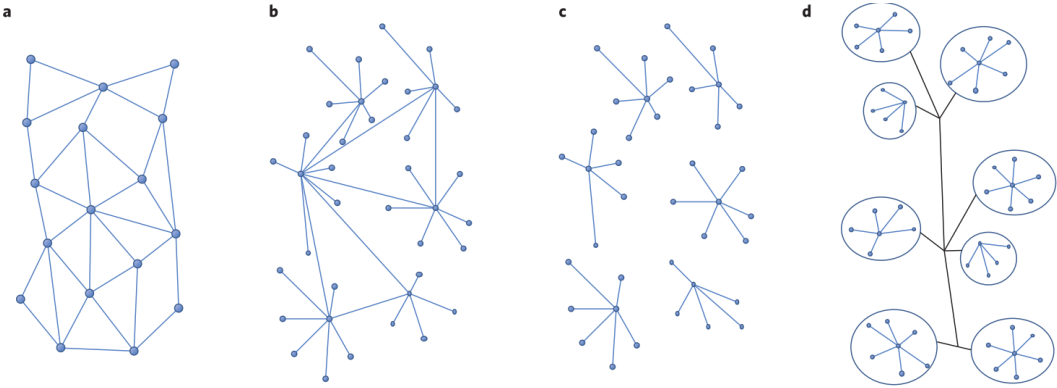
Fig. 3.2. Structural attributes of prosumer markets [10].

Prosumer communities have organizational and geographical boundaries and can be connected to the grid or operate as a stand-alone island solution. The crowd energy (CE) concept represents a prosumer community with defined boundaries and grid access and is based on the technical as well as on the human cooperation capacities of its members [11]. Within the CE community, households, so-called iGSL cells (intelligent generation-load-storage), use their infrastructural assets to implement the energy turnaround collectively [11]. Individual electricity surplus can be either shared by other community members or be stored, as in Fig. 3.3.

Benefits of such an electricity network structure or of the smart grid are presented from a system's point of view [12]–[14]. Here, a semi-dispatchable hybrid system is proposed to work as a prosumer at the distribution level.

In this research, the prosumer is reflected in a HS based on non-conventional renewable energies as generation and a controlled load as the consumer.
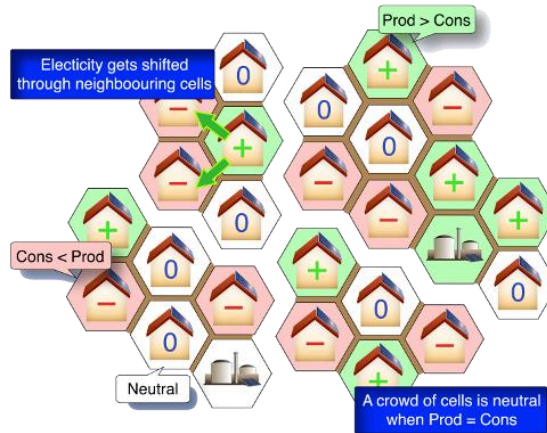
Fig. 3.3. Crowd energy concept [11].

3.2.1 Hybrid system setup and modeling

The hybrid system employed in Chapter 2 and explained in Section 2.1 is updated with a small PV plant. The PV plant consists of a 3 kW KC200GT PV array [15] which increases the active power available to be managed. Fig. 3.4 shows the updated HS; the continuous, dashed and pointed lines represent the active power, signal control, and hydrogen flow, respectively. The SWT and PV output active power will be used to produce hydrogen or send it to the grid. Hydrogen is stored and supplied to the FC to generate active power as required. In contrast to the HS proposed in Chapter 2, the proposed prosumer EMS computes its power trajectory considering its constraints, depending on the final user needs. The EMS of the HS is the decision maker based on the prosumer control developed, which takes into account the final user needs without disturbing the distribution network at the connection point.
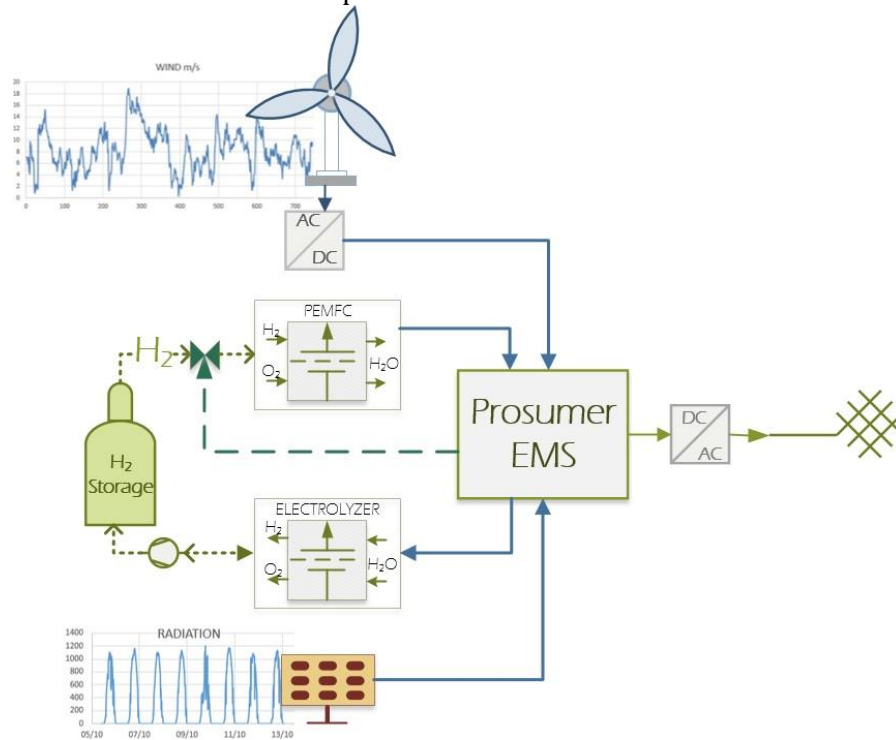
Fig. 3.4. Wind-PV-FC generation system.

The prosumer control is determined by the objective function and constraints applied in the MPC. The objective function contemplates the active power of each element, including the stored power. The constraints consider the physical limits of the fuel cell, electrolyzer and hydrogen storage (P_{fc}^{nom}, P_{ele}^{nom}, φ_{max}), the dynamic model of each element (l) related to the hydrogen flow (φ) and the behavior of the output power ($P_{t+k|t}^{ref}$). The implemented HS, described in Fig. 3.4, is developed to be connected to the distribution network at a residential area as a prosumer. The HS can be adjusted to generate a constant output power, as well as to meet a reference trajectory. The HS is based on load data from households and mini-stores, considering the size of the HS and the needs of the final user.

3.2.2 Photovoltaic model

A PV system is composed of several photovoltaic solar cells; each cell can generate 1 - 2 W, depending on the material used. The cell equivalent circuit for a crystalline type is described in Fig. 3.5.
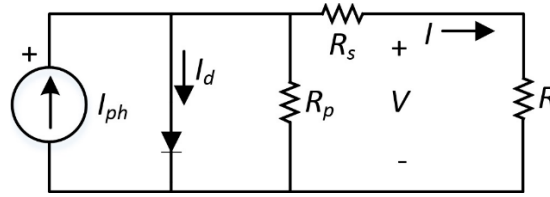
Fig. 3.5. Cell equivalent circuit.

The parameter R_s is the cell resistance, which represents the semiconductor material resistance. Moreover, R_p is the cell shunt resistance, and V is the output voltage; this stands for losses caused by the leakage current [16]. From the cell circuit in Fig. 3.5, the output current I can be calculated as

$$I = I_{pv} - I_0 \left[\exp\left(\frac{V + R_s I}{V_t \alpha}\right) - 1\right] - \frac{V + R_s I}{R_p} \tag{3.1}$$

where

$$V_t = \frac{k_{pv} T}{q}, \tag{3.2}$$

in which k_{pv} is Boltzmann's constant, q is the electronic charge, T is the ambient temperature in °K, I_0 is the saturation current and α is the diode quality factor, which takes values between 1 and 2 because of the germanium and silicon material.

Additionally, we consider the cell design variables: for instance, the nominal open-circuit voltage ($V_{oc,n}$), the nominal short-circuit current ($I_{sc,n}$), the voltage at the maximum power point (MPP) (V_{mp}), the current at the MPP (I_{mp}), the open-circuit voltage/temperature coefficient (K_v), the short-circuit current/temperature coefficient (K_i), and the maximum experimental peak output

power ($P_{max,e}$). It is assumed that $I_{sc} \approx I_{pv}$ in the modeling of PV devices because the series resistance is low, contrary to the parallel resistance [17]. The diode saturation current is given by

$$I_0 = \frac{I_{sc,n} + K_i\Delta T}{\exp\left(\dfrac{V_{oc,n} + K_v\Delta T}{\alpha V_t}\right) - 1}.$$

(3.3)

The current I_{pv} is linear with respect to the temperature, by using a constant radiation level deduced as [16]

$$I_{pv} = \left(I_{pv,n} + K_i\Delta T\right)\frac{G}{G_n},$$

(3.4)

in which

$$I_{pv,n} = \frac{\left(R_p + R_s\right)}{R_p}I_{sc,n},$$

(3.5)

where G is the actual radiation and G_n is the nominal radiation. The relation between R_s and R_p may be found by making $P_{max,m} = V_{mp}I_{mp} = P_{max,e}$. By solving the resulting equation for R_s, we obtain

$$P_{max,e} = V_{mp}\left\{I_{pv} - I_0\left[\exp\left(\frac{V_{mp} + R_sI_{mp}}{\alpha V_t}\right) - 1\right] - \frac{V_{mp} + R_sI_{mp}}{R_p}\right\}$$

(3.6)

$$R_p = \frac{V_{mp}\left(V_{mp} + R_sI_{mp}\right)}{V_{mp}I_{pv} - V_{mp}I_0\left[\exp\left(\dfrac{V_{mp} + R_sI_{mp}}{V_t\alpha}\right)\right] + V_{mp}I_0 - P_{max,e}}.$$

(3.7)

From (3.7), clearly for each value on resistance R_s, there is a R_p which describes the I-V curve that passes by the experimental point V_{mp} and I_{mp}. The goal is to find the values of R_s and R_p that match the max point of the P-V curve with the experimental one with an iterative function updating the values R_s and R_p in each iteration until the correct values are found.

The initial value of R_p is given by the slope of the line between the short-circuit and the experimental maximum point of power at 50°C, shown in Fig. 3.6 and deduced as
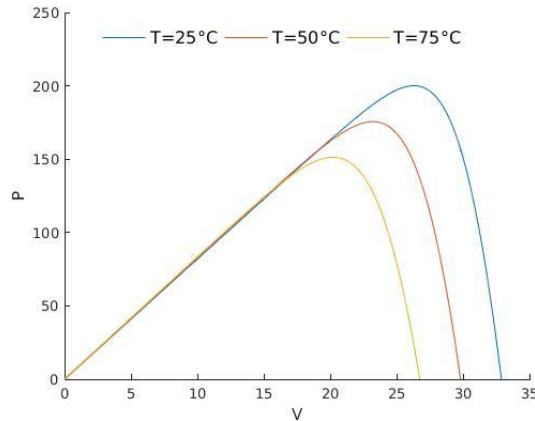
Fig. 3.6. P-V curve at different temperatures for a KC200GT PV panel.

$$R_{p,ini} = \frac{V_{mp}}{I_{sc,n} - I_{mp}} - \frac{(V_{oc,n} - V_{mp})}{I_{mp}} . \tag{3.8}$$

When the values R_s and R_p that match the maximum point of the P-V curve with the experimental one are found, these values are integrated into (3.1) to calculate the respective current. Consequently, (3.9) is solved to compute the active power generated by the PV cell

$$P = V \left\{ I_{pv} - I_0 \left[\exp\left(\frac{V + R_s I}{\alpha V_t}\right) - 1 \right] - \frac{V + R_s I}{R_p} \right\} . \tag{3.9}$$

3.3   Prosumer management system

The prosumer management was developed by implementing MPC, together with a time series analysis algorithm to compute the forecast, and the models of the elements that integrate the generation system by applying the forecast model explained in Section 2.2.1. Fig. 3.7 shows the structure of the prosumer management, where at the end of the first column the wind and radiation power is forecasted and implemented by the MPC. The upper part of Fig. 3.7 shows the forecast behavior for the next hour. In addition, the MPC considers the values at that moment of the storage level and the FC saturation power value for managing the power.
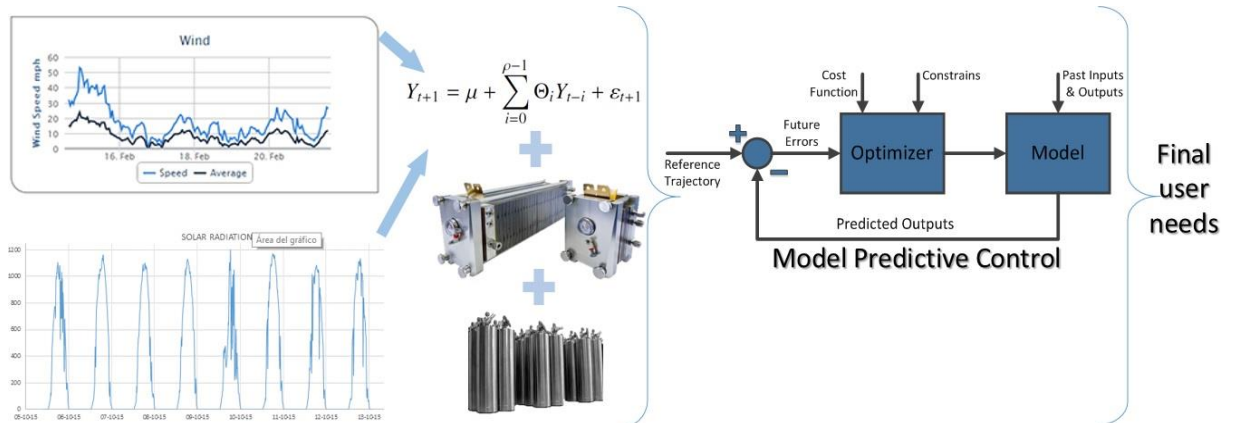
Fig. 3.7. Structure of the prosumer management system.

The block diagram in Fig. 3.7 represents the basic structure of the MPC, where different strategies can be implemented to control many processes including unstable systems [18]–[20]. The implemented strategies are reflected in the objective function and constraints dedicated to managing the energy as required by the final user.

Remembering (2.9), the predicted outputs for an N horizon are forecasted for an instant t; the forecasted outputs for $k = 1, \ldots, N$ depend on the historic data until instant t, the objective function, and the constraints. The prediction will be updated every 10 minutes as to always have an hour-ahead forecast.

The reference trajectory $P_{t+k|t}^{ref}$ is computed by the MPC taking into account the objective function and constraints on account of the FC, electrolyzer and generated power forecasted. Furthermore, the trajectory can be given considering the final user needs, which eliminates the variability given

by the wind and PV generation. Furthermore, $P_{t+k|t}^{ref}$ can be represented by the user's load curve or be computed by the MPC considering the physical constraints of the components, level of storage and the slope of output power as to not disturb the frequency of the system.

The proposed prosumer EMS is based on the fact that the frequency can be controlled through active power management on the HS, as explained in Appendix B.

3.4   Prosumer scenarios management

Unlike the algorithm proposed in Chapter 2, where the power reference trajectory is assessed in a separate algorithm, in this section, the MPC computes the power reference trajectory based on the system constraints. The prosumer scenarios' aim is to manage the system energy; it is important to clarify that any costs derived by this action are out of this study scope. Two scenarios are accomplished to validate the proposed algorithm as a prosumer control system. i) Power management subjected to a designated value and ii) prosumer for demand-side management. In both scenarios, a zero network frequency disturbance is also targeted.

The daily power generated by wind turbine and PV combined, without performing a power management method, is presented in Fig. 3.8. The proposed power managements independently use the power generated by each device, with the consideration of further flexibility when market employment is required by the final user.
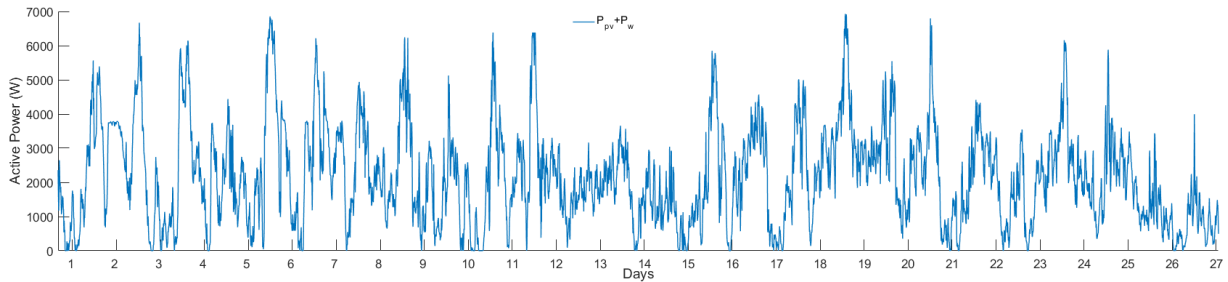
Fig. 3.8. Actual power generated by the wind turbine and PV system.

3.4.1 Power management subjected to a designated value

This scenario task is to manage the system output power by keeping a specific value (P_{value}); it is premeditated for energy storage to prosumer employment, with the possible implementation of dispatch considering power factor and cost behavior when connected to the grid. Furthermore, when implemented on a large scale as DG or in a prosumer community, it draws the steady-state power factor deviation to the nominal value by considering the grid code through active power management.

The algorithm used is presented in Fig. 3.9. Initially, the FC, electrolyzer, and storage step response are computed as explained in Section 2.2 and described in Fig. 2.8. Afterwards, the forecast algorithm separately estimates the hour ahead wind speed and radiation, for energy regulation at the MPC level and future energy dispatch. The voltage angle θ at PCC is considered when is required from the HS a power factor improvement.
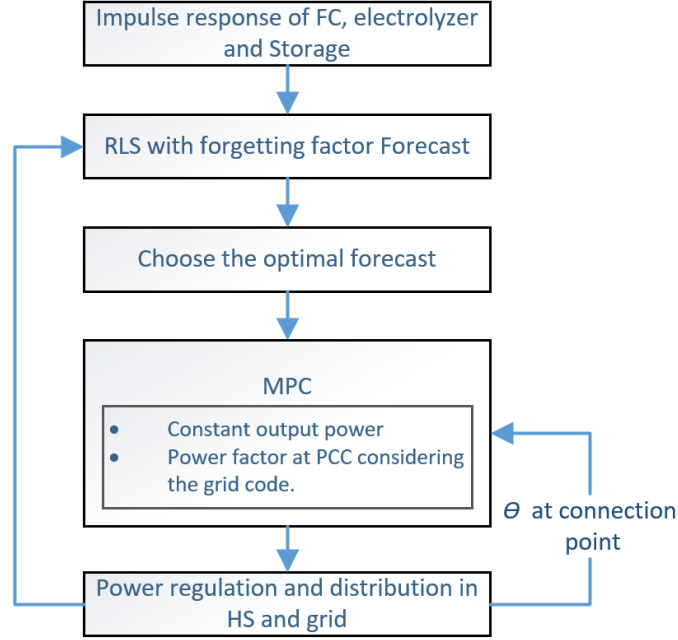
Fig. 3.9. Structure of the prosumer management system.

The MPC manages the generation system according to the objective function and constraints. The objective function of the generation system presented in Fig. 3.1 is deduced as

$$\min_{P_{\theta,k}} \left\| P_{w,k} + P_{pv,k} - P^{ref}_{t+k|t,k} + P_{\phi,k} \right\| \tag{3.10}$$

representing the system power balance. Most variables were described in Section 2.3: $P_{pv,k}$ is the vector with the actual PV power ($k = 0$) and forecasted PV power ($k = 1, \dots, N$) meaning $P_{pv} = [P^{pv}_{k=0}, \hat{P}^{pv}_{t+k|t}]$. The restrictions implemented in this stage are

$$subject\ to \quad \phi = \sum_{k=0}^{N} -l_{fc}P_{fc,k} + l_{el}P_{el,k} + l_{st,k}\phi_0$$
$$0 \leq \phi \leq \phi_{max}$$
$$-P^{nom}_{ele} \leq P_{\phi,k} \leq P^{nom}_{fc}$$
$$P_{\phi,k} = P_{fc,k} - P_{el,k}$$
$$0 \leq P_{el,k} \tag{3.11}$$
$$0 \leq P_{fc,k}$$
$$P^{ref}_{t+k|t,k} \leq P_{ref} + 0.05P_{ref}$$
$$P^{ref}_{t+k|t,k} \leq P_{value}$$
$$P^{ref}_{t+k|t,k} \geq P_{ref} - 0.05P_{ref}$$

Note that some constraints consider the slope to avoid abrupt power changes and disturbance of the network's frequency considering the grid code. By using the constraints, we can also consider the level of hydrogen for maintaining a minimum level in case of contingency.

By adjusting P and Q independently, frequency and amplitude of the grid voltage are determined. The voltage angle θ can be controlled by regulating P, specifically attaining control over the load at the distribution level as explained in Appendix B.

The aim of the prosumers from the frequency regulation point of view is to drive the steady-state frequencies and power levels to the desired values. To perform power factor regulation at the connection point, the voltage angle θ is monitored, the constraint $P_{t+k|t,k}^{ref} \leq P_{value}$ is modified to $P_{t+k|t,k}^{ref} \leq P_{value} + P_\theta$, and P_θ is computed as

$$P_\theta = \begin{cases} 0.05P_{ref} & \theta_0 - \theta > 0 \\ 0 & \theta_0 - \theta = 0 \\ -0.05P_{ref} & \theta_0 - \theta < 0 \end{cases}, \tag{3.12}$$

where θ_0 represents the angle nominal value and θ is the voltage angle at instant t in the connection bus.

For the prosumer to manage the energy considering cost behavior the constrain $P_{t+k|t,k}^{ref} \leq P_{value}$ is modified to $P_{t+k|t,k}^{ref} \leq P_{value} + P_{cost}$ and P_{cost} is computed as

$$P_{cost} = \begin{cases} 0.05P_{ref} & \text{cost} < \text{set value} \\ 0 & \text{cost} = \text{set value} \\ -0.05P_{ref} & \text{cost} > \text{set value} \end{cases}. \tag{3.13}$$

It is worth mention that the cost management depends on the country regulations.

3.4.2 Prosumer method for demand-side management

Demand-side management has been an important element of the electric utility planning approach and is referred to as integrated resource planning. A known definition of demand-side management is the planning, implementation, and monitoring of those utility activities designed to influence customer use of electricity in ways that will produce desired changes in the utility's load shape, i.e., changes in the time pattern and magnitude of a utility's load. Utility programs falling under the umbrella of demand-side management include the following: load management, new uses, strategic conservation, electrification, customer generation, and adjustments in market share [21].

In general, demand-side management embraces the following critical components of energy planning [21]:

- It will influence customer use. Any program intended to influence the customer's use of energy is considered demand-side management.

- It must achieve selected objectives. To constitute a desired load shape change, the program must further the achievement of selected objectives; that is, it must result in reductions in

average rates, improvements in customer satisfaction, achievement of reliability targets, etc.

- It will be evaluated against non-demand-side management alternatives. The concept also requires that selected demand-side management programs further these objectives to at least as great an extent as non-demand-side management alternatives, such as generating units, purchased power, or supply-side storage devices. In other words, it requires that demand-side management alternatives be compared to supply-side alternatives. It is at this stage of evaluation that demand-side management becomes part of the integrated resource planning process.

- It identifies how customers will respond. Demand-side management is pragmatically oriented. Normative programs (we ought to do this) do not bring about the desired positive efforts (if we do this, that will happen) are required. Thus, demand-side management encompasses a process that identifies how customers will respond not how they should respond.

- Its value is influenced by load shape. Finally, this definition of demand-side management focuses on the load shape. This implies an evaluation process that examines the value of programs according to how they influence costs and benefits throughout the day, week, month, and year.

The purpose of the prosumer method for demand-side management is to reduce to a minimum the load shape of the final user and even reach a non-demand management considering the available resources. The proposed approach is an integrated resource planning, where the management process involves the consistent evaluation of demand-side to supply-side alternatives. The target user is the residential and commercial sector associated with the low and medium power level network.

As mentioned before, an MPC is a discrete-time control approach, in which at each time step, the controller uses a system model to predict outputs over a finite-time prediction horizon and then determine the optimal choice of the control inputs for a defined control horizon [21]. As aforementioned, the algorithm refinement determining the prosumer method for demand-side management occurs at the MPC level.

The process flowchart presented in Fig. 3.10, is very similar to the one implemented in Section 2.4 and Section 3.4.1, with the difference that in this case the final user's load is taken into consideration, meaning that the voltage angle θ is not considered at the MPC level.

With the computed forecast and implementation of the models for the different elements that integrate the HS, the objective function can be deduced and incorporated to be minimized in the MPC. The system objective function is (3.10), representing the power balance in the generation system.

In this case, the power trajectory is managed by taking into account the final user's load curve, which in this case is the load curve of a small Mexican store [22]; as a result, the constraints are established as follows
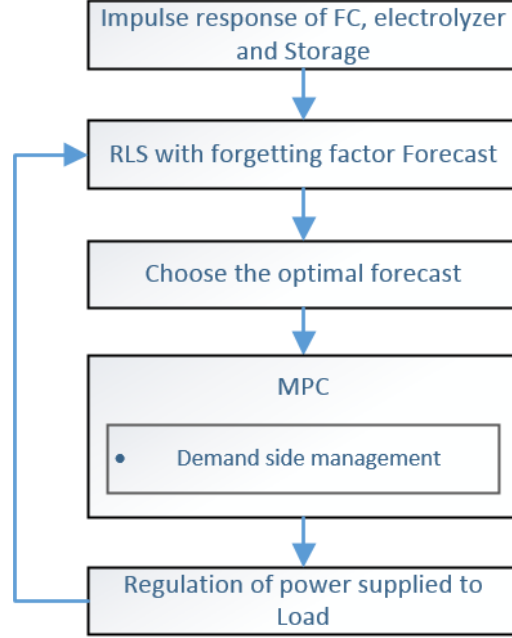
Fig. 3.10. Demand management flowchart.

$$subject\ to \quad \phi = \sum_{k=0}^{N} -l_{fc}P_{fc,k} + l_{el}P_{el,k} + l_{st,k}\phi_0$$

$$0 \leq \phi \leq \phi_{max}$$
$$-P_{ele}^{nom} \leq P_{\phi,k} \leq P_{fc}^{nom}$$
$$P_{\phi,k} = P_{fc,k} - P_{el,k} \qquad\qquad , \qquad\qquad (3.14)$$
$$0 \leq P_{el,k}$$
$$0 \leq P_{fc,k}$$
$$P_{t+k|t,k}^{ref} \leq P_{load}$$

where the load power is considered as the power trajectory of the HS.

3.5   Results and discussion

The power dispatch obtained from the start-up through the first 27 days by applying the proposed method in the first scenario is shown in Fig. 3.11, where the yellow color represents the power generated by the PV, the green color is the power generated by the SWT, and the blue color is the one generated by the FC.

In the same time period, the hydrogen storage performance for the first scenario is presented in Fig. 3.12. As seen, a zero hydrogen level is assumed at the start-up of the system.

Regardless, the system was tested for a longer period of time, resulting in similar hydrogen storage behavior and same lineal output power. It is worth mentioning that the first 27 days of results are shown, so the reader has a clear understanding of the results.
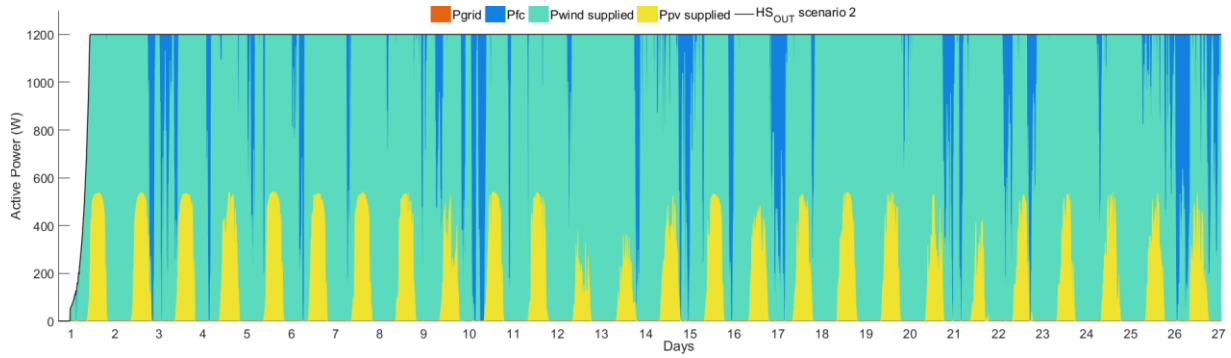
Fig. 3.11. Total power generated by the system.
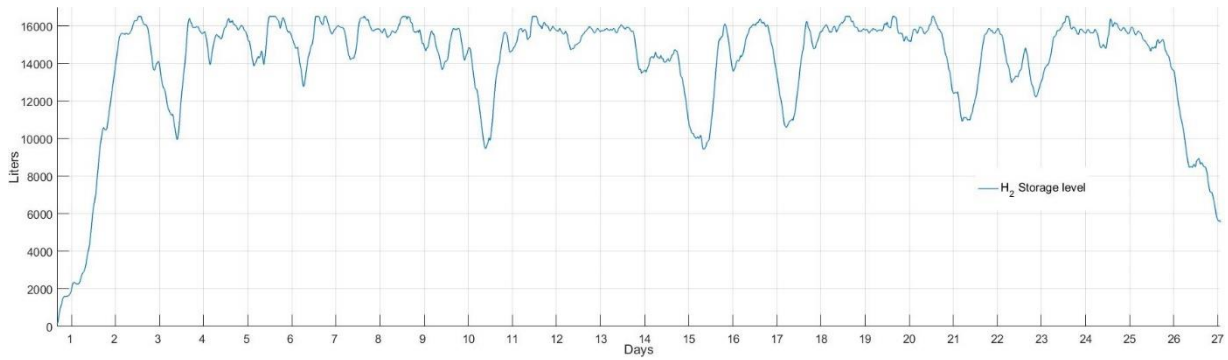
Fig. 3.12. Hydrogen storage behavior.

Fig. 3.13 to Fig. 3.15, reveal the impact on the power load supplied by the grid, and the hydrogen storage behavior achieved when the second scenario is simulated. The actual final user's load curve, as well as, observed load curve from the perspective of the grid is shown in Fig. 3.13.
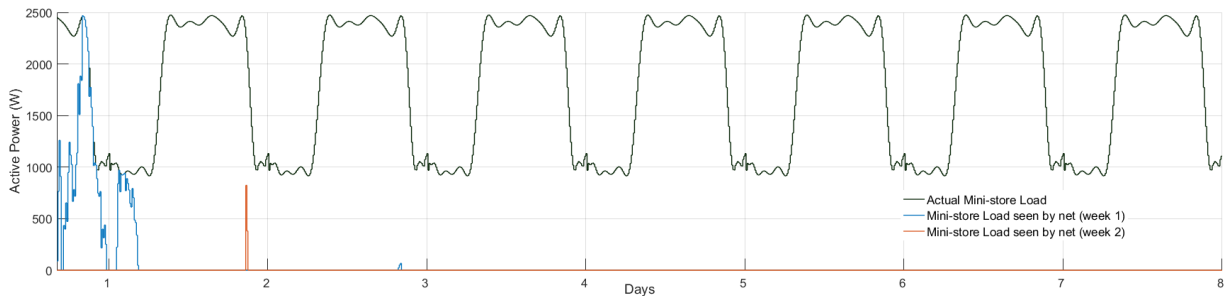
Fig. 3.13. HS power for load curve dispatch.

Two different week dispatches are presented to display the obtained results. The first week shows the working scenario since the connection with empty storage, whereas the second week was chosen randomly after a period of time from the start-up. The second scenario outcome associated with the active power dispatch can be seen in Fig. 3.14. Moreover, the dispatch power hierarchy has as a base the power from the SWT and the PV, yellow for PV generation and green for SWT generation, which are the first to be supplied to accomplish P_{ref}. The second instance is

the power "backup" provided by the FC represented by the blue color, and the last resource is the power from the grid presented in orange.
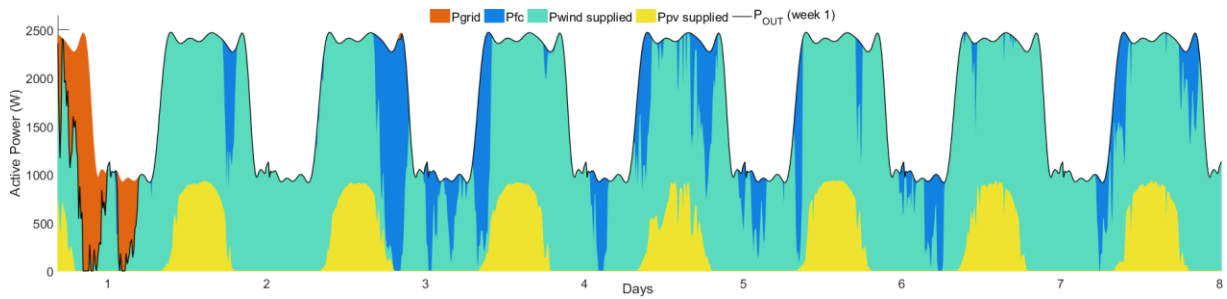
(a)
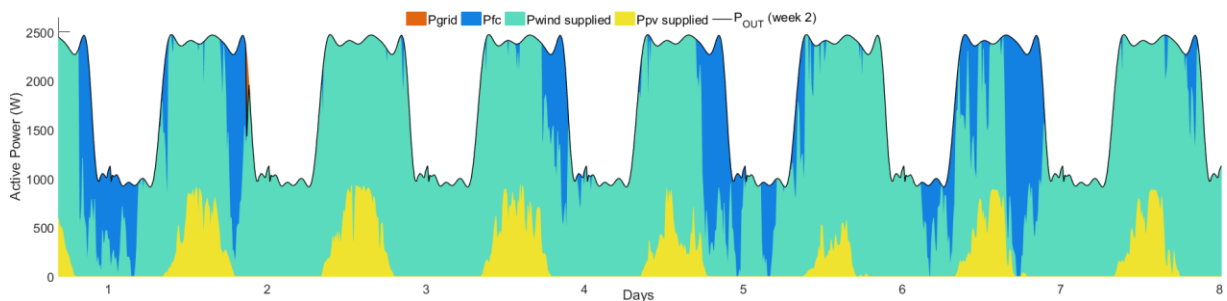
(b)

Fig. 3.14. Power load resource dispatch: (a) week 1 and (b) week 2.

Finally, the hydrogen behavior for the evaluated two weeks can be seen in Fig. 3.15. The primary focus, in the storage behavior, is that it has good hydrogen levels at all times after the start-up.
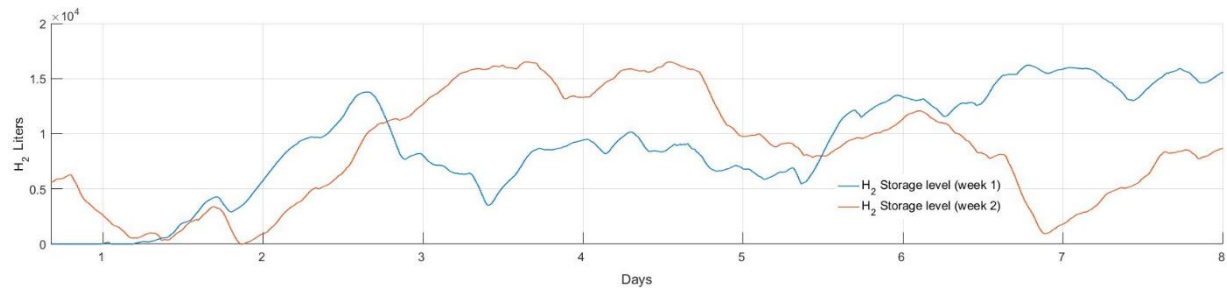
Fig. 3.15. Hydrogen storage for load curve dispatch.

3.5.1 Active power generated

Fig. 3.11 shows that a constant supply to the grid is possible without disturbing the constant output power and/or network characteristics, making possible the interaction with the market or even stabilizing the power factor at the connection bus.

A substantial load reduction is seen in Fig. 3.13, satisfying the purpose of prosumer on the demand-side. It is observed how the network is implemented as a final backup power supply to meet the load; this is reflected more in the first day of operation because of the lack of hydrogen stored. On a random week after the system start-up, it is noticeable that the grid only makes a very small contribution (at the end of the second day) in fulfilling the load required by the user; as for the following days, a zero load is detected by the network. Because of the aforementioned, it can be concluded that from the network's point of view most days the load was reduced, reaching a zero value.

The dispatch hierarchy, Fig. 3.11 and Fig. 3.14, was established so that the wind and PV generated power are the first to be supplied to the load (green), followed by the power generated by the FC (blue), and finally requested power from the network (orange).

The proposed prosumer control scenarios, consider the future one hour ahead forecasted wind and PV power generation preventing the SO about the future power supplied/required for the user; this to avoid the disruption of the network stability.

Note that the power dispatch by the SWT and the PV, along the presented results, were 85.74%, 78.71% and 76.86% for the first and second scenarios over the two weeks results. In contrast, the power supplied by the FC was 14.26%, 17.96%, and 23.07%, respectively. As observed by the percentage results, the backup power required from the network was minimum, only 3.33%, and 0.07%, respectively in the two-week results of the last scenario.

3.5.2 Hydrogen behavior in the system

The hydrogen behavior is determined by the final user, the FC and electrolyzer conversion rate, and prosumer control constraints. When the required power supply is a constant generation by the system, a fine hydrogen level storage at all times is essential, as noticed in Fig. 3.12. Consequently, in case of low wind or PV power generation, the system can still fulfill the constant output power. This behavior opens the doors to a more economically advantageous approach for participating in the electrical market and/or reassuring the frequency value when connected on a large scale to the grid.

It is appreciable in Fig. 3.12 and Fig. 3.15 how the first scenario has a better hydrogen level than the second. In the first case, because of the designated constant power generation, the hydrogen storage presents an average level of 85.57% at all times, which in comparison with the second scenario, the average stored levels in both weeks were 54.16% and 51.66%, respectively.

Confronting the obtained data, it can be noted that in the first case there was roughly 6% less hydrogen consumption than in the second case; this is caused by the power trajectory decided in each case constraints at the MPC and in the specifications of the prosumer control to be implemented.

The power surplus, in respect to the trajectory power (P_{ref}), will be consumed by the electrolyzer in order to generate hydrogen for storage, observed in Fig. 3.12 and Fig. 3.15 when the slope is positive. On the other hand, the hydrogen consumption by the FC is detected with a negative slope in the hydrogen storage behavior.

Even though the second scenario demands more output power than the first scenario, Fig. 3.15 displays that usually there is a fine hydrogen level stored.

3.5.3 Findings of the method

The systems were designed to be connected to the distribution network. From the results, it can be seen that with only a few modifications the prosumer control can be adjusted to achieve the final user's need, demonstrating its flexibility, while taking into account the storage capacity and generation resources.

Results show that the system can work with or without "backup" from the power grid depending on the size of the HS and the needs of the final user. Furthermore, the HS power generation can be stored for later use or injected into the grid if a market is considered, without changing the original characteristics of the grid.

Comparing the hydrogen behavior from the study cases, it can be seen how the hydrogen flow is influenced by the prosumer control output power conditions. In the first case in Fig. 3.12, there is always a fine level of hydrogen, while in the second case in Fig. 3.15 the average storage level drops. These behaviors are caused by the generation required from the FC in both cases.

3.6   References

[1]   Smart grid task force, "Report: Regulatory recommendations for the deployment of flexibility," EU, 2015.

[2]   S. Grijalva and M. U. Tariq, "Prosumer-based smart grid architecture enables a flat, sustainable electricity industry," in *Innovative smart grid technologies (ISGT), IEEE PES*, 2011, pp. 1–6.

[3]   S. Grijalva, M. Costley, and N. Ainsworth, "Prosumer-based control architecture for the future electricity grid," in *IEEE International Conference on Control Applications (CCA)*, 2011, pp. 43–48.

[4]   G. Ritzer, P. Dean, and N. Jurgenson, "The coming of age of the prosumer," *Am. Behav. Sci.*, vol. 56, no. 4, pp. 379–398, Apr. 2012.

[5]   A. Toffler, *The third wave*. New York, NY: Bantam Books, 1981.

[6]   P. Kotler, "The prosumer movement : a new challenge for marketers," *Adv. Consum. Res.*, vol. 13, pp. 510–513, 1986.

[7]   G. Ritzer and N. Jurgenson, "Production, consumption, prosumption," *J. Consum. Cult.*, vol. 10, no. 1, pp. 13–36, Mar. 2010.

[8]   S. Grijalva and M. U. Tariq, "Prosumer-based smart grid architecture enables a flat, sustainable electricity industry," in *Innovative smart grid technologies (ISGT), IEEE PES*, 2011, pp. 1–6.

[9]   H. Yves and S. Teufel, "Prosumer communities: Electricity as an interpersonal construct," in

2016 International Conference on Smart Grid and Clean Energy Technologies (ICSGCE), 2016, pp. 89–94.

[10] Y. Parag and B. K. Sovacool, "Electricity market design for the prosumer era," *Nat. Energy*, vol. 1, no. 4, p. 16032, 2016.

[11] S. Teufel and B. Teufe, "The crowd energy concept," *J. Electron. Sci. Technol.*, vol. 13, no. 3, pp. 263–269, 2014.

[12] C. R. Karger and W. Hennings, "Sustainability evaluation of decentralized electricity generation," *Renew. Sustain. Energy Rev.*, vol. 13, no. 3, pp. 583–593, Apr. 2009.

[13] N. D. Sintov and P. W. Schultz, "Unlocking the potential of smart grid technologies with behavioral science.," *Front. Psychol.*, vol. 6, p. 410, 2015.

[14] K. Alanne and A. Saari, "Distributed energy generation and sustainable development," *Renew. Sustain. Energy Rev.*, vol. 10, no. 6, pp. 539–558, Dec. 2006.

[15] Kyocera, "Model KC200GT high efficiency multicrystal photovoltaic module." [Online]. Available: http://www.kyocera.com.sg/products/solar/pdf/kc200gt.pdf. [Accessed: 25-Sep-2017].

[16] J. A. Gow and C. D. Manning, "Development of a photovoltaic array model for use in power-electronics simulation studies," *IEE Proc. - Electr. Power Appl.*, vol. 146, no. 2, pp. 193–200, Mar. 1999.

[17] S. Sumathi, L. Ashok Kumar, and P. Surekha, "Wind energy conversion systems," in *Solar PV and wind energy conversion systems*, 2015, pp. 247–307.

[18] E. F. Camacho, C. Bordons, M. J. Grimble, and M. A. Johnson, *Model predictive control*. London: Springer London, 2007.

[19] R. Halvgaard, N. K. Poulsen, H. Madsen, J. B. Jorgensen, F. Marra, and D. E. M. Bondy, "Electric vehicle charge planning using economic model predictive control," in *2012 IEEE International Electric Vehicle Conference*, 2012, pp. 1–6.

[20] J. Maciejowski, *Predictive control with constraints*. Harlow, England ; New York: Prentice Hall, 2002.

[21] F. Kreith and D. Y. Goswami, *Energy management and conservation handbook*, 2nd ed. London: CRC Press.

[22] G. Ramos Niembro, R. Fiscal Escalante, M. Maqueda Zamora, J. Sada Gámiz, and H. Buitrón Sánchez, "Variables que influyen en el consumo de energía eléctrica," *boletín iie*, vol. 23, pp. 11–18, 1999.

CHAPTER 4

IMPACT OF HIBRID SYSTEM WITH DEVELOPED EMS AS DISTRIBUTED GENERATION

This chapter studies the influence of connecting to the distribution network prosumer systems based on HS, executing the developed energy management system (EMS). The implemented small wind turbine-photovoltaic-fuel cell hybrid system was stochastically modeled by applying time series analysis through the root mean square algorithm with forgetting factor and by using model predictive control to integrate the system as mentioned in Chapter 3. The stochastic model provides probabilistic information of short-term forecast for wind and radiation, used for the hybrid system's output electric generation planning. This study uses historic wind speed and radiation data from Mexico City, the load curves are based on average Mexican households and mini-stores on a daily basis. A study case is presented where the HS is mass connected as DG. First, using just demand-side management EMS. Second, an EMS power generation supply according to price and nodal power factor behavior; and finally a case with hybrid systems with a mix of the first and second case EMS, as to simulate individual requirements of the final user. The EMS implemented was modeled and explained in the previous chapter. The IEEE 13 node distribution test network is used as benchmark. Results show that implementation of forecast and model predictive control improve the efficiency of the hybrid systems. Furthermore, the generated active power does not reflect the intermittence of the wind speed and/or radiation. Consequently, the output power is stabilized into the tolerance range required by the grid code with the proposed method.

Various solutions have been proposed to minimize the effects of DG on distribution networks, but most of them, evaluate their study from an isolated networks point of view using external devices, or studied for a single-line microgrid [1], [2].

In this chapter, also is demonstrated that the effects of DG on frequency and power factor, at the point of common coupling (PCC), can be reduced or be overcome with an energy management system (EMS) implementation making the HS a semi-dispatchable source.

A tool using a continuous power flow in the three-phase frame-of-reference has been developed to be used to demonstrate the impacts of the prosumer system in the distribution networks. Power flow analysis uses the Newton-Raphson method. Primary equipment of distributions grids as cables, transformer and transmission lines are modeled for their basis three-phase operation, including couplings [3].

4.1   Multiphase power flow

The power flow or load flow analysis gives information about steady-state operations conditions of the power system. A power flow analysis focuses on aspects of AC power parameters, such as voltages magnitudes and angles, and active and reactive power flows. A power flow solution

predicts what the electrical state of the network will be when it is subjected to a specified loading condition.

The starting point for any power flow study is the set of generation and load data with the electrical network being described by the nodal admittance matrix (Y_{nodal}). Usually, the generation and load data is given in terms of the scheduled active and reactive power generation at the generator nodes and the predicted active and reactive power demand at the load nodes, rather than in terms of current injections. This means that the relationship between the data inputs, active and reactive power nodal injections, and the state variables, nodal voltage magnitudes and angles, is non-linear [4].

The input data for all the nodes in the system (N_B) is summarized in Table 4.1. For the generation nodes (N_G), referred to as voltage-controlled or PV-nodes, the required inputs are the net active power injection, scheduled generation minus predicted local demand and the magnitude of the nodal voltage, while the voltage angle (θ) is the unknown state variable. The unknown net reactive power injection will be determined once all the system state variables are calculated. For the load nodes, also referred to as PQ-nodes, the inputs are in the form of the specified active and reactive power demand, with the unknown state variables being the nodal voltage magnitude and angle. Usually, one of the generator nodes is selected as the slack node. At this node, the voltage angle and magnitude are specified and the unknown values of the active and reactive power injection determined once the state variables at all the other nodes are calculated. Any power system imbalance will then appear as the required generation from the slack generator [4].

Table 4.1. Node types in the power-flow problem [4]

Node type	Number of nodes	Quantities specified	Unknown voltage variables	Unknown power variables
Slack	usually 1	$\theta = 0, V$	-	P, Q
PV (source)	N_G	P, V	θ	Q
PQ (load)	$N_B - N_G - 1$	$\theta = 0, V$	θ, V	-
Total	N_B	$2N_B$	$2N_B - N_G - 2$	$N_G + 2$

4.1.1 Formulation of network equation

The basic formulation of power flow analysis in steady-state operation of a power system, is based on the equations stipulating that at a given node the generation, load, and powers exchanged through the transmission elements connecting to the node must add up to zero.

The power flow analysis implemented, was based on the single-phase power flow analysis made in [5], which considers the circuits from Fig. 4.1.
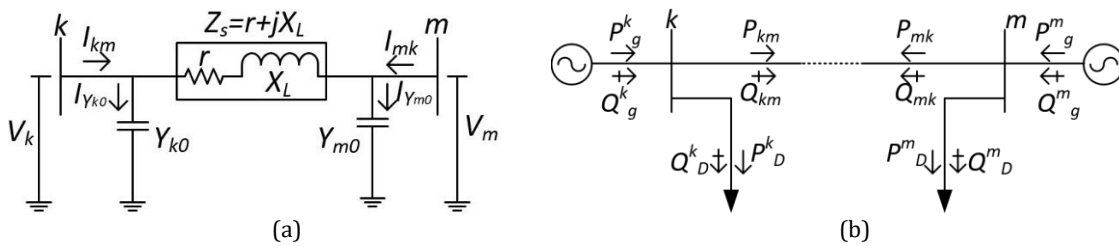
Fig. 4.1. Single-phase line (a) circuit elements (b) active and reactive power flows.

Considering the case of three conductors of a single, untransposed, three-phase line as in Fig. 4.2.
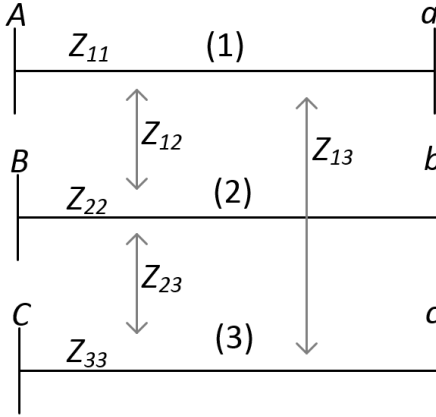
Fig. 4.2. Three parallel coupled lines

The impedance, Z_{PR} matrix representing Fig. 4.2, is assumed known and can be expressed as

$$Z_{PR} = \begin{matrix} & (1) & (2) & (3) \\ (1) \\ (2) \\ (3) \end{matrix} \begin{bmatrix} Z_{11} & Z_{12} & Z_{13} \\ Z_{12} & Z_{22} & Z_{23} \\ Z_{13} & Z_{23} & Z_{33} \end{bmatrix} \tag{4.1}$$

and its inverse, the admittance, Y_{PR} as

$$Y_{PR} = \begin{matrix} & (1) & (2) & (3) \\ (1) \\ (2) \\ (3) \end{matrix} \begin{bmatrix} Y_{11} & Y_{12} & Y_{13} \\ Y_{12} & Y_{22} & Y_{23} \\ Y_{13} & Y_{23} & Y_{33} \end{bmatrix}. \tag{4.2}$$

The nodal admittance matrix of a network may be expressed by the matrix multiplication [6]

$$Y_{bus} = N^T Y_{PR} N \tag{4.3}$$

where N is the branch-nodes incidence matrix. Corresponding to the 6-nodes, 3-branch system of Fig. 4.2, an expression for the bus admittance matrix can be written regarding (4.3) as

$$Y_{bus} = \begin{bmatrix} 1 & 0 & 0 \\ -1 & 0 & 0 \\ 0 & 1 & 0 \\ 0 & -1 & 0 \\ 0 & 0 & 1 \\ 0 & 0 & -1 \end{bmatrix} \begin{bmatrix} Y_{11} & Y_{12} & Y_{13} \\ Y_{12} & Y_{22} & Y_{23} \\ Y_{13} & Y_{23} & Y_{33} \end{bmatrix} \begin{bmatrix} 1 & -1 & 0 & 0 & 0 & 0 \\ 0 & 0 & 1 & -1 & 0 & 0 \\ 0 & 0 & 0 & 0 & 1 & -1 \end{bmatrix}. \tag{4.4}$$

Expanding (4.4) is

$$Y_{PR} = \begin{array}{c} \\ A \\ a \\ B \\ b \\ C \\ c \end{array} \begin{array}{c} \begin{array}{cccccc} A & a & B & b & C & c \end{array} \\ \left[\begin{array}{cccccc} Y_{11} & -Y_{11} & Y_{12} & -Y_{12} & Y_{13} & -Y_{13} \\ -Y_{11} & Y_{11} & -Y_{12} & Y_{12} & -Y_{13} & Y_{13} \\ Y_{12} & -Y_{12} & Y_{22} & -Y_{22} & Y_{23} & -Y_{23} \\ -Y_{12} & Y_{12} & -Y_{22} & Y_{22} & -Y_{23} & Y_{23} \\ Y_{13} & -Y_{13} & Y_{23} & -Y_{23} & Y_{33} & -Y_{33} \\ -Y_{13} & Y_{13} & -Y_{23} & Y_{23} & -Y_{33} & Y_{33} \end{array} \right]. \end{array} \qquad (4.5)$$

From the nodal admittance of (4.5), a network can be synthesized as shown in Fig. 4.3.
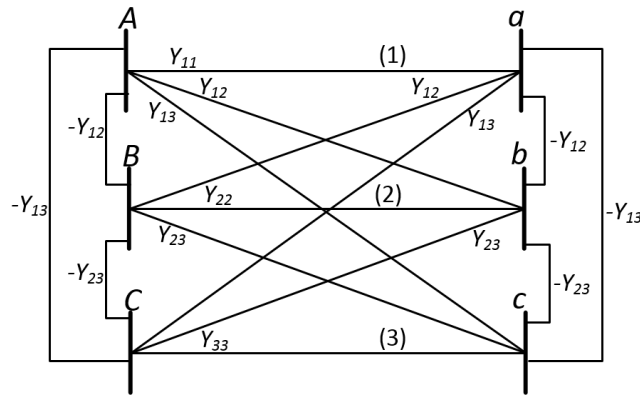
Fig. 4.3. Equivalent bus admittance as network [6]

Using the nodes order and the arbitrary orientation of the branches shown in Fig. 4.2, the odd-numbered buses can be designated as "from" buses and the even-numbered buses as "to" buses [6].

Considering Fig. 4.3, analogously, the three-phase line from Fig. 4.4 is analyzed for a multi-phase power flow.
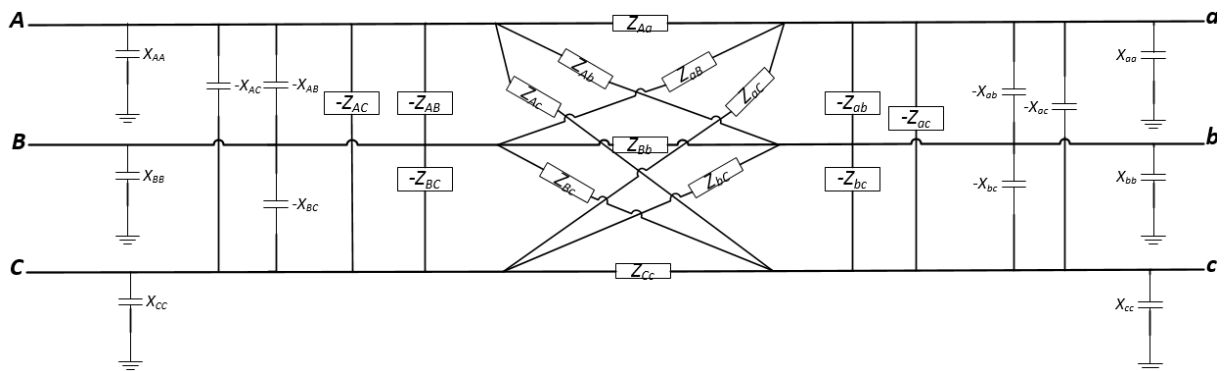
Fig. 4.4. Three-phase overhead line model with self and mutual inductances

From Fig. 4.1a and Fig. 4.4, is deduced Fig. 4.5 [6]–[8], in which is observed the required variables of a three-phase line for an easier understanding.
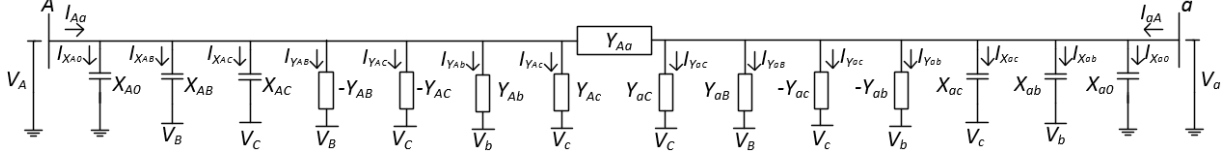
Fig. 4.5. Three-phase line with coupled effects.

For active and reactive power, the mismatch equations are

$$\Delta P_A = P_g^A - P_D^A - P_{Aa} = 0 \tag{4.6}$$

$$\Delta Q_A = Q_g^A - Q_D^A - Q_{Aa} = 0 \tag{4.7}$$

where ΔP_A and ΔQ_A represent the active and reactive power mismatch at node A respectively, P_g^A and Q_g^A are the active and reactive power injected by the generator at phase A, P_D^A and Q_D^A are the active and reactive power drawn by the load at A, and P_{Aa} and Q_{Aa} express the active and reactive power transmitted from A to a bus which are functions of nodal voltages and network impedances.

The corresponding mismatch powers are zero, for any practical purpose as seen in (4.6) and (4.7). Thus, the power balance at each bus of the network is satisfied. Considering that the nodal voltages are unknown, the calculated transmitted powers will have approximated values, and the mismatch will not be precisely zero but will have a tight tolerance, in this case of 1e−12.

To compute P_{Aa} and Q_{Aa} are required the relationship between injected currents and voltages, which are accomplished by Kirchhoff's current law (KCL) of the circuit from Fig. 4.1a, resulting

$$I_{Aa} = I_{X_{A0}} + I_{X_{AB}} + I_{X_{AC}} + I_{Y_{AB}} + I_{Y_{AC}} + I_{Y_{Ab}} + I_{Y_{Ac}} + I_{Aa}^{Y_{Aa}}$$

$$I_{Aa} = V_A X_{A0} + (V_A - V_B)X_{AB} + (V_A - V_C)X_{AC} + (V_A - V_B)(-Y_{AB}) + (V_A - V_C)(-Y_{AC}) + \tag{4.8}$$

$$(V_A - V_b)Y_{Ab} + (V_A - V_c)Y_{Ac} + (V_A - V_a)Y_{Aa}$$

regrouping the elements and rewriting (4.8) will be

$$I_{Aa} = V_A(X_{A0} + X_{AB} + X_{AC} - Y_{AB} - Y_{AC} + Y_{Ab} + Y_{Ac} + Y_{Aa}) + V_B(Y_{AB} - X_{AB}) +$$

$$V_C(Y_{AC} - X_{AC}) + V_a(-Y_{Aa}) + V_b(-Y_{Ab}) + V_c(-Y_{Ac}). \tag{4.9}$$

Equation (4.9) can be rewritten adding the admittance in brackets and considering its real (G_{XX}) and complex (B_{XX}) part, resulting in

$$I_{Aa} = V_A(G_{AA} + jB_{AA}) + V_B(G_{AB} + jB_{AB}) + V_C(G_{AC} + jB_{AC}) + V_a(G_{Aa} + jB_{Aa}) +$$

$$V_b(G_{Ab} + jB_{Ab}) + V_c(G_{Ac} + jB_{Ac}). \tag{4.10}$$

60

From (4.10), voltages can be expressed as

$$V_M = V_M e^{j\theta_M} = V_M(\cos\theta_M + j\sin\theta_M) \tag{4.11}$$

being M the voltages subscripts from (4.8).

The complex power injected at phase A consists of an active and a reactive component, which can be expressed as a function of the nodal voltage and the injected current as follows

$$
\begin{aligned}
S_{Aa} &= P_{Aa} + jQ_{Aa} = V_A I_{Aa}^* \\
&= V_A[V_A(G_{AA} + jB_{AA}) + V_B(G_{AB} + jB_{AB}) + V_C(G_{AC} + jB_{AC}) \\
&\quad + V_a(G_{Aa} + jB_{Aa}) + V_b(G_{Ab} + jB_{Ab}) + V_c(G_{Ac} + jB_{Ac})]^*
\end{aligned} \tag{4.12}
$$

where I_{Aa}^* is the complex conjugate of the current injected. Substituting (4.11) into (4.12); (4.12) can be rewritten as

$$
\begin{aligned}
S_{Aa} &= V_A e^{j\theta_A}[V_A e^{-j\theta_A}\,(G_{AA} - jB_{AA}) + V_B e^{-j\theta_B}(G_{AB} - jB_{AB}) + V_C e^{-j\theta_C}(G_{AC} - jB_{AC}) \\
&\quad + V_a e^{-j\theta_a}(G_{Aa} - jB_{Aa}) + V_b e^{-j\theta_b}(G_{Ab} - jB_{Ab}) + V_c e^{-j\theta_c}(G_{Ac} - jB_{Ac})] \\[2mm]
&= V_A^2\,(G_{AA} - jB_{AA}) + V_A V_B e^{(j\theta_A - j\theta_B)}(G_{AB} - jB_{AB}) + V_A V_C e^{(j\theta_A - j\theta_C)}(G_{AC} - jB_{AC}) \\
&\quad + V_A V_a e^{(j\theta_A - j\theta_a)}(G_{Aa} - jB_{Aa}) + V_A V_b e^{(j\theta_A - j\theta_b)}(G_{Ab} - jB_{Ab}) \\
&\quad + V_A V_c e^{(j\theta_A - j\theta_c)}(G_{Ac} - jB_{Ac}).
\end{aligned} \tag{4.13}
$$

The expressions P_{Aa} and Q_{Aa} can be determined from (4.13), by substituting the exponential in terms of *sin* and *cos* considering (4.11), and separating the real and complex part resulting in

$$
\begin{aligned}
P_{Aa} = \ &V_A^2 G_{AA} + V_A V_B[G_{AB}\cos(\theta_A - \theta_B) + B_{AB}\sin(\theta_A - \theta_B)] + \\
&V_A V_C[G_{AC}\cos(\theta_A - \theta_C) + B_{AC}\sin(\theta_A - \theta_C)] + \\
&V_A V_a[G_{Aa}\cos(\theta_A - \theta_a) + B_{Aa}\sin(\theta_A - \theta_a)] + \\
&V_A V_b[G_{Ab}\cos(\theta_A - \theta_b) + B_{Ab}\sin(\theta_A - \theta_b)] + \\
&V_A V_c[G_{Ac}\cos(\theta_A - \theta_c) + B_{Ac}\sin(\theta_A - \theta_c)]
\end{aligned} \tag{4.14}
$$

$$
\begin{aligned}
Q_{Aa} = \ &-V_A^2 B_{AA} + V_A V_B[G_{AB}\sin(\theta_A - \theta_B) - B_{AB}\cos(\theta_A - \theta_B)] + \\
&V_A V_C[G_{AC}\sin(\theta_A - \theta_C) - B_{AC}\cos(\theta_A - \theta_C)] + \\
&V_A V_a[G_{Aa}\sin(\theta_A - \theta_a) - B_{Aa}\cos(\theta_A - \theta_a)] + \\
&V_A V_b[G_{Ab}\sin(\theta_A - \theta_b) - B_{Ab}\cos(\theta_A - \theta_b)] + \\
&V_A V_c[G_{Ac}\sin(\theta_A - \theta_c) - B_{Ac}\cos(\theta_A - \theta_c)].
\end{aligned} \tag{4.15}
$$

Equations (4.14) and (4.15) are substituted in (4.6) and (4.7) respectively.

Similar equations are obtained for the different buses and phases by changing the subscripts of the resulting (4.6) and (4.7). The mismatch vector for the three-phase overhead line comprises active and reactive nodal power as follows $[\Delta P_A, \Delta P_B, \Delta P_C, \Delta P_a, \Delta P_b, \Delta P_c, \Delta Q_A, \Delta Q_B, \Delta Q_C, \Delta Q_a, \Delta Q_b, \Delta Q_c]$ and the state vector of variables $[\theta_A, \theta_B, \theta_C, \theta_a, \theta_b, \theta_c, V_A, V_B, V_C, V_a, V_b, V_c]$.

The Same technique was applied to the basic distribution network elements, overhead line, concentric neutral cable, tape-shielded cable, and transformers; and the models were integrated into the power flow analysis algorithm. Those models are presented in Appendix C.

From all the different buses and phase equations, the system will have a problem with twelve unknown variables and the same number of mismatch equations for Fig. 4.5, modeled as presented in Appendix C.

To apply the Newton-Raphson (N-R) method to solve the system equations representing the three-phase distribution network the power flow formulation is expressed as

$$
\begin{bmatrix} \Delta P_A \\ \cdot \\ \cdot \\ \cdot \\ \Delta P_c \\ -- \\ \Delta Q_A \\ \cdot \\ \cdot \\ \cdot \\ \Delta Q_c \end{bmatrix} = \begin{bmatrix} \frac{\partial \Delta P_A}{\partial \theta_A} & \cdot & \cdot & \cdot & \frac{\partial \Delta P_A}{\partial \theta_c} & | & \frac{\partial \Delta P_A}{\partial V_A}V_A & \cdot & \cdot & \cdot & \frac{\partial \Delta P_A}{\partial V_c}V_c \\ \cdot & & & & \cdot & | & \cdot & & & & \cdot \\ \cdot & & & & \cdot & | & \cdot & & & & \cdot \\ \cdot & & & & \cdot & | & \cdot & & & & \cdot \\ \frac{\partial \Delta P_5}{\partial \theta_A} & \cdot & \cdot & \cdot & \frac{\partial \Delta P_c}{\partial \theta_c} & | & \frac{\partial \Delta P_c}{\partial V_A}V_A & \cdot & \cdot & \cdot & \frac{\partial \Delta P_c}{\partial V_c}V_c \\ -- & -- & -- & -- & -- & | & -- & -- & -- & -- & -- \\ \frac{\partial \Delta Q_A}{\partial \theta_A} & \cdot & \cdot & \cdot & \frac{\partial \Delta Q_A}{\partial \theta_c} & | & \frac{\partial \Delta Q_A}{\partial V_A}V_A & \cdot & \cdot & \cdot & \frac{\partial \Delta Q_A}{\partial V_c}V_c \\ \cdot & & & & \cdot & | & \cdot & & & & \cdot \\ \cdot & & & & \cdot & | & \cdot & & & & \cdot \\ \cdot & & & & \cdot & | & \cdot & & & & \cdot \\ \frac{\partial \Delta Q_c}{\partial \theta_A} & \cdot & \cdot & \cdot & \frac{\partial \Delta Q_c}{\partial \theta_c} & | & \frac{\partial \Delta Q_c}{\partial V_A}V_A & \cdot & \cdot & \cdot & \frac{\partial \Delta Q_c}{\partial V_c}V_c \end{bmatrix} \begin{bmatrix} \Delta\theta_A \\ \cdot \\ \cdot \\ \cdot \\ \Delta\theta_c \\ -- \\ \frac{\Delta V_A}{V_A} \\ \cdot \\ \cdot \\ \cdot \\ \frac{\Delta V_c}{V_c} \end{bmatrix} \quad (4.16)
$$

which when solving, a check for convergence is needed applying $\|f(x_0 + \Delta x_n)\| \le \varepsilon$, as explained in Appendix D, where ε is the tolerance with a value of $1e^{-12}$ in this case. The algorithm solving the power flow alongside the modeled network elements were coded in MATLAB ®, resulting in a program for multiphase power flow analysis.

4.1.2 Validation of multiphase power flow algorithm

With the purpose to corroborate the performance of the multiphase power flow algorithm programmed in MATLAB ®, the distribution networks IEEE 13 nodes and IEEE 34 nodes were implemented (Appendix E and F). Initially, the parameters of the networks were introduced in the multiphase power flow program coded in MATLAB ® and the results obtained were validated with a commercial software NEPLAN ® version 5.5.4, showing minimum differences. Confronting the results obtained from the multiphase power flow MATLAB ® program and NEPLAN ®, it can be

observed that are very similar, with minimum differences as shown in Fig. E.2, Fig. E.3 and Fig. F.2, Fig. F.3 for the respective networks in Appendix E and Appendix F.

Even though NEPLAN ® version 5.5.4 performs power flow analysis for multiphase networks; it lacks the models for hybrid systems even the different generators based on renewable energies, used for NEPLAN ® are generic models.

4.2   Continuous power flow analysis with DG

Up to this point, the multiphase power flow program works in steady-state. To analyze a network performance for several days in a row is required to update the steady-state power flow program to a continuous power flow program, capable of analyzing distribution networks with DG supply in a required time frame.

The power flow software developed and validated for steady-state analysis has been updated to perform continuous power flow analysis. Using the updated software, the prosumer system is programmed to follow an actual load curve, and validate the capabilities of the EMS controlling the prosumer system.

The new software runs in the time frame-of-reference, and the EMS is supported by the forecasting technique developed in Section 2.2.1 and published by the author in [9], this method provides the behavior of the network in the time frame required and the one hour-ahead. Furthermore, provides the behavior of the grid with the impact of the DG implementing the HS with the EMS using renewable energies developed during this research.

The algorithm used to perform the continuous power flows analysis with prosumer coupling can be observed in Fig. 4.6. Initially, the distribution lines, transformers, configuration and complete information of the distribution network is loaded into the program. The selected prosumer EMS will run for the required time and will provide the results for that period plus the next hour behavior; it is considered that the HS's are connected to the grid through a DC/AC converter as shown in Figs. 2.1 and 3.1.

When all required data are loaded, the power flow program will perform a power flow analysis of the distribution network behavior instant per instant, updating the corresponding power and demand data at each time. This process can keep running while the data source continues to manage data. Using the forecast method, the program simulates one hour-ahead behavior of the grid, working as a tool to prevent the frequency, voltage levels and voltage angles of the grid from being affected.

It is worth mention that for each power flow analysis at time t, the program will make the conventional iterations process to analyze the network with the one hour-ahead forecasted generation supply given by the EMS's and the load data supplied.

4.2.1 Load curve

In Mexico City, residential users spent the same amount of energy throughout the year [10], the only remarkable differences are due the summer hour change and month to month because of the artificial illumination at mornings and evenings. The load curves were obtained from official and public researches. The load curves in the residential sector were deduced from the data in [11],

[12]. [11] presents a statistical report focused on the 2013 year load curves of the residential and commercial sectors; the document shows the average monthly electric consumption of Mexican households and low tension commercial users. [12] analyses the residential consumption taking into account weather influence on the central Mexico region; this region include Mexico City, the states of Morelos, Guerrero, Estado de Mexico, and Puebla.
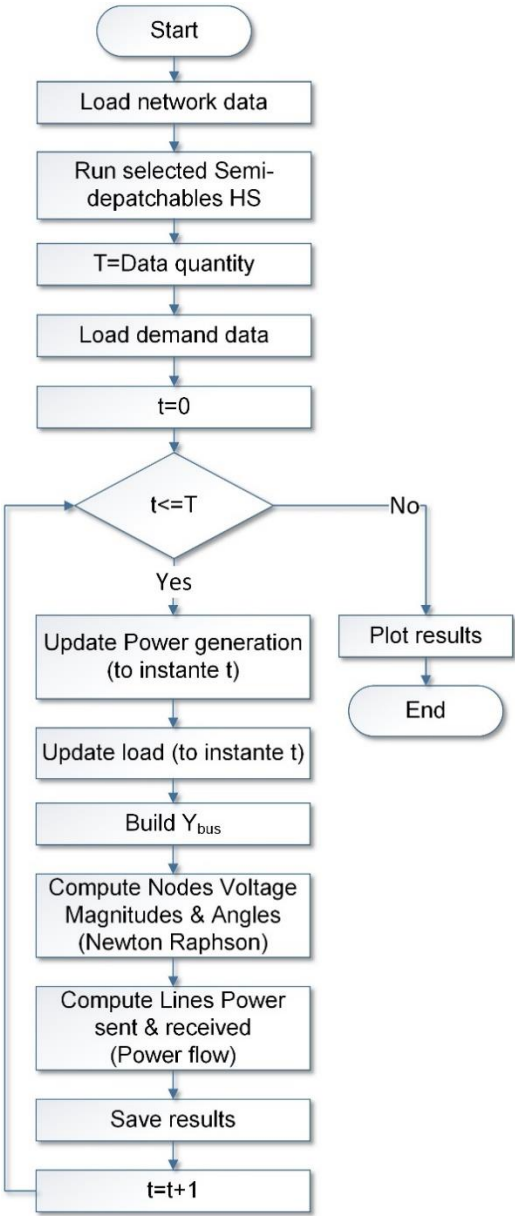
Fig. 4.6. Flowchart of continuous power flow with load curves and embedded semi-dispatchable HS as DG.

The focus of the load curves implemented in this research were households and mini-stores in Mexico City at working days. The mini-store load curve was obtained from [13]. Fig. 4.7 shows the daily curves for different households in January and July without weather influence; additionally, it is presented the load curve of a mini-store.
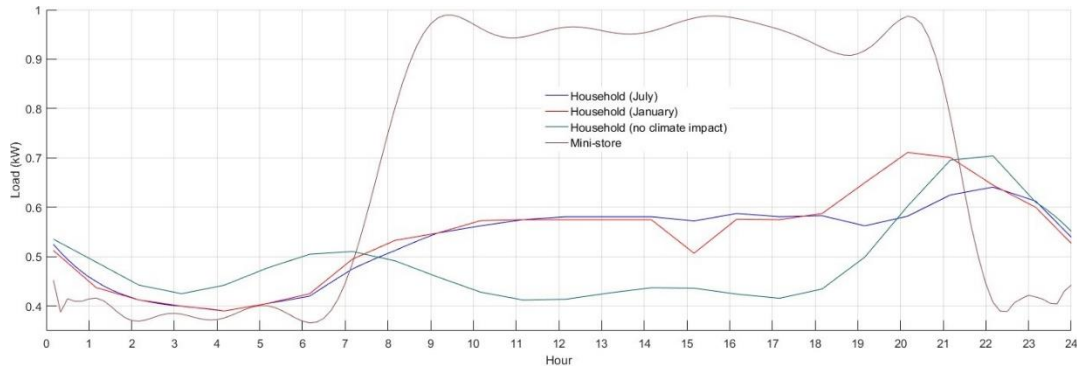
Fig. 4.7. Load curves for different households and mini-store.

The load curves were added to make a set of twenty houses and one mini-store as seen in Fig. 4.8. The last load curve is applied in the test distribution network of the test cases.
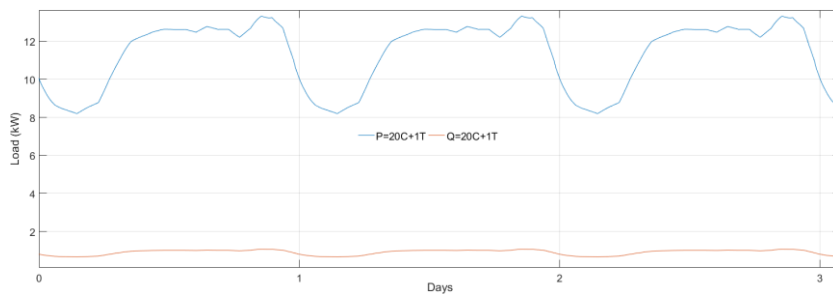
Fig. 4.8. Load curve of twenty houses plus one mini-store.

4.3 Distributed generation

DG is defined under IEEE Standard 1547 as electricity generating facilities connected to an electric power system through a point of common coupling. Also, DGs are defined as small-value generators up to 10 MVA and a subset of distributed resources (DR) [14]. DR are resources of electric power that are not directly connected to bulk power transmission systems, includes both generators and energy storage facilities.

DG is related to the use of small generating units installed at strategic points of the electric power system or locations of load centers. DG can be used in an isolated way, supplying the consumer's local demand, or integrated into the grid supplying energy to the remainder of the electric power system. DG technologies can run on renewable energy sources (RES), fossil fuels or waste heat. Equipment ranges in size from less than a kilowatt (kW) to tens of megawatts (MW). If connected to a distribution or transmission system, power can be sold to the utility or a third party.

The implications for the interconnection of the utility are: Customers within the supply zone of a utility are covered under power quality parameters like voltage and frequency. Any deviations of parameters out of tolerance limits are subject to financial damage claims by customers [14]. The most important impact of the deregulation of the electricity market is that there is no longer any single organization that has control over the location and production of the individual generator stations [15]. Despite the small size of DG technologies, these are having a strong impact in electricity markets. However, there are technical issues that deserve attention [16].

The potential adverse impacts at distribution level include [15]:

- Overload of feeders and transformers could occur due to large amounts of production during periods of low consumption.

- The risk of over-voltages increases due to production at remote parts of a distribution feeder. This could in theory already occur before the production exceeds the consumption.

- As consequence of the introduction of DG, the level of power quality disturbances may increase beyond what is acceptable for other customers.

- Incorrect operation of the protection is another potential consequence of large amounts of DG. This could be failure to operate or unwanted operation.

On the contrary, premium power market reliability and power quality can be improved by the use of DG and its integration. Reliability and power quality improvements are significant impacts of DG integration in the form of microgrid through an active distribution network. The following requirements are the main elements of power quality and reliability improvement [17]:

- Fast response: The load needs fast response of energy storage system to safeguard from momentary voltage fluctuations.

- Clean power: Storage power should be converted to clean power.

- Synchronization: Smooth control should be there in paralleling and synchronization.

- Soft transfer: Alternate power source should be capable of seamless power transfer.

- Isolation: Integrated DG, i.e. microgrid should be efficient enough in quick isolation from utility in case of any contingencies.

- Adequate storage: The quantity of storage energy should be sufficient to ride through any outage until primary or secondary power restoration.

- Supply to priority loads: Microgrid should be capable of supplying clean power to the priority loads of the system.

- Dispatch ability: Microgrid should be capable of supplying power to varying local loads.

- Efficiency: Microgrid should operate at high efficiency.

- Emission: Microgrid should drastically reduce DG emissions to minimize the environmental impacts.

4.3.1 DG interconnection to Mexican electric network

The Mexican government has established a decree [18], and regulation [19], stating the renewable energies use and financing of the energy transition. A strategy is settled as the

mechanism through which the Mexican State will promote policies, programs, actions and projects aimed to achieve higher RES use and clean technologies, promoting energy efficiency and sustainability. The national electricity system will receive the produced electricity from renewable energy surplus derived from self-sufficient or cogeneration electric projects [18], following the established public electric energy service law [20]. The electric industry law states, in article 23 and 24, that power plants that allocate part of their production for isolated supply purpose can be interconnected to the national transmission network or the general distribution grid [21].

Considering the technical issues concerning the connection to the network and taking into account the grid code; first, it is relevant to keep in mind that the power factor (PF) is an indicator displaying the correct energy usage. It can take values between 0 (very bad) and 1 (ideal value). A value of 1 indicates that all energy consumed has been converted into work. The CFE issues a penalty for power factors below 90% [22].

At low voltage network, the inverter must operate with power factor higher than 0.90 inductive or capacitive, for output powers higher than 10% of its nominal power. The system should operate in synchrony with the network and not cause deviations in its frequency. The system frequency regulation control must be in the range of 59.2 - 60.8 Hz [23]. The distributed energy resource (DER) will be connected parallel to the national network without causing voltage fluctuations greater than +/- 5% of the network voltage levels at the connection point and ought to comply with the disturbance requirements established by CFE [24].

The generation system requires over-voltage, under-voltage, frequency, anti-islanding, and synchronism protections. The connection diagram is shown in Fig. 4.9, where the battery bank is optional, as it is the DC/AC inverter depending on the generation device [24].
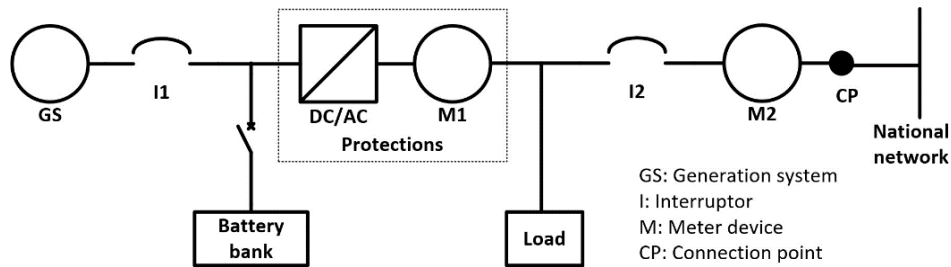
Fig. 4.9. DER connection diagram to low voltage network [24].

The meter M1 indicated in Fig. 4.9, has the function of recording the total generation in kWh from the DER and must be supplied by the generator owner or integrated as part of the DER. The meter M2 is the billing meter. Both meters are described in [25].

4.3.2 DG interconnection in the world

Steady-state operational requirements focus on frequency, active power and reactive power settings, and operational ranges. In 50 Hz electrical power systems, the frequency range during normal power system operation is a narrow band between 49.95 and 50.05 Hz. A frequency value outside this range normally calls for corrective control measures. As opposed to conventional plants, renewable-based generation plants connected to the grid through VSCs are capable of operating in a much broader frequency range. As a result, continuous operation in the frequency range between 49 and 50.5 Hz is considered as a basic requirement as long as the voltage does not

exceed 1.1 p.u., in which case disconnection is permissible after a 30 min delay. While there is no requirement to remain connected outside the range of 46.5 and 52.5 Hz, disconnection inside this range (and outside the 49 – 50.5 Hz) is possible only after a certain delay, depending on the value of the frequency [26].

Regarding active power output, generating units are required to be capable of operating up to the rated output power in the frequency range from 47.5 to 50.2 Hz. In addition, the units must be capable of reducing active power output in steps from any operating point to a target value given by the network operator. The required reduction in each step can amount to maximum 10% of the contractually agreed active power at the connection point with no timeframe for reaching the target value, but the interval should be less than 1 min. For renewable-based power generation units, the frequency threshold for active participation in frequency control is 50.2 Hz. When the frequency exceeds this value, continuous output power reduction is a requirement; the reduction rate is 40% of the generator's momentary output per hertz, and be as fast as possible (within a 10 s maximum time span) [26].

Fig. 4.10 presents an example of the minimum requirements in steady-state operation regarding the reactive power supply capability. The specific requirements may vary depending on the grid. Reactive power supply capability exceeding these minimum requirements is also allowed. All generation plants must be capable of shifting from one operating point to another inside the boundary within a time span of 30 s at a maximum [27].
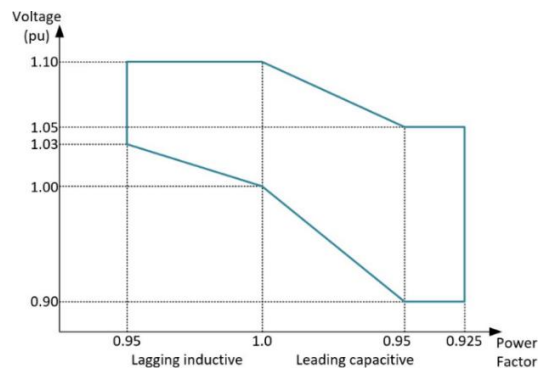
Fig. 4.10. Reactive power requirement at the point of common coupling.

4.4 Power flow analysis for hybrid system controlled by developed EMS, connected as DG

The IEEE13 test feeder is used to test the proposed algorithm. Appendix E gives the parameters used for the distribution network. A base case was simulated as benchmark to compare the effects of the DG in the simulated cases. It can be distinguished that distribution lines are not all three-phase, but there are two-phase and single-phase lines; giving an idea of the multiphase topology of a distribution network. For this base case, the original grid loads were replaced by mass households and mini-store loads keeping the original loads average, as presented in Fig. 4.11 for the three-phases. Power flow results of the benchmark grid are also shown in Appendix E, Fig. E.2 and E.3 show the solution of the network with no prosumer as DG, both for the developed software and the commercial one, in this case, NEPLAN ®.

To emphasize the effects of the DG when integrated to power systems, a load disturbance is applied in one phase as to show the independent response of each connected EMS. The load connected at node 11 has been sudden incremented by three times only in phase *c* this increment can be seen in Fig. 4.11.
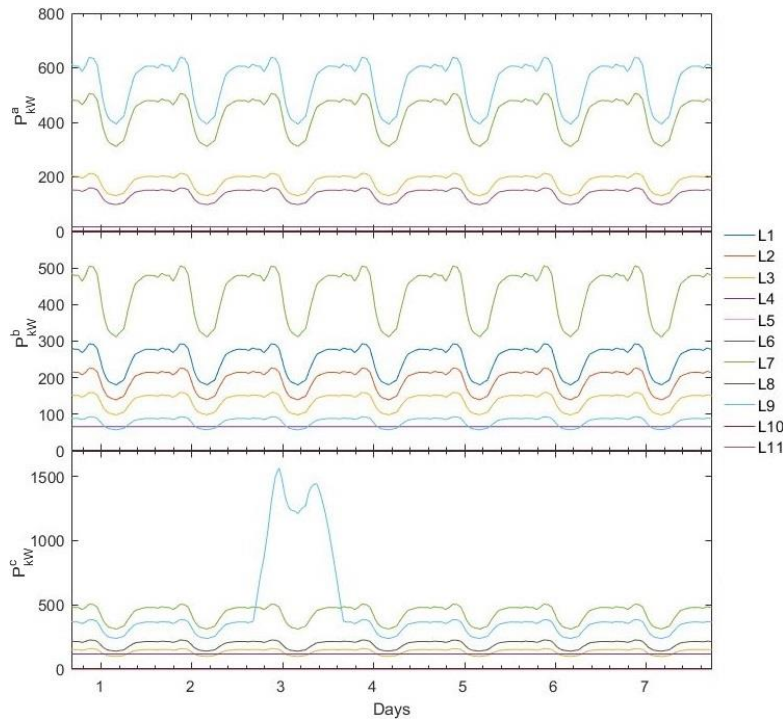
Fig. 4.11. Grid active power loads.

To assess the DG impact in the distribution network, 13 HS controlled by the proposed EMS, were added in six buses of the grid to act as prosumers. In addition to the solution of the network with no prosumer, three other cases are assessed:

- Case 1: All prosumers are controlled to improve the power factor at their connection point and respond to cost behavior.
- Case 2: All prosumers are controlled to supply energy as the load curves shown in Fig. 4.11, demand-side management mode.
- Case 3: A mix of controls are applied. The HS connected in nodes 2, 6, 12 and 11 phases *a* and *c*, follow the load curve and the ones connected in nodes 2, 8, 14 in phases *b* and *c*, and node 11 in phases *a* and *b* improve the power factor at the connection point, as shown in Fig. 4.12.

Fig. 4.12 shows grid update with the HS. The EMS algorithms developed in this research is used as the controller for the prosumers. The purpose of these cases, is to appreciate the way in which the EMS helps to follow the curve demand and/or support the power factor at the connection point. Moreover, the general characteristics of the grid, considering the implemented stochastic models can also be appreciated.

A whole week scenario is implemented in all cases to evaluate the different EMS models flexibility. Additional to the previously mentioned voltage phenomenon occurrence on the third

day, it is assumed expensive cost on the first and sixth day of the week; low electricity cost on the second, fourth and seventh days; as well as an average cost on the third and fifth day, as presented in Fig. 4.13. It is meaningful remarking the fact that the last hour of the analysis, belongs to the one hour-ahead forecasted generation.
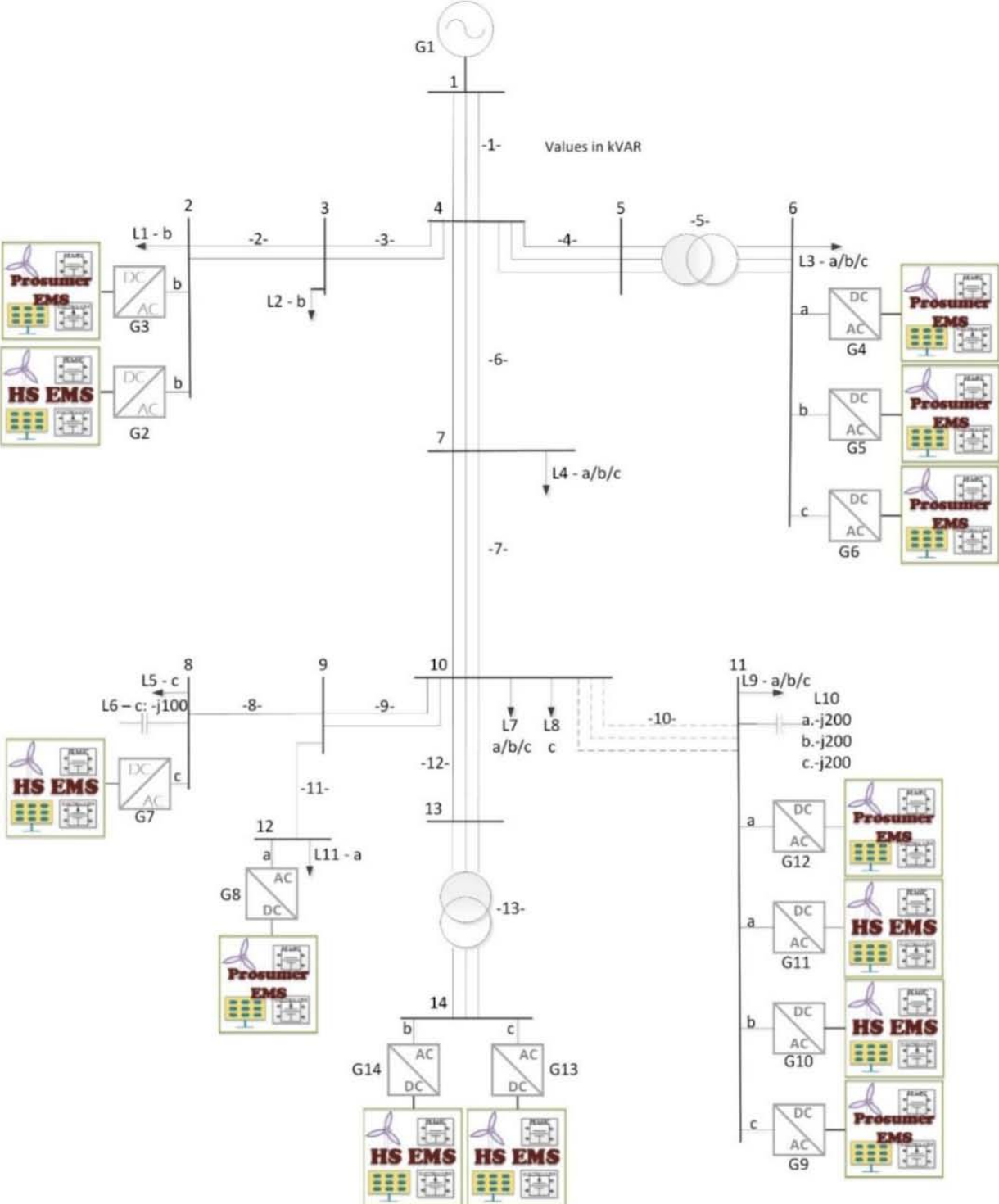
Fig. 4.12. Modified IEEE 13-nodes distribution test feeder network.
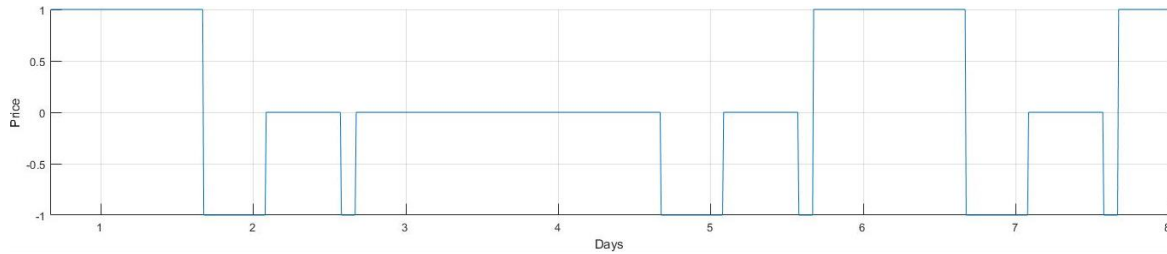
Fig. 4.13. Assumed cost curve.

4.4.1 Results obtained

Base case

Unsurprisingly, the solution given by the developed program essentially agrees with that provided by the commercial software (Appendix E). It can be observed that all nodal voltages are with accepted voltage magnitudes limits. As expected in distribution feeders, the larger power flow takes place in the line connecting the primary distribution network, node 1 and the closest substation, node 4. Fig. 4.14 shows the active power supplied to the feeder by the primary distribution network per phase. It can be observed from the plot that all three-phases are unbalanced, being phase c the one that transmits more power, almost the double 3,009.1 kW, that the phases a and b, with 1,576.2 kW, 1,374.8 kW respectively; this condition is presented because of the disturbance on the third day.
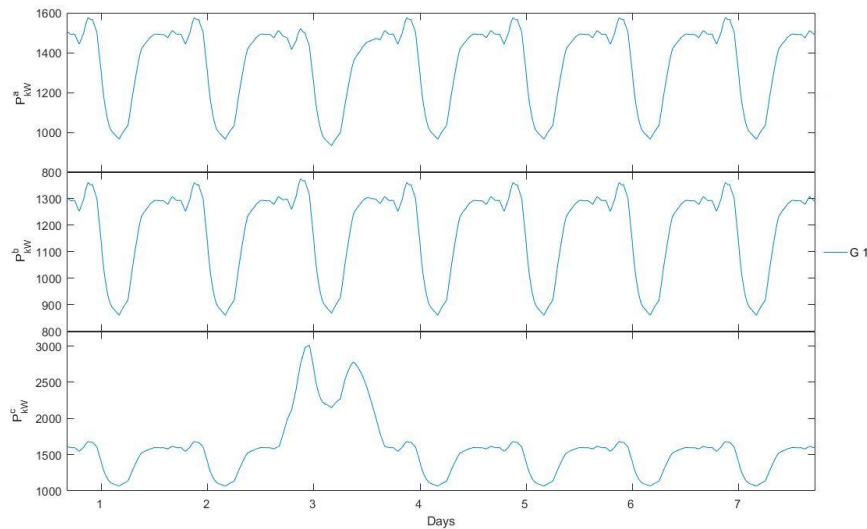
Fig. 4.14. Base case grid power generation.

Likewise, the disturbance is reflected in the behavior of active power running through overhead lines and underground cables, nodal voltages and power factor obtained from the base case, as displayed in Fig. 4.15 to Fig. 4.17. This results will be further addressed in the next section to compare them with the other test cases simulated.

71
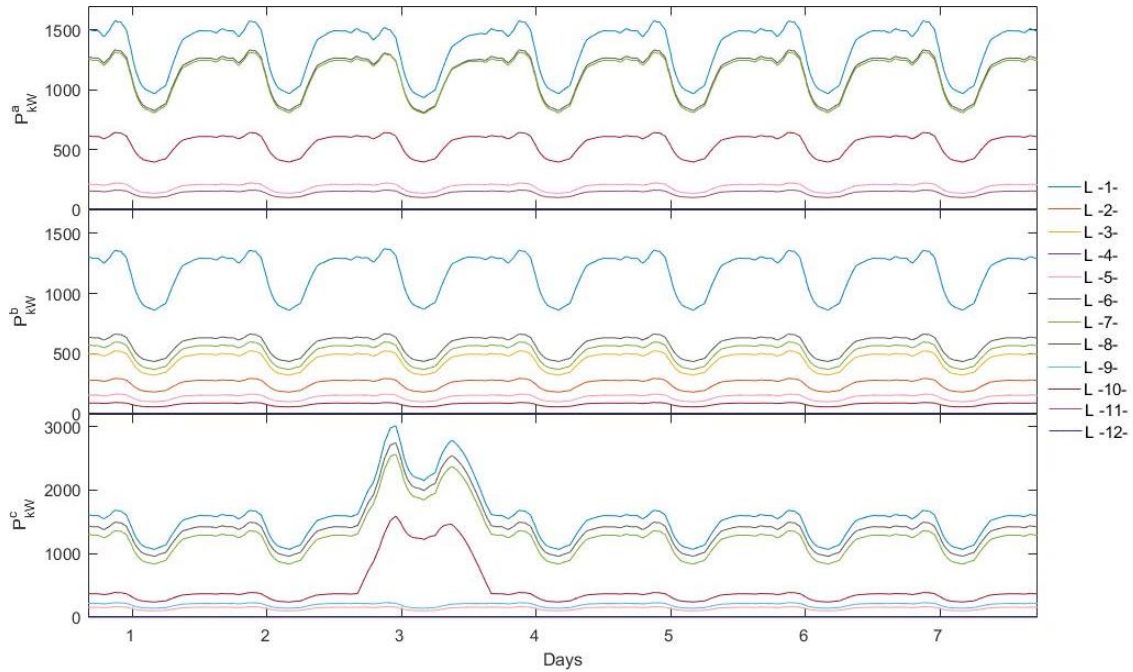
Fig. 4.15. Base case grid active power through lines.

Fig. 4.15 shows the active power through overhead lines and underground cables. Whereas, in Fig. 4.16, it is observed that nodal voltage variations are within acceptable limits, i.e. +/-10% in the PCC Mexican grid code for small generation [28], and +/-5% in the remaining nodes.
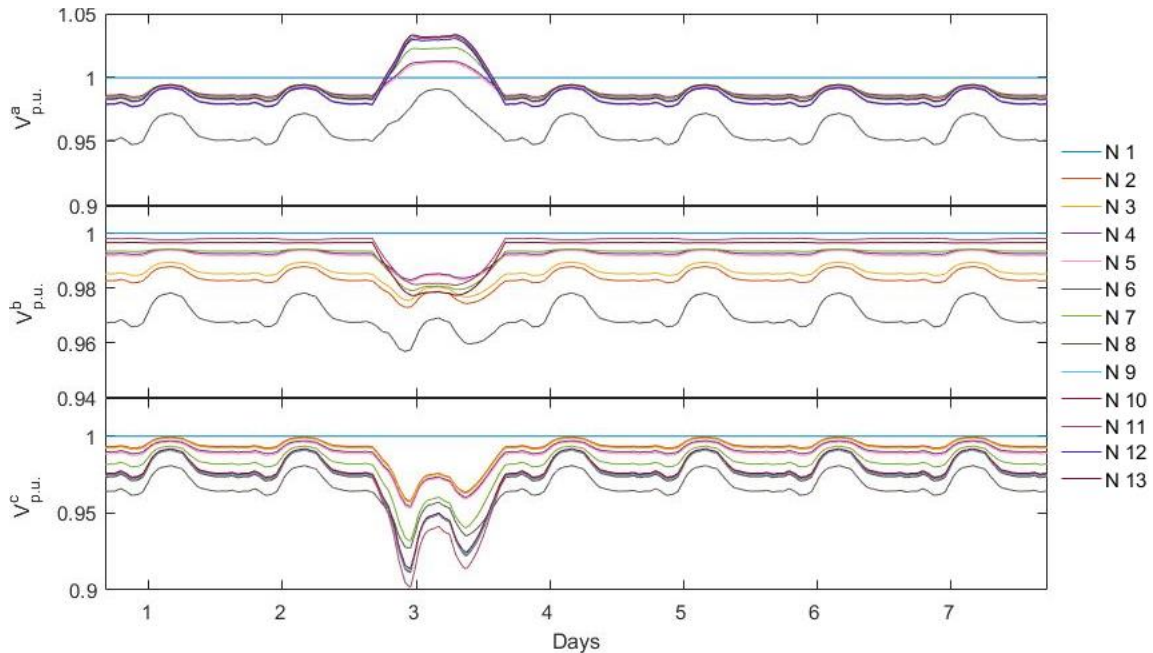
Fig. 4.16. Nodal voltage profile in the base case grid.

The power factor presents a similar behavior; they are within acceptable limits, i.e. +/-5% in the Mexican grid code; in this case, only the feeder node maintains a unit power factor. Fig. 4.17 shows

the power factor response in the base case. The presented average value per phase is 0.9980, 0.9995, and 0.9971.
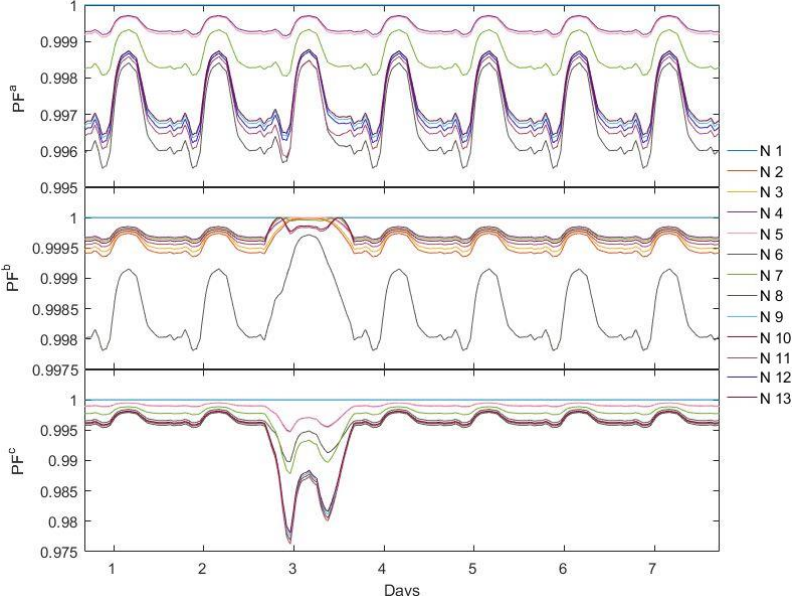
Fig. 4.17. Base case power factor response.

Hybrid systems implement EMS for power factor improvement and respond of cost behavior

In this scenario, the EMS was programmed to improve the power factor with the EMS developed in Section 3.4.1, considering (3.12) and (3.13). The PF is improved until it reaches a value between 0.995 and 1.

Fig. 4.18 shows active power injections supplied by the various embedded HS and the principal supplier at node 1. The HSs are connected per phase, considering the end users individuality. Results are introduced like the sum per block of the prosumer connected at said node. The main power supply presents a minimum injection of -394.27 kW, 112.6 kW, and 2.68 kW per phases a, b, and c respectively.
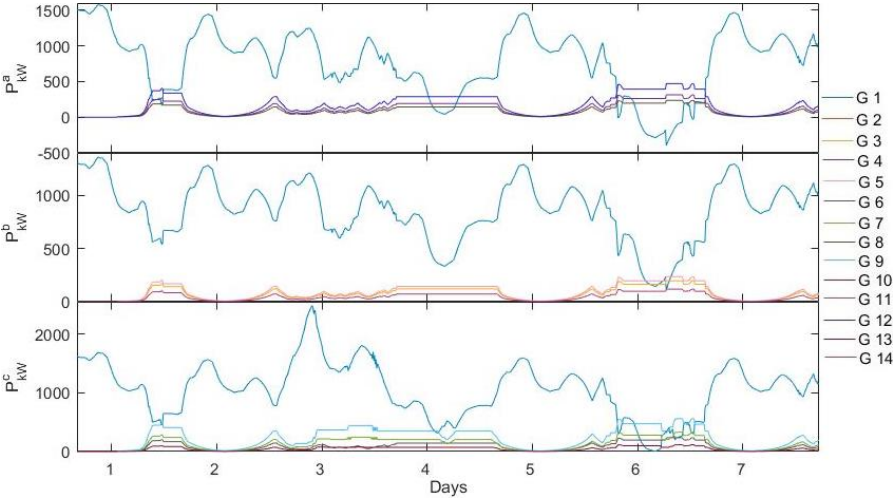
Fig. 4.18. Grid power generation.

It is noticeable in Fig. 4.18 the variability of the supplied HS generation, as consequence of the change in cost and power factor behavior.

In Fig. 4.19 It can be seen a power flow reduction through lines in comparison with the results obtained in the base case, reflected in line 1 with a reduction average per phase of 41.47%, 27%, and 32.56%. Furthermore, the active power through lines presents a change of flow direction. This behavior is because of the power generated by the HSs been greater than the load, i.e. line 10; as a result, the power losses through lines decreased considerably, as seen below in Fig. 4.39 and further discussed in Section 4.5.
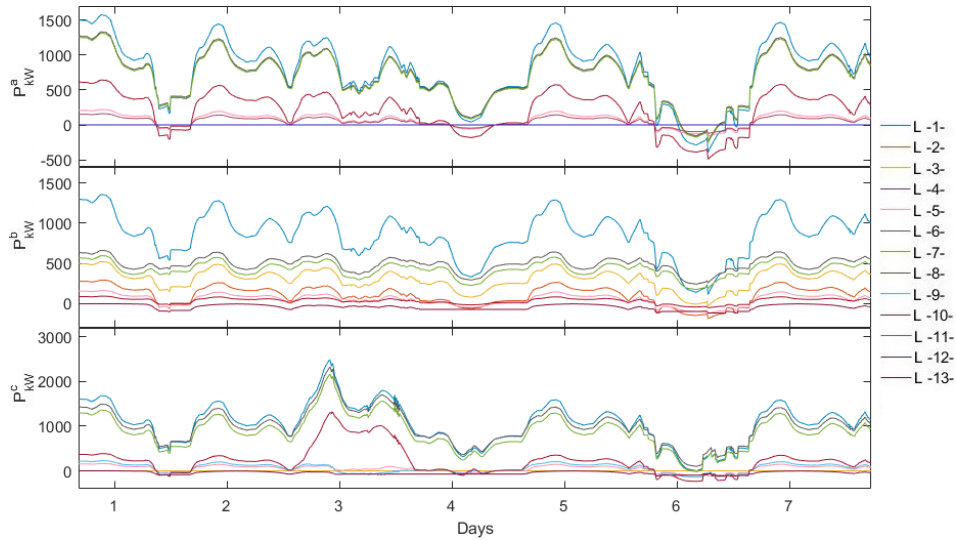
Fig. 4.19. Grid active power through lines.

The nodal voltages profile presented in Fig. 4.20 show values between of 1.0302 p.u. – 0.94 p.u. in phase *a*, 1.002 p.u. - 0.959 p.u. in phase *b*, and 1.034 p.u. – 0.919 p.u. in phase *c* considering all nodes, which are within the accepted limits. The voltage profile at base case has an average of 0.9861 while in this case of study presents an average of 0.9907 being an improvement. When there is power injection from the HSs, the nodal voltages will increase.
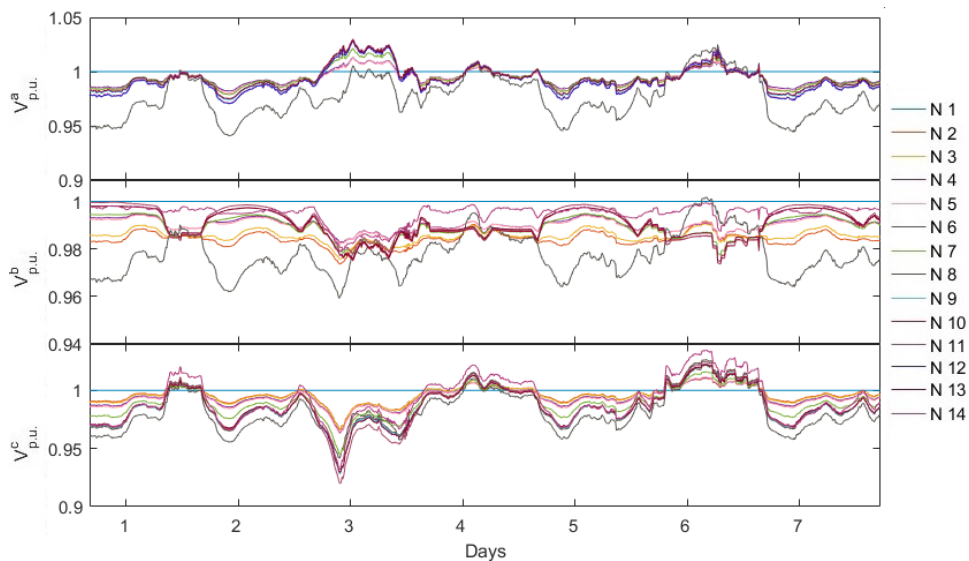
Fig. 4.20. Grid nodal voltages.

Fig. 4.21 presents the improvement of the power factor behavior, which is nearer to 1 at all times after the HS start-up period, at each node in contrast to the base case. The average values presented are 0.9992, 0.9997, and 0.9985 per phase, representing a 59.47%, 43.23%, and 49.13% improvement per phase when compared to the base case.
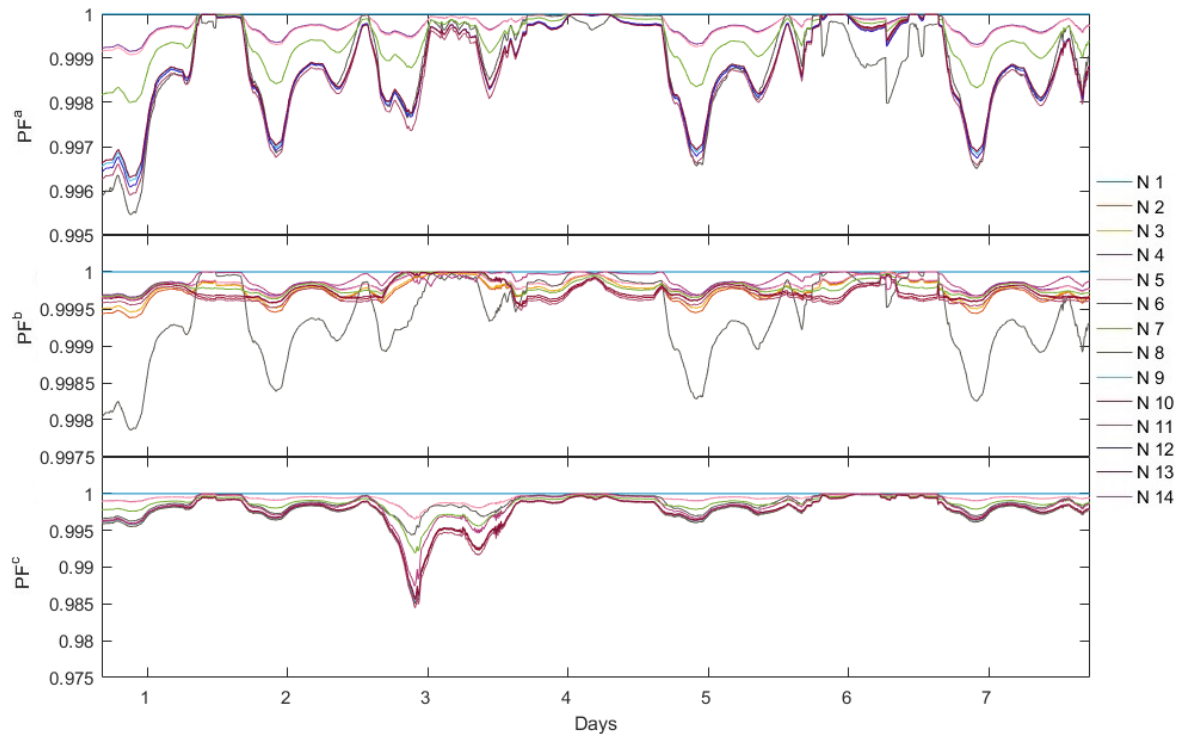
Fig. 4.21. Grid nodal power factor behavior.

The embedded HS individual performance can be seen in Fig. 4.22 where the EMS dispatch can be identified by the generation curve. Additionally, is observed how the HSs that see the power factor deviation from the accepted range of values, G7, G9, and G13, inject more power to the grid when the power factor at PCC is affected by the recreated disturbance. The increase of power injection due to cost value is observed in the sixth day, which causes a power injection to the grid through node 1, previously seen in the change of power flow direction in line 1. The power supply by the HSs is in accordance with the wind and solar radiation profiles.

The storage behavior from each HS is shown in Fig. 4.23, as in the previous figure, the legend identifies the generator number and location.

Hybrid systems implement prosumer method for demand-side management

In this scenery each EMS is programmed to follow a demand curve, results are shown in Fig. 4.24 to Fig. 4.27. Initially, Fig. 4.24 presents the grid generators behavior corresponding to the active power, as in the previous case, the grid supplier G1, shows a maximum generation similar to the base case on the first day, due to the charging storage period. In addition, the G1 minimum generation is 712.28 kW, 730.25 kW, and 868.7 kW per phases *a*, *b*, and *c*, respectively.
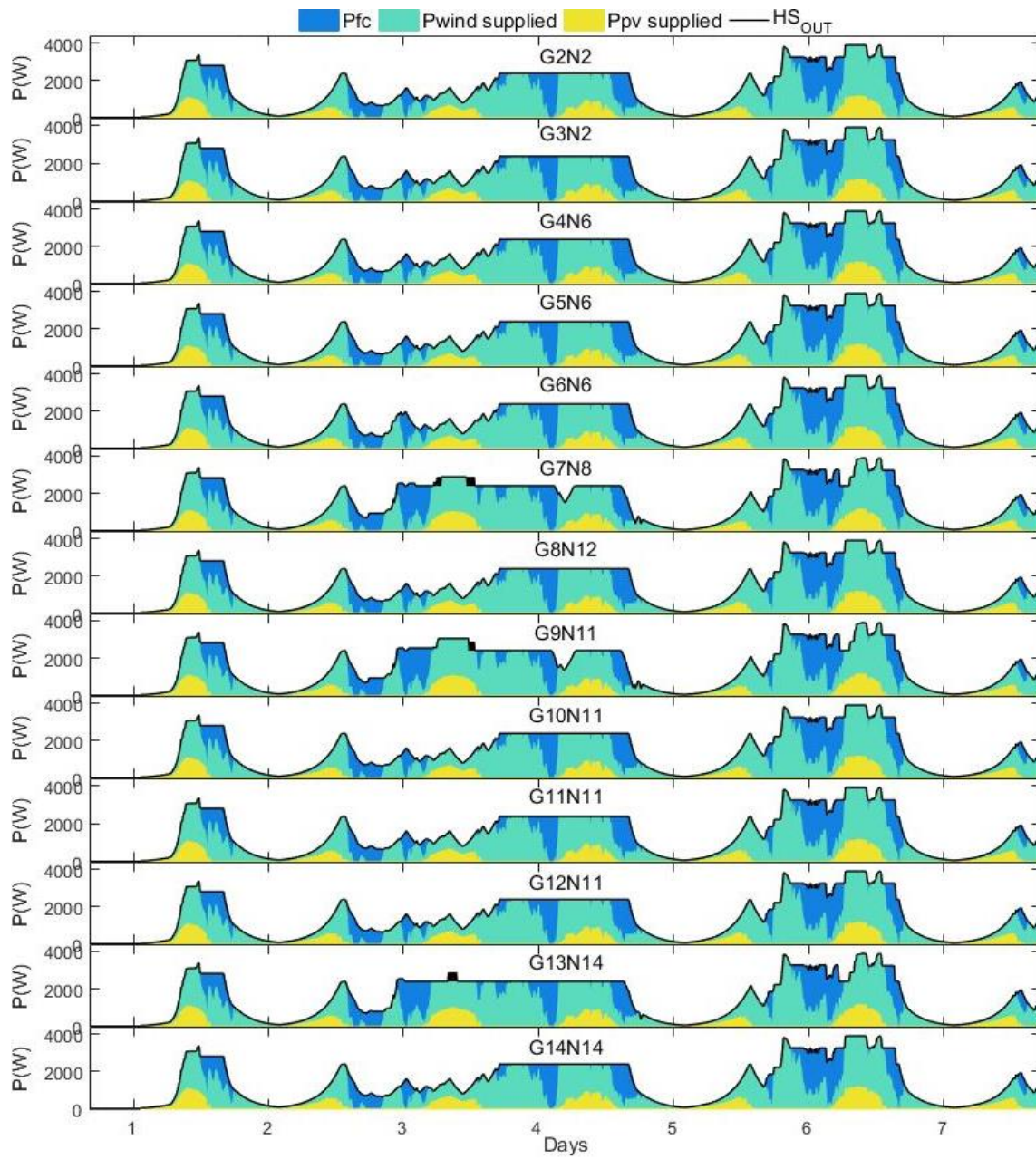
Fig. 4.22. Dispatched power from HS's.
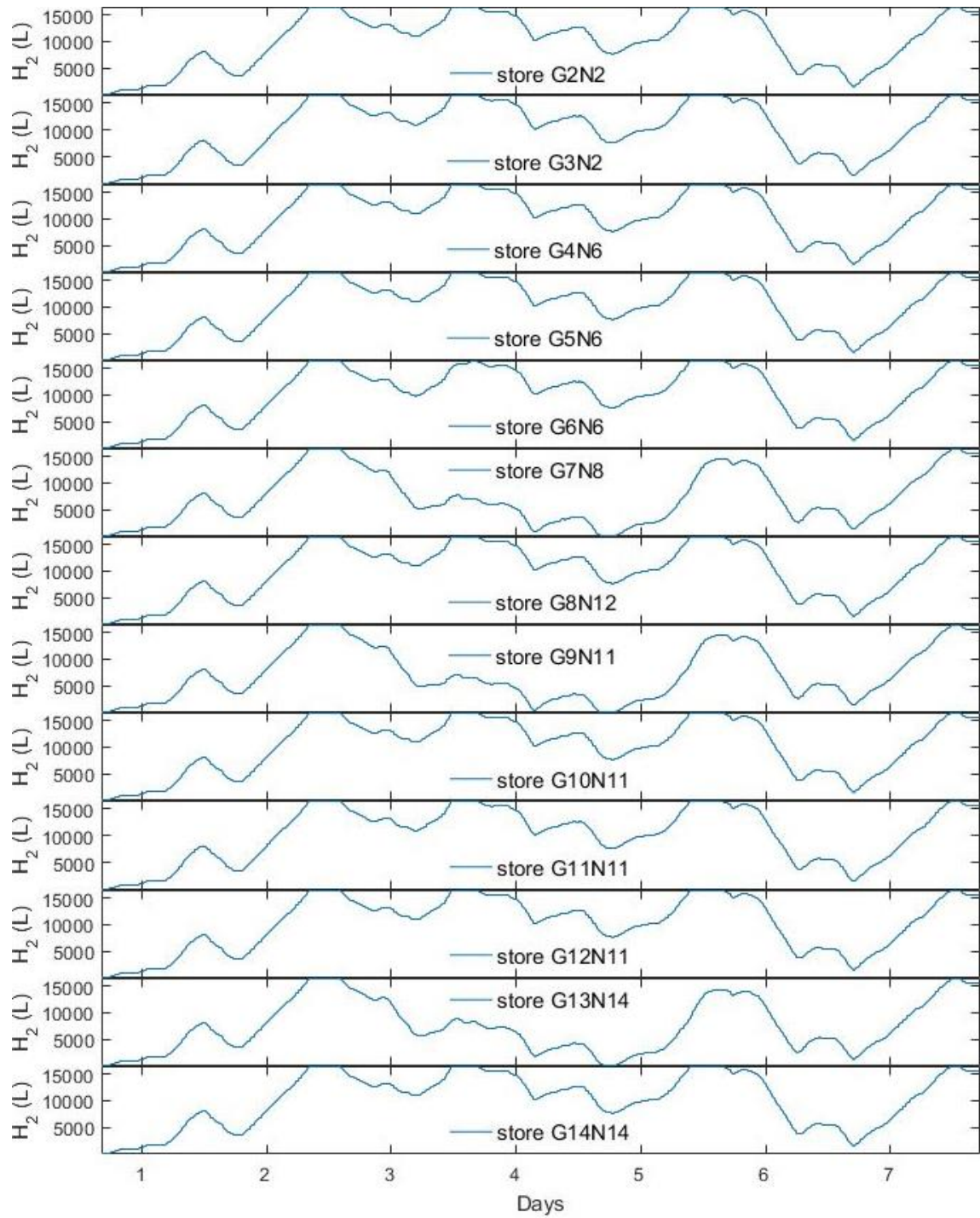
Fig. 4.23. Hydrogen storage behavior from HS's.
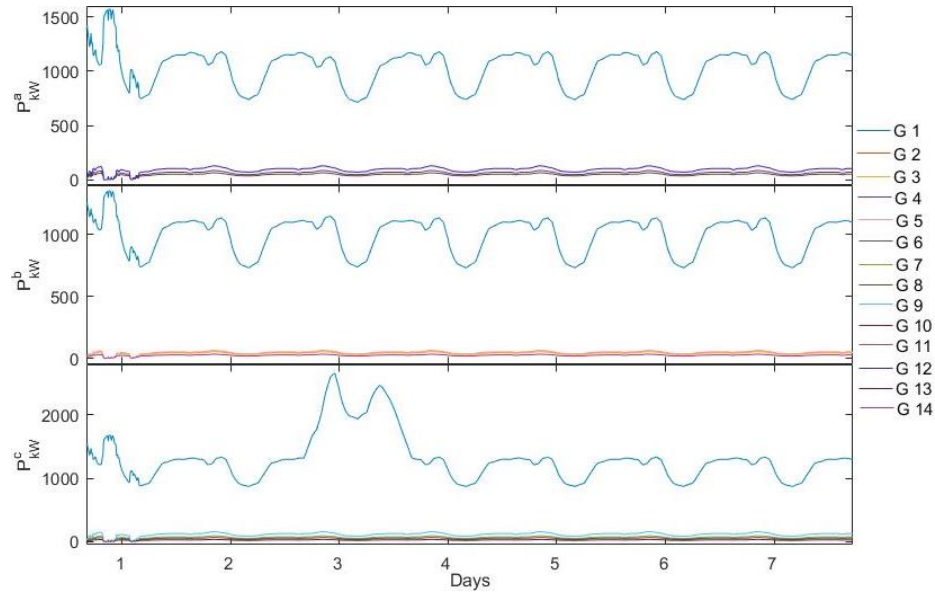
Fig. 4.24. Grid power generation.

The active power through lines from Fig. 4.25 displays a similar shape as in the base case seen in Fig. 4.15, with the difference that the power through lines, in this case, is less than in the base case, because the power injection from the HS follows the consumer load. It was considered that just a quarter of the consumers at HS connecting nodes has HS with demand-side management, which is seen in Fig. 4.15, with a 23.5% average power through lines reduction.
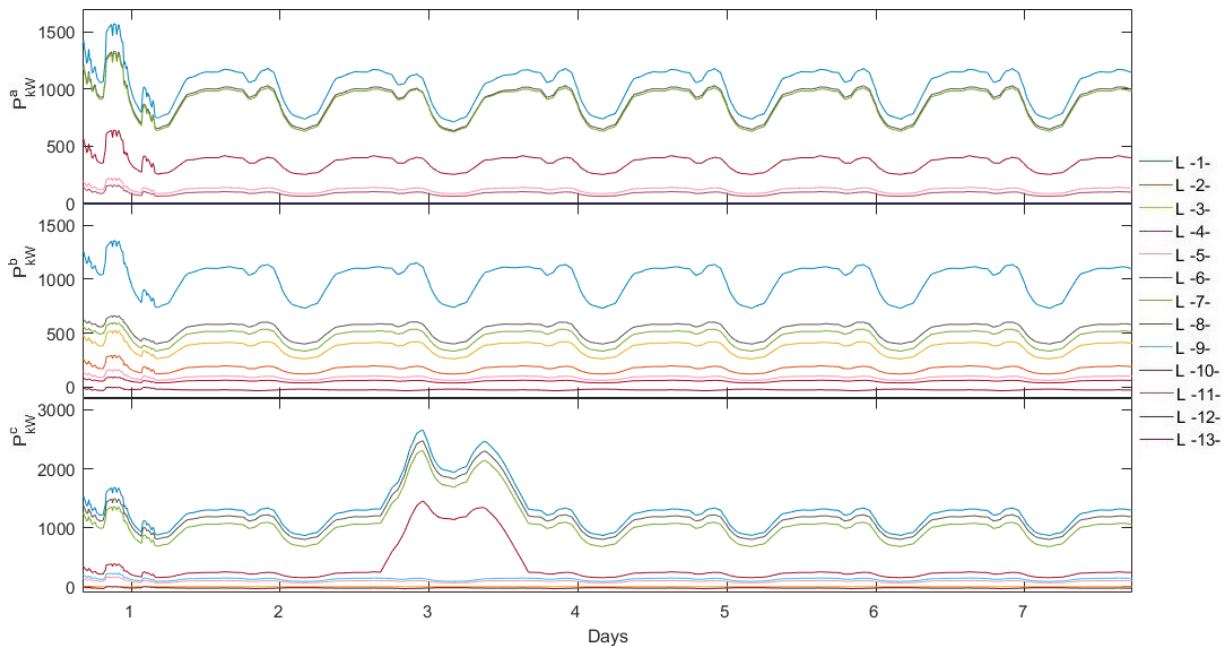
Fig. 4.25. Grid active power through lines.

The nodal voltages from Fig. 4.26 shows maximum values of 1.0361 p.u., 1 p.u. and 1 p.u., and minimum values of 0.9479 p.u., 0.9599 p.u. and 0.9104 p.u. per phase respectively, taking into account all nodes per phase. The nodal voltages are within the accepted limits, with an improvement of 0.13% in comparison to the base case.
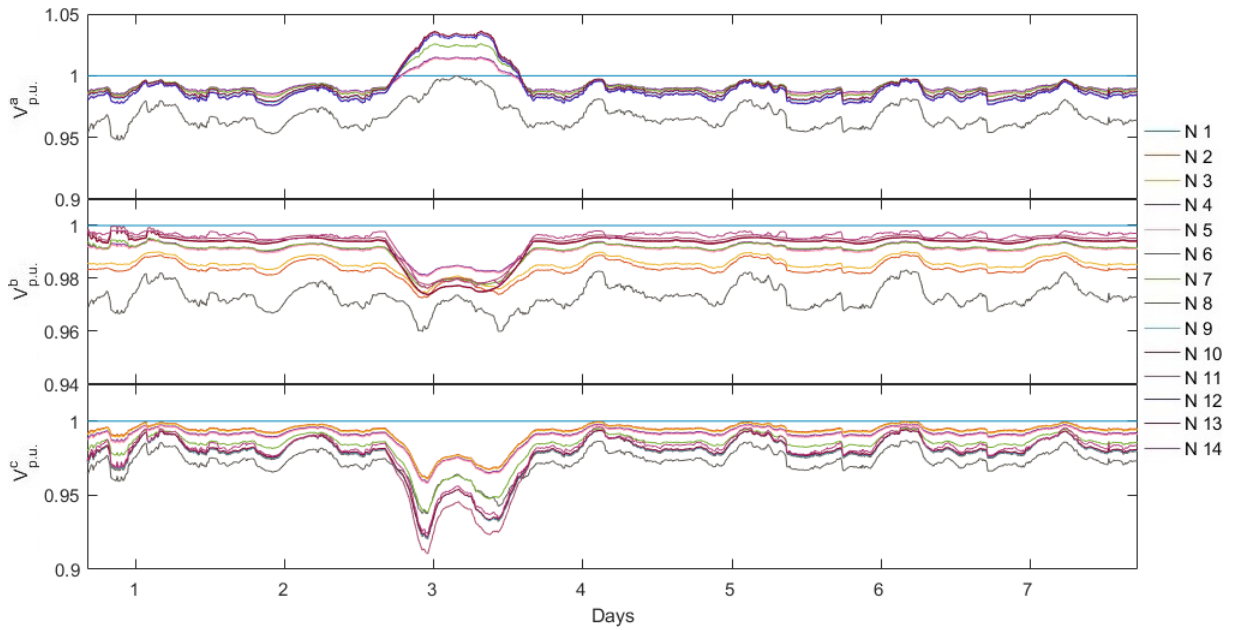
Fig. 4.26. Grid nodal voltages profile.

The power factor profile is presented in Fig. 4.27, with average values of 0.9986 in phase *a*, 0.997 in phase *b*, and 0.9979 in phase *c*. It is seen a percentage improvement of 64.25%, 32.62% and 27.93% per phase respectively when compared to the base case.
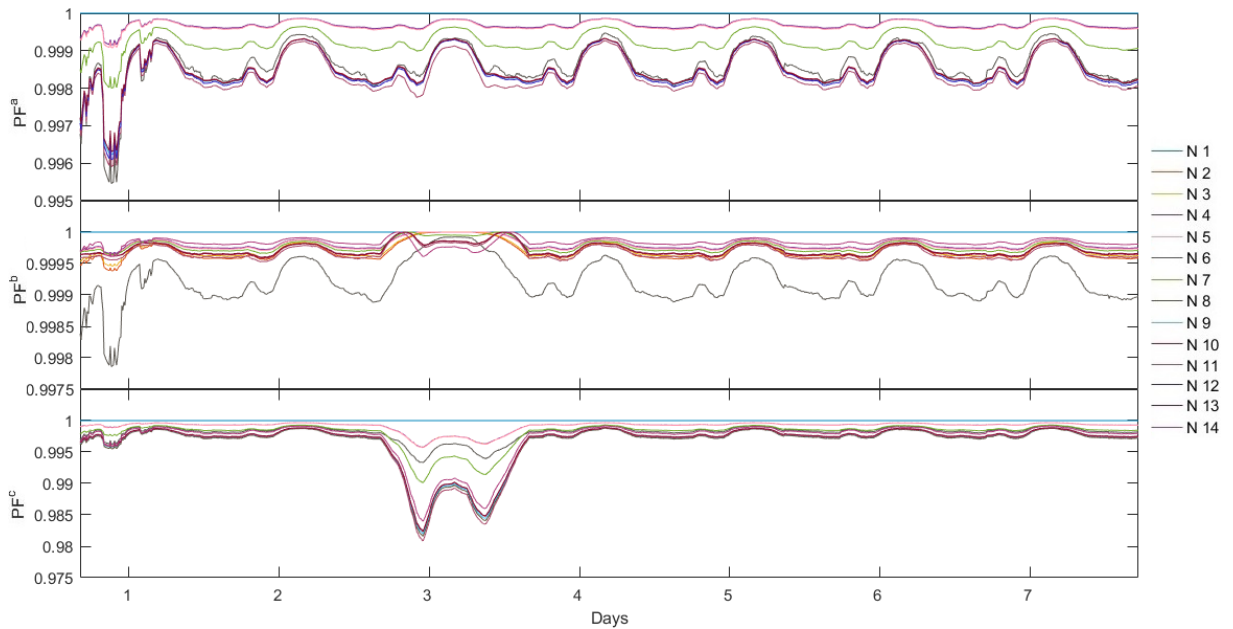
Fig. 4.27. Grid nodal power factor behavior.

The individual performance of the HSs can be seen in Fig. 4.28, where the output power supplies the final user's load curve. Because of the lack of hydrogen at the start-up, it is required power from the grid to supply the complete user's demand, as seen in orange in Fig. 4.28.
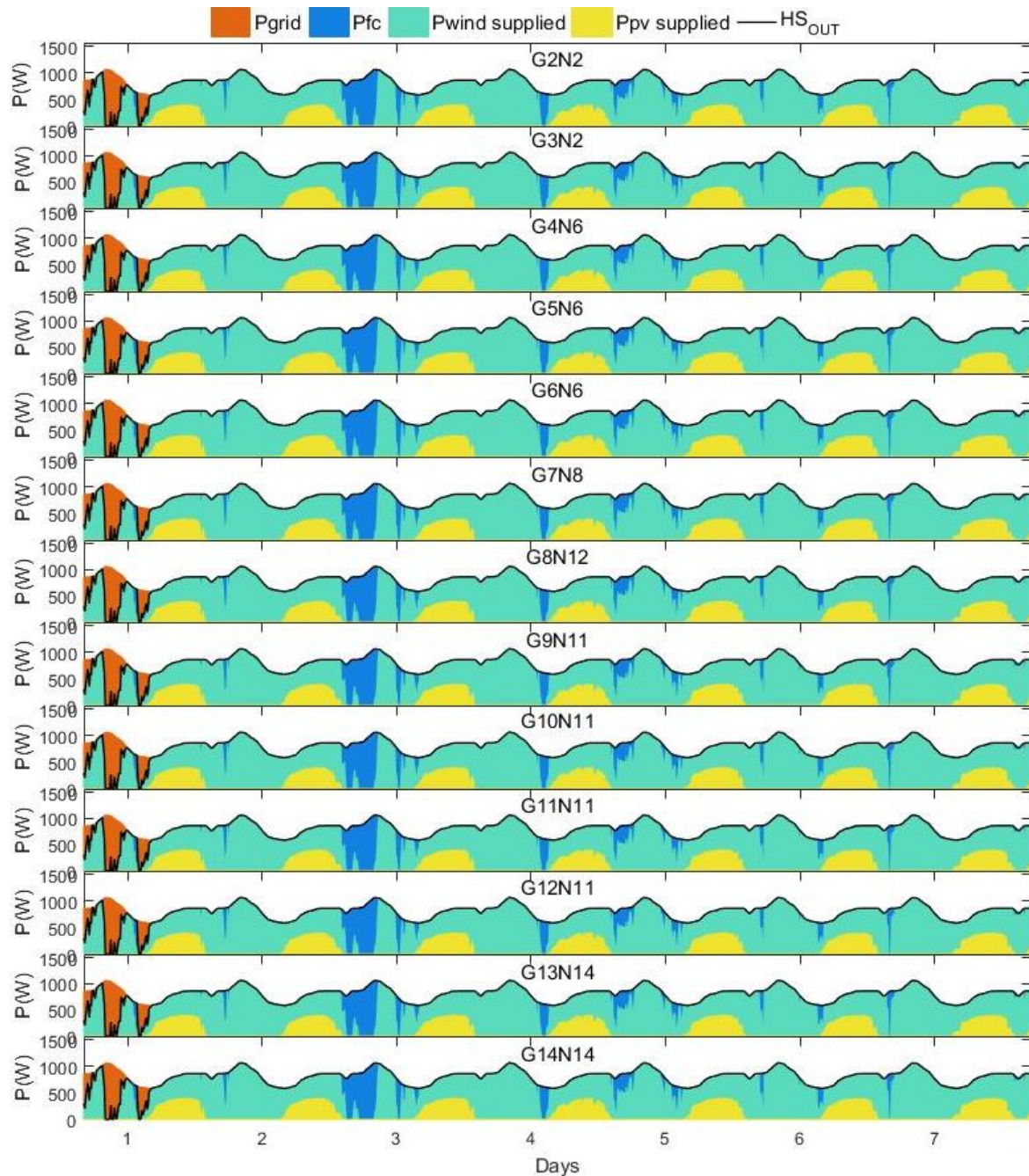
Fig. 4.28. Dispatched power from HS's.

The hydrogen storage behavior from each HS is shown in Fig. 4.29. It is noticeable the high average level of hydrogen stored due to the small amount of hydrogen used by the FC in the tested week. The legend identifies the generator number and location.
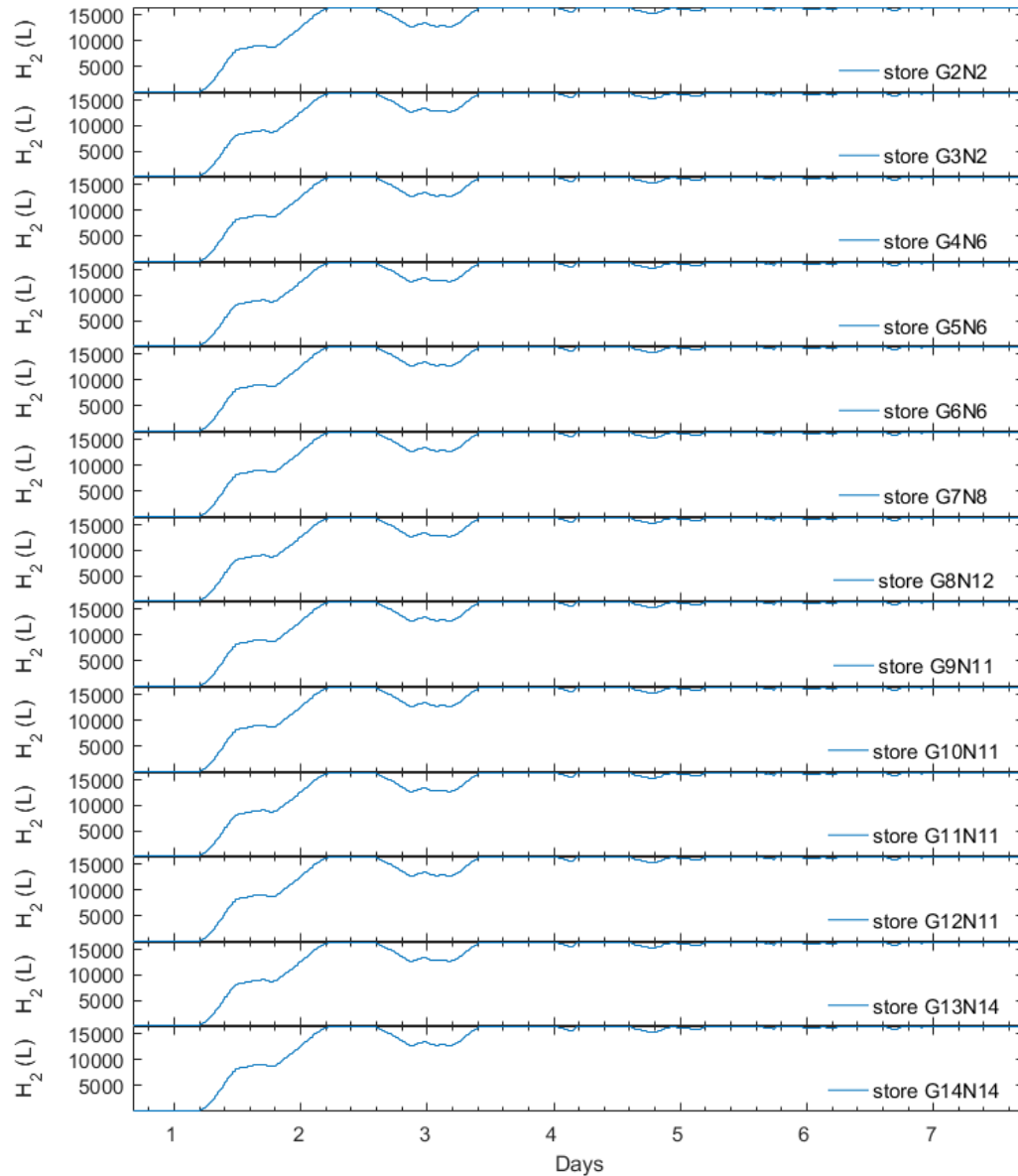
Fig. 4.29. Hydrogen storage behavior from HS's.

Hybrid systems implement EMS subjected to power factor and cost behavior, and prosumer method for demand-side management

In this scenario, as aforementioned, the HSs implement the previous EMS in an almost 50-50% mix control, where the HS from Fig. 4.12 named "Prosumer EMS" will follow the load curve and the ones named "HS EMS" will be programmed to improve the power factor at PCC and behave considering the cost curve profile from Fig. 4.13.

Initially, Fig. 4.30 shows the active power injections supplied by the various embedded HS with the programmed EMS. The HSs are connected per phase, considering the end users individuality. The grid supplier G1, shows a maximum generation similar to the base case at the beginning of the test week, being the start-up of the HSs. Also, it is presented a minimum generation of 378.53 kW,

421.23 kW, and 530.44 kW per phases *a*, *b*, and *c* respectively, which is an average of 29.36%, 21.19%, and 23.33% less than the base case at each phase.
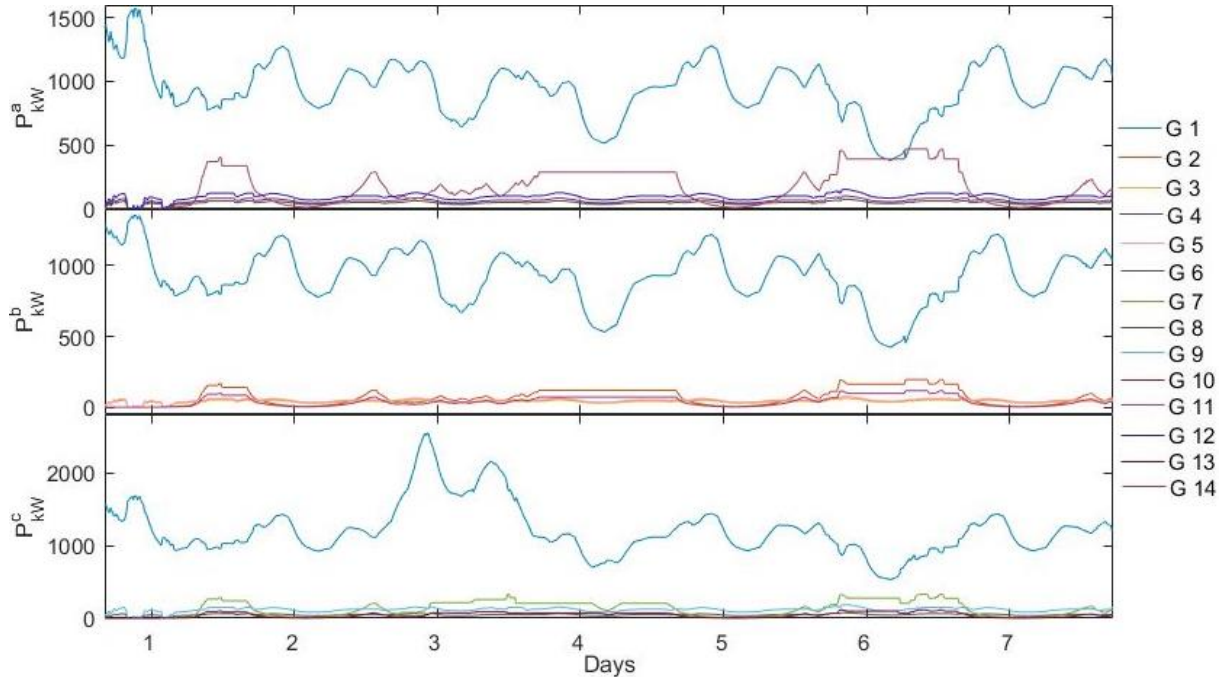
Fig. 4.30. Grid power generation.

A power flow reduction of 30.61% through lines can be noted in Fig. 4.31. Also, a change of power flow direction because of the "HS EMS" generation is very noticeable in lines 10, 13 and 9 mostly in the periods where the electricity price is high.
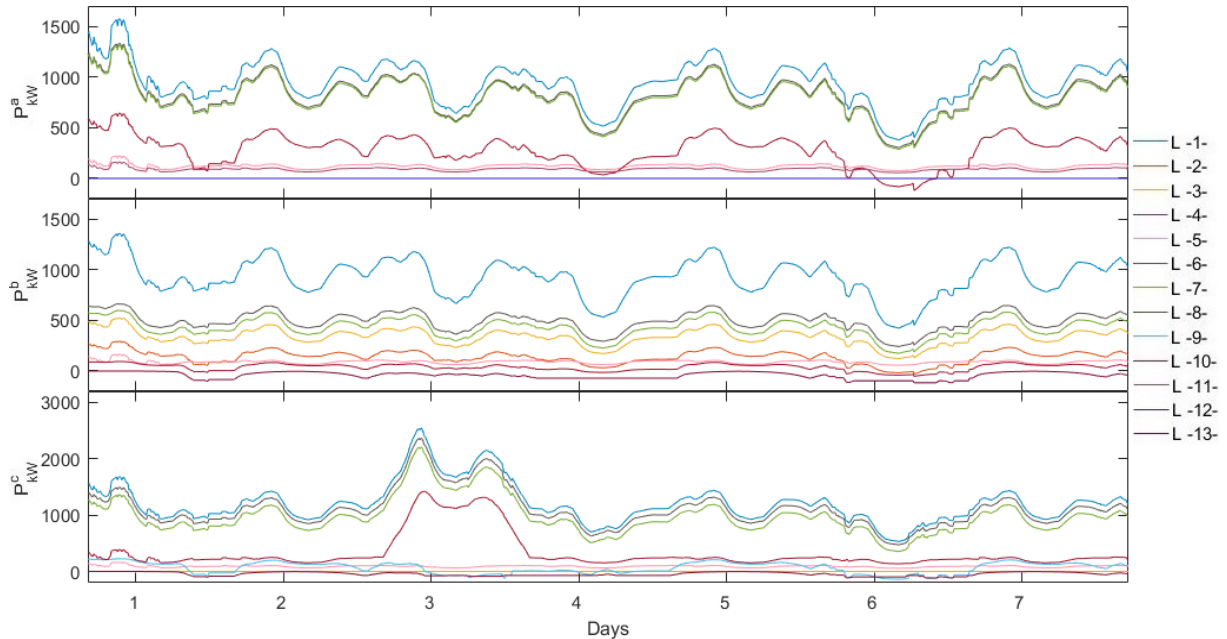
Fig. 4.31. Grid active power through lines.

Fig. 4.32 shows the nodal voltages profile presented in show values inside the accepted range, with a maximum of 1.032 p.u., 1.0085 p.u. and 1.0152 p.u. per phase, and minimum values of 0.9975 p.u., 0.9848 p.u. and 0.9913 per phase respectively. It is seen an average improvement of 0.9% in respect to the minimum values obtained at the base case.
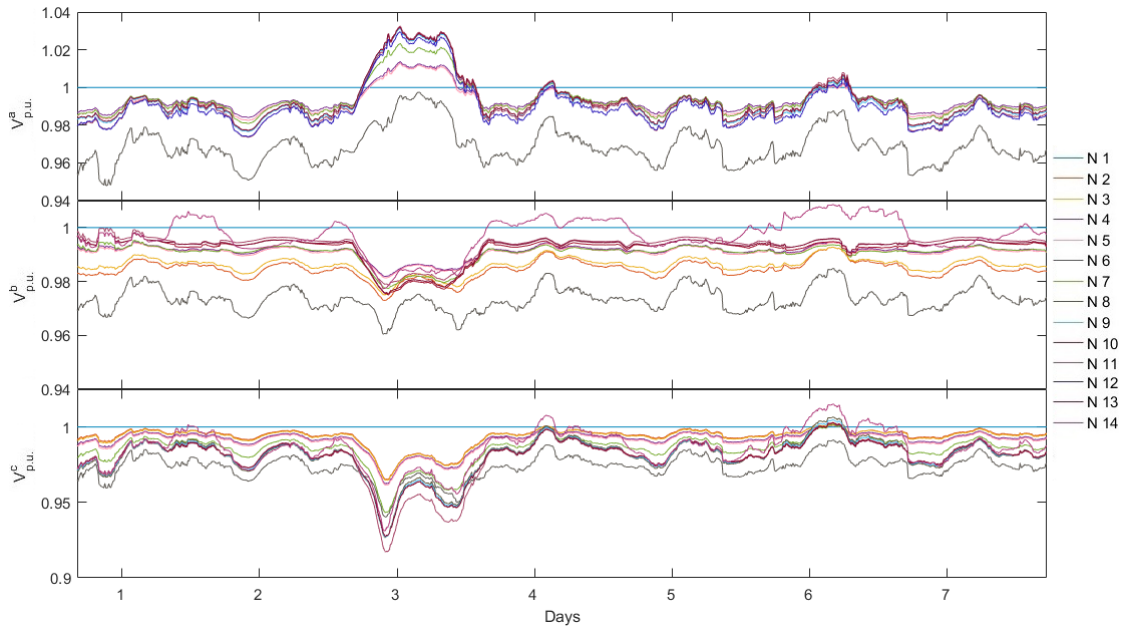
Fig. 4.32. Grid nodal voltages.

The power factor values are within the accepted limits as appreciated in Fig. 4.33, with an average value of 0.9991, 0.9997, and 0.9982 per phase, representing an improvement in respect to the base case of 54.92%, 41.73%, and 39.63% per phase.
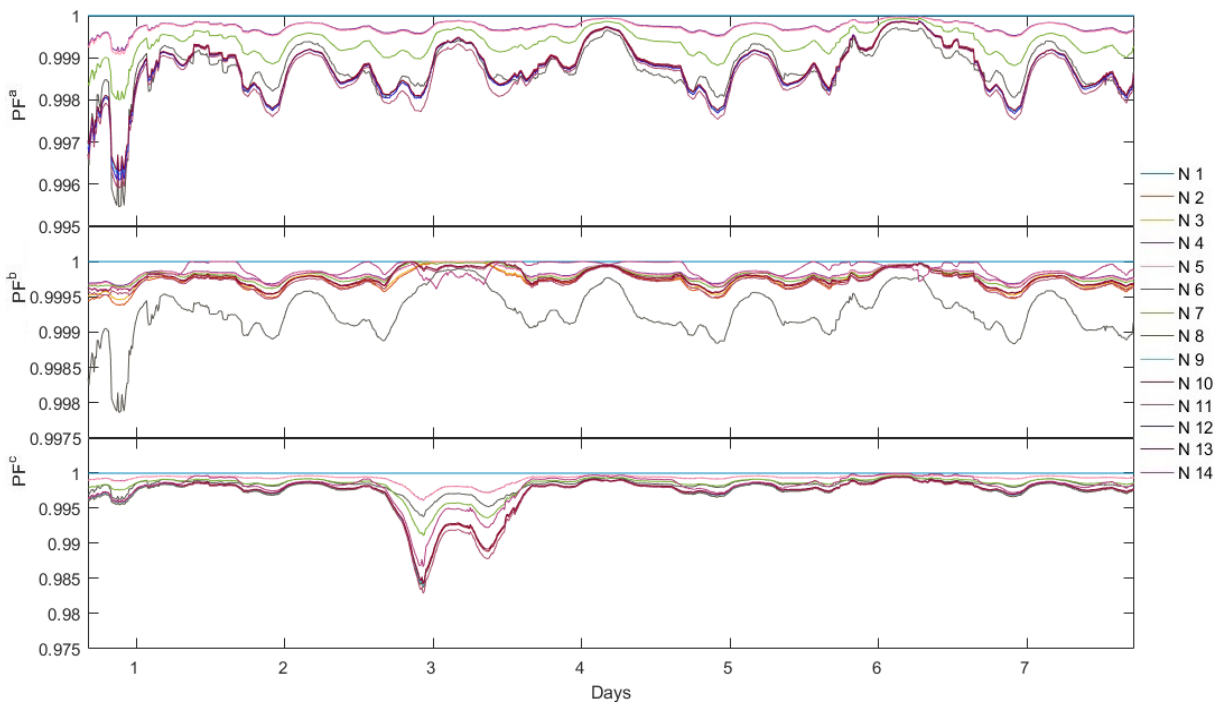
Fig. 4.33. Grid nodal power factor behavior.

The embedded HS individual performance is presented in Fig. 4.34 where the HSs dispatch is identified by the shape of the power generated. It can be noted the increase in power generated at the different HS when because of cost price and power factor disturbance, as well as the unbalanced generation as a result of the power factor value seen by the HS at PCC.
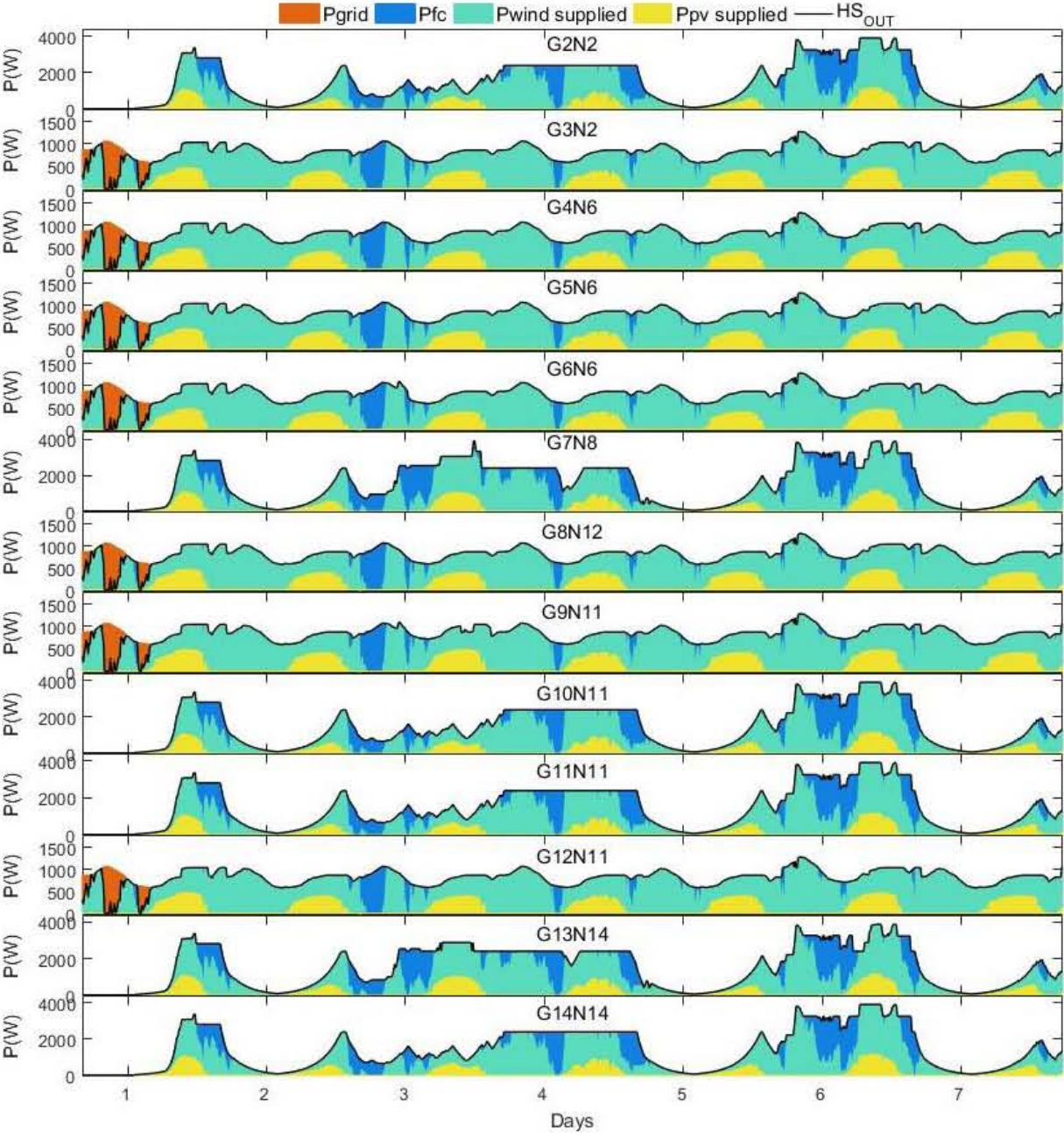
Fig. 4.34. Dispatched power from HS's.

The storage from each EMS is displayed in Fig. 4.35, where the hydrogen consumption is more detectable in the HS with the implemented EMS for power factor improvement and cost behavior.
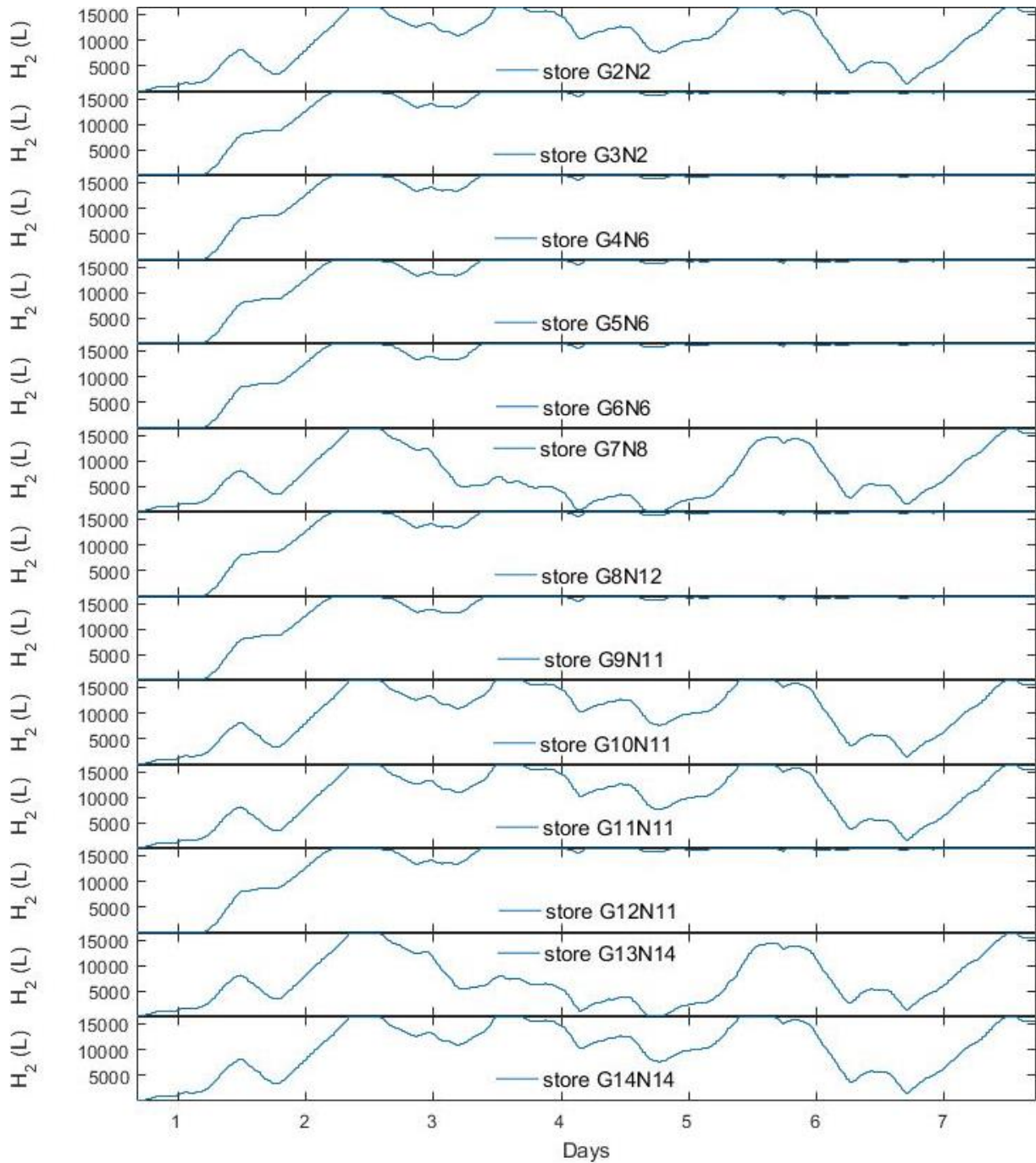
Fig. 4.35. Hydrogen storage behavior from HS's.

4.5   Discussion

Observing Fig. 4.22 and Fig. 4.34, it can be noted how the generators respond to the power factor disturbance, by increasing the generation of the HS that can sense the PF decrease. Also, it is observed that when there is an electricity price increase, the HS will inject more active power to the grid, contrary to when the price decrease.

The hydrogen storage behavior in Fig. 4.23, Fig. 4.29, and Fig. 4.35, it is noticeable that the first will present more activity due to the tasked amount of power generation and dispatch conditions of the EMS. In contrast, the second storage presents a good level of hydrogen at all time without much activity, because of the little amount of demand by households.

Comparing the overall active power generation from Fig. 4.14, Fig. 4.18, Fig. 4.24, and Fig. 4.30, it can be noticed that the peak generation, consequence of the recreated disturbance, is reduced a 17.55% from the obtained in the base case with the EMS subjected to power factor and cost behavior. An 11.65% reduction is seen, when all HS implement a demand-side management; and a 15.40% when the HS implemented a mix of the proposed EMS. This behavior is thanks to the EMS power factor stability considered in the MPC constraints when a disturbance occurs. Furthermore, it can be noticed on the first day of obtained results, that all cases present similar behavior of active power generated by the feeder as consequence of the HSs charging period.

The decreased of required active power supply from the feeder is mirrored in the active power transported through lines, presented in Fig. 4.15, Fig. 4.19, Fig. 4.25 and Fig. 4.31. The HSs connected as DG are providing power to its own and nearby loads to PCC, resulting in the decrease of active power through lines and power required from the feeder.

The PF performance has improved along the tested week, after the DG implementation with the proposed models; even when the load phenomenon on the third day occurs in phase *c* of node 11. At all cases, the general performance of PF is approached to the optimal value as seen in Fig. 4.21, Fig. 4.27, and Fig. 4.33 when compared with the results from the base case in Fig. 4.17.

The independent respond from each HS can be observed in Fig. 4.22, Fig. 4.28 and Fig. 4.34, where comparing them with results from previous chapters, it can be seen how when the electricity price is low the power supplied to the grid decrease; opposite to the days with a high price, in which the supplied active power from the HS increase considering the grid code as to not disturb the frequency. Furthermore, it can be appreciated how when in an occurrence of power factor deviation, the implemented algorithm will try to improvise it.

4.5.1 Remark behaviors

Observing the respond of the power factor at the different tests and comparing them with the obtained at the base case, it is seen that from a lower 0.9762 value in Fig. 4.17, to a lower 0.9808 value in Fig. 4.27, to a lower 0.985 in Fig. 4.33 and finally a lower 0.9877 in Fig. 4.21; a 19.33%, 36.48% and 52.67% of power factor improvement respectively is observed in Fig. 4.36. It is noticeable the 33.34% difference between just demand management and an EMS subjected to the PF behavior.

The reduction of deviation on nodal voltages is apparent as clearly seen in Fig. 4.37, and along the tested week after the DG implementation with the proposed models. The lower value is found in node 11 at phase c. From a lower 0.9017 p.u. value in Fig. 4.16 and Fig. 4.37, to a lower value of 0.9104 p.u. with the demand-side management EMS seen in Fig. 4.26, to a lower 0.9223 p.u. implementing a mix EMS seen in Fig. 4.32, to a 0.9371 p.u. value with all HS's implementing an EMS with power factor optimization as in Fig. 4.20. The improvement can be observed for each case in Fig. 4.37, which express in percentage represents an 8.81%, a 20.94% and a 36.01% respectively.
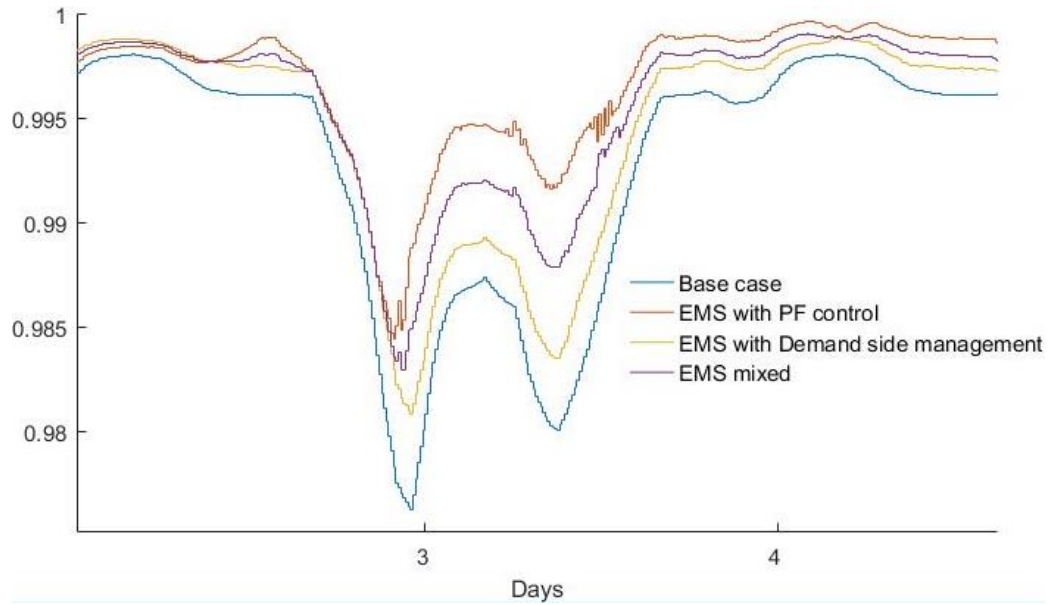
Fig. 4.36. Comparing nodal power factor between Base, EMS without control and EMS with control.
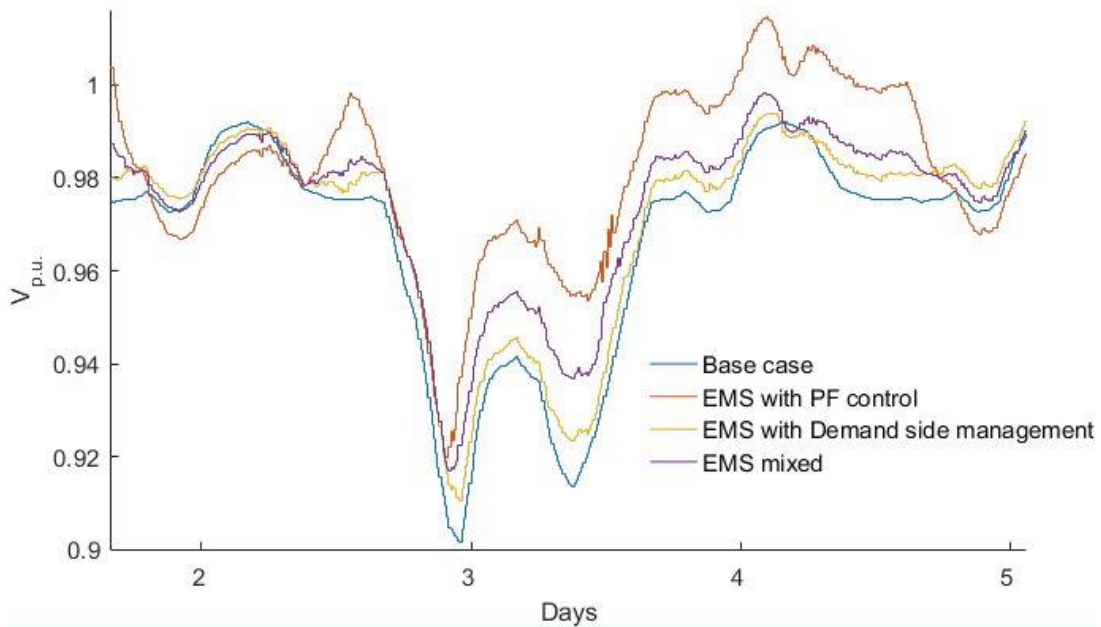
Fig. 4.37. Nodal voltage deviation comparison.

The base case presents 100,185.55 kW total active power losses through lines, seen in Fig. 4.38. A losses reduction is seen in Fig. 4.39 of 50,670.9 kW, equivalent to a 49.42% reduction compared to the base case. A losses reduction is seen in Fig. 4.40, been of 65,359.25 kW or a reduction of 34.7% in respect to the base case. Fig. 4.41 shows a total active power loss of 57,439.1 kW, meaning a 42.66% losses reduction.
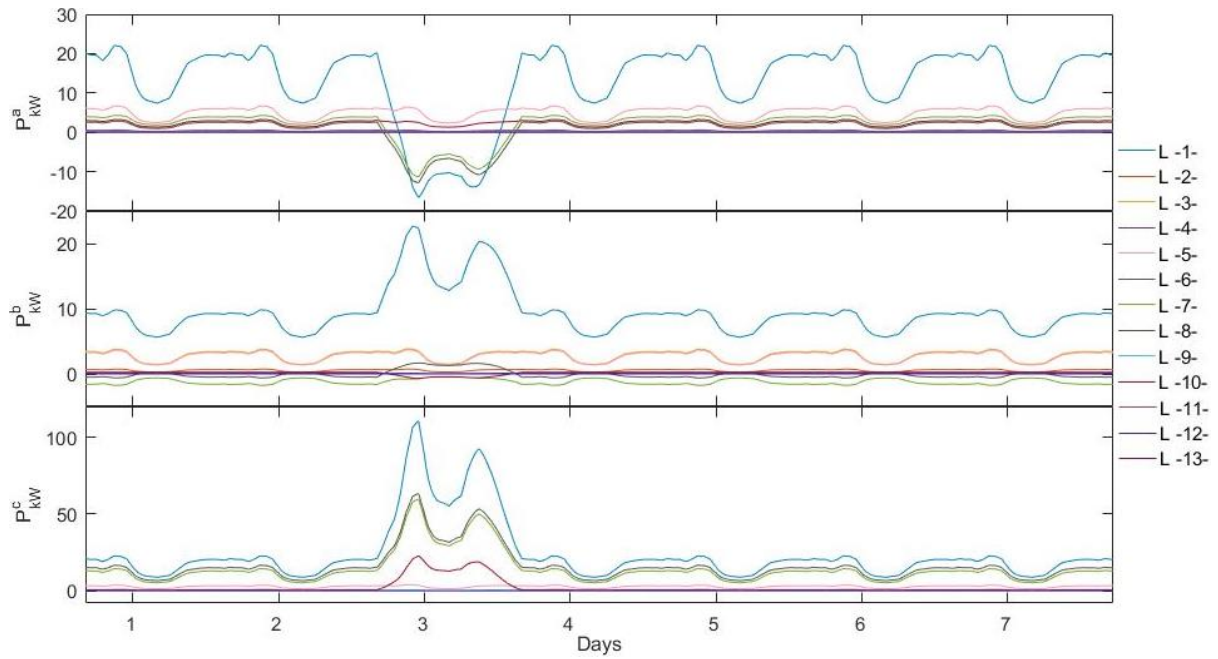
Fig. 4.38. Base case grid active power losses through lines.
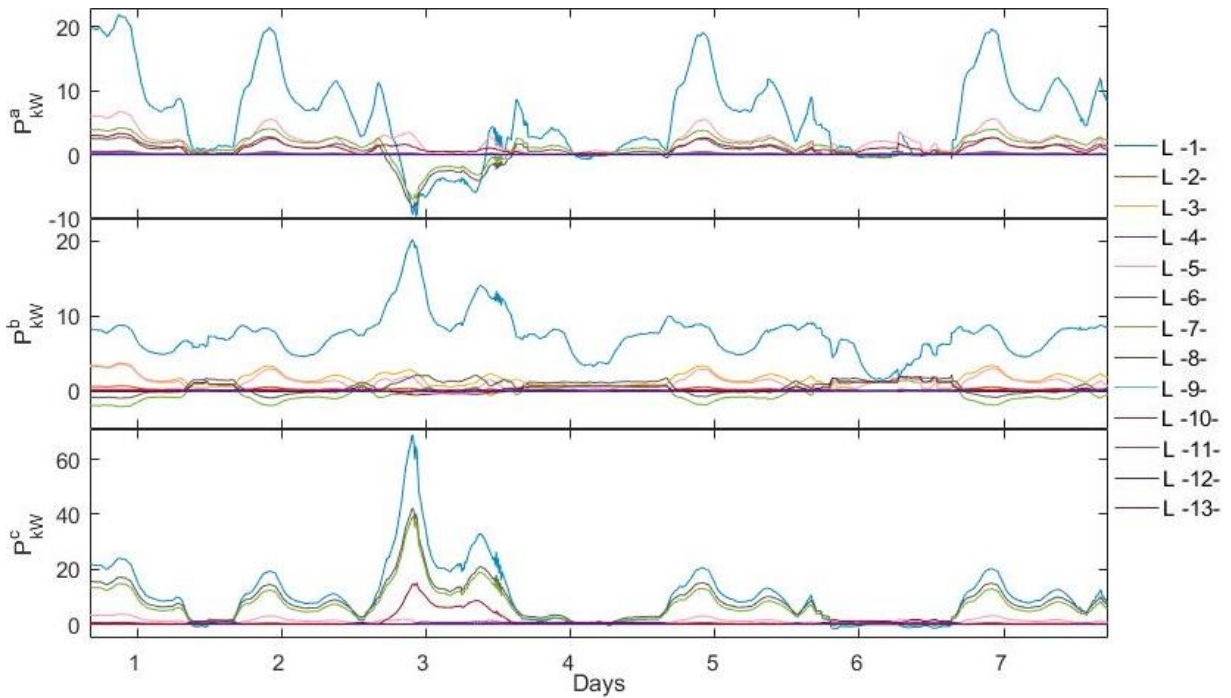
Fig. 4.39. Grid active power losses through lines with EMS subjected to power factor and cost behavior.
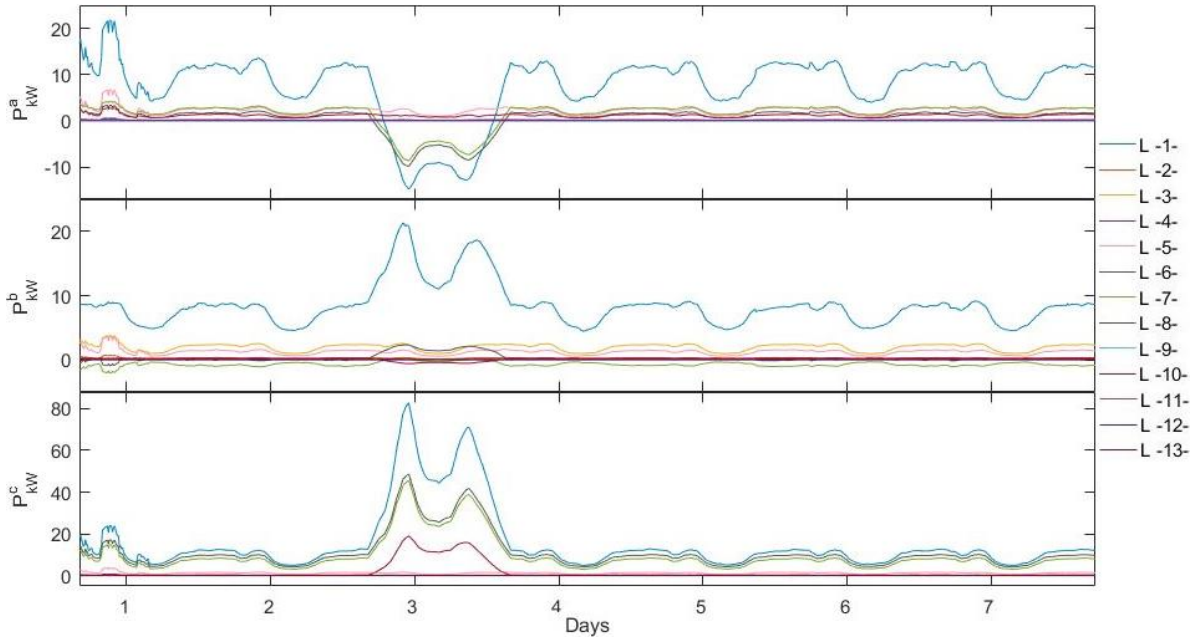
Fig. 4.40. Grid active power losses through lines with EMS prosumer method for demand-side management.
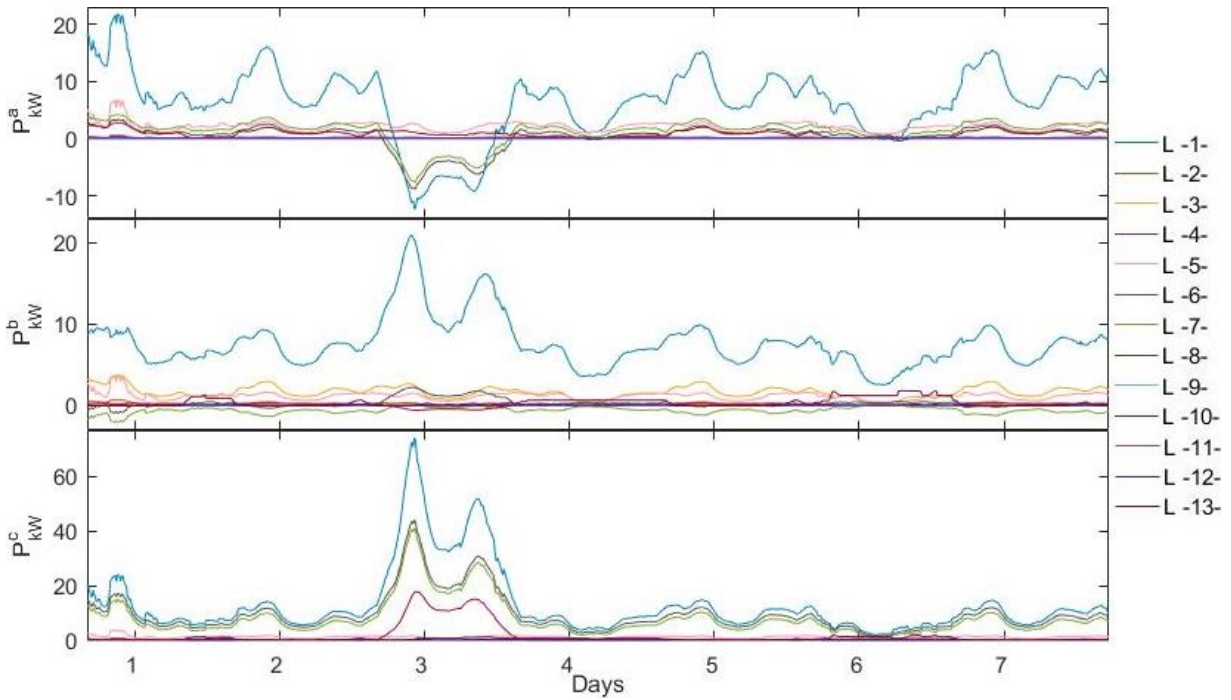
Fig. 4.41. Grid active power losses through lines with mixed EMS.

Comparing the overall active power generation from Fig. 4.14, Fig. 4.18, Fig. 4.24 and Fig. 4.30, the feeder G1 generation is reduced due to the influence of the HSs with the proposed EMS implemented. At the base case, the mean generation is 1,340.13 kW, 1,174.11 kW, and 1,577.36 kW per phase respectively, whereas at case one an average of 784.32 kW, 857.09 kW, and 1,063.7 kW is presented, meaning a reduction of 41.47%, 27% and 32.56% at each phase. At case two is seen an average generation from G1 of 1030.70 kW, 998.75 kW and 1305.24 kW showing a

89

reduction of 23.09%, 14.94% and 17.25% per phase. Furthermore, in case three a reduction per phase of 29.36%, 21.19%, and 23.33% is seen, with average generation values per phase of 946.7 kW, 925.25 kW and 1209.29 kW respectively.

The behavior at the different scenarios of the power supplied by the grid feeder is compared in Fig. 4.42. At all phases, it is seen that the HSs with all EMS programmed for PF control, presents a 33.88% less required power supply from the grid feeder. Followed by the scenario in which a mix of programmed EMS is implemented in the HSs with 24.69%, and an 18.49% from the HS with demand-side management because of the assumption of a quarter of users implementing HSs. These results are reflected in the power losses at each scenario. This behavior is because of the scenario where all HS use PF control EMS, is the one that presents more power injection from the HSs.
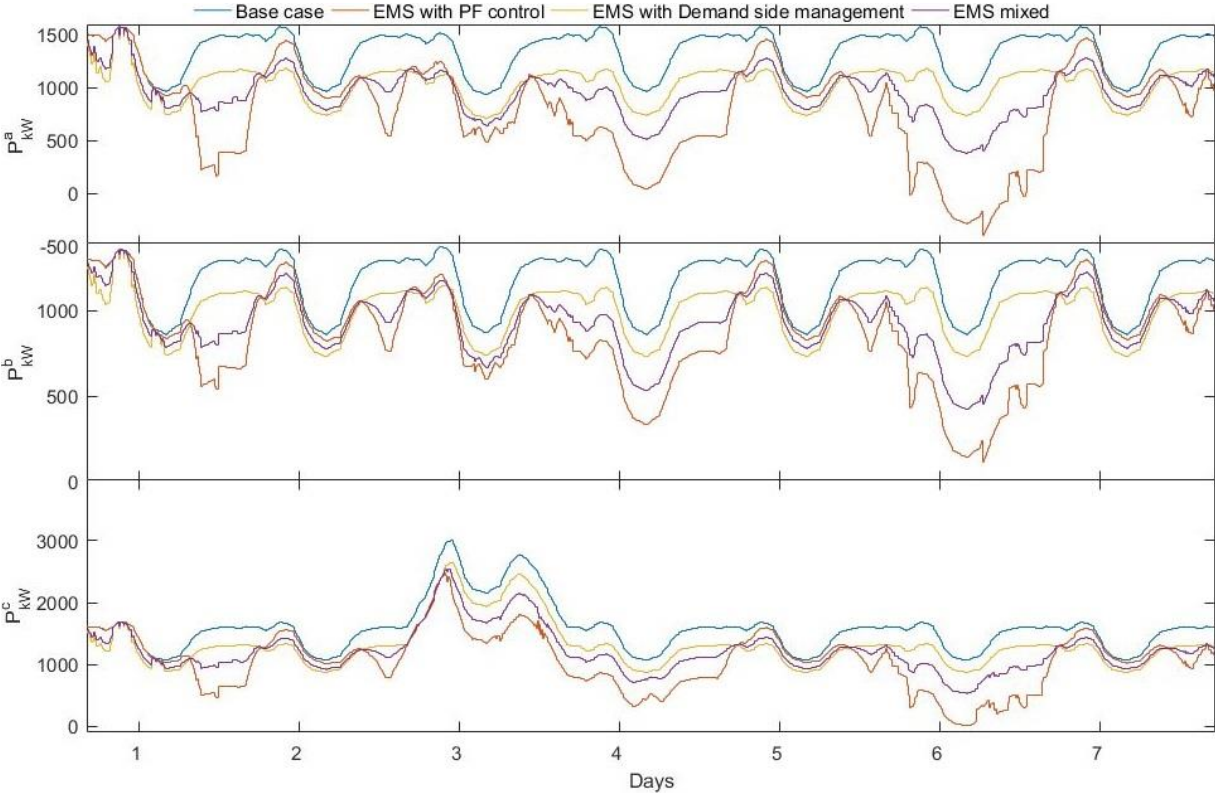
Fig. 4.42. Comparison of power supplied by the grid feeder.

4.5.2 Findings

The decrease of required active power from the general network, allows the distribution network to work more independently from the central generation. This opens the road to divide the distribution network into several interconnected microgrids. This way, when a fault happens, the nearby distributed generation may supply the required load.

DG integration allows the connection of other loads into the distribution network as consequence of the reduction of active power through the lines; always considering the overhead lines and underground cables chargeability.

Here, it was assumed a 25% users implementing the proposed EMS for demand-side management at connection nodes, proving that an increase in the trend may develop the crowd energy concept stated in Chapter 3.

It would be ideal that all HS connected to the grid, implement the proposed EMS focus on power factor behavior which is the one presenting the best results as seen in Section 4.4.2 and discussed in Section 4.5.

4.6   References

[1]   A. Pina, C. Silva, and P. Ferrão, "The impact of demand-side management strategies in the penetration of renewable electricity," *Energy*, vol. 41, no. 1, pp. 128–137, May 2012.

[2]   F. Katiraei and M. R. Iravani, "Power Management Strategies for a Microgrid With Multiple Distributed Generation Units," *IEEE Trans. Power Syst.*, vol. 21, no. 4, pp. 1821–1831, Nov. 2006.

[3]   C. Angeles-Camacho, "Phase domain modeling and simulation of large-scale power systems with VSC-based FACTS equipment," University of Glasgow, 2005.

[4]   J. Machowski, J. W. Bialek, and J. R. Bumby, *Power system dynamics : stability and control*, 2nd ed. England: John Wiley & Sons, Inc., 2008.

[5]   C. Acha, Enrique.; Fuerte-Esquivel, Claudio; Ambriz-Pérez, Hugo; Angeles-Camacho, *FACTS : modeling and simulation in power networks*. John Wiley & Sons, Inc., 2004.

[6]   H. A. Smolleck and R. R. Shoults, "A straightforward method for incorporating mutually-coupled circuits into the bus admittance matrix using the concept of artificial branches," *IEEE Trans. Power Syst.*, vol. 5, no. 2, pp. 486–491, May 1990.

[7]   N. D. Tleis, *Power systems modeling and fault analysis : theory and practice*. Elsevier/Newnes, 2008.

[8]   T.-H. Chen, M.-S. Chen, T. Inoue, P. Kotas, and E. A. Chebli, "Three-phase cogenerator and transformer models for distribution system analysis," *IEEE Trans. Power Deliv.*, vol. 6, no. 4, pp. 1671–1681, 1991.

[9]   F. Alvarez-Mendoza, P. Bacher, H. Madsen, and C. Angeles-Camacho, "Stochastic model of wind-fuel cell for a semi-dispatchable power generation," *Appl. Energy*, 2017.

[10]   G. Ramos Niembro, "Modelado de la curva de usuarios domésticos para la implementación de medidas de administración por el lado de la demanda," Mexico city, 1998.

[11]   CRE, "Reporte Mensual de Estadísticas del Sector Eléctrico," Mexico city, 2014.

[12]   M. R. Maqueda Zamora and L. A. Sánchez Viveros, "Curvas de demanda de energía eléctrica en el sector doméstico de dos regiones de México," *Boletín IIE Gestión del uso Efic. la energía eléctrica*, vol. 35, no. 4, p. 54, 2011.

[13]   G. Ramos Niembro, R. Fiscal Escalante, M. Maqueda Zamora, J. Sada Gámiz, and H. Buitrón Sánchez, "Variables que influyen en el consumo de energía eléctrica," *boletín iie*, vol. 23, pp.

11–18, 1999.

[14] D. M. Tagare, *Electric power generation : the changing dimensions*. John Wiley & Sons, Inc. - IEEE Press, 2011.

[15] M. Bollen and F. Hassan, *Integration of distributed generation in the power system*. New Jersey: John Wiley & Sons, Inc., 2011.

[16] L. L. Lai and T. F. Chan, *Distributed generation : induction and permanent magnet generators*. London: John Wiley & Sons, Inc.-IEEE Press, 2007.

[17] S. Chowdhury, P. Crossley, and S. P. Chowdhury, *Microgrids and active distribution networks*. Institution of Engineering and Technology, 2009.

[18] Comisión Federal de Electricidad-CFE, "Ley para el aprovechamiento de energías renovables," Mexico city.

[19] Comisión Federal de Electricidad-CFE, "Reglamento de la ley para el aprovechamiento de energías renovables," Mexico city.

[20] Diario Oficial, "Ley de servicio publico de energia eléctrica. DOF 22-12-1975," pp. 1–21, 2013.

[21] Diario Oficial, "Ley de industria eléctrica," 2014.

[22] Comisión Federal de Electricidad-CFE, "Informe Anual," p. 63, 2015.

[23] Comisión Federal de Electricidad-CFE, "Interconexión a la red eléctrica de baja tensión de sistemas fotovoltaicos con capacidad hasta 30 kW," p. 48, 2008.

[24] Comisión Federal de Electricidad-CFE, "Especificaciones técnicas pequeña escala," Mexico city.

[25] Comisión Federal de Electricidad-CFE, "Características de los equipos de medición," Mexico city.

[26] I. Erlich, F. Shewarega, and S.-J. Lee, "Grid codes on power systems with significant renewable-based generation," in *Smart grid handbook*, 1st ed., C.-C. Liu, S. McArthur, and S.-J. Lee, Eds. Duisburg, Germany: John Wiley & Sons, 2016, pp. 321–332.

[27] E. M. G. Rodrigues, G. J. Osório, R. Godina, A. W. Bizuayehu, J. M. Lujano-Rojas, and J. P. S. Catalão, "Grid code reinforcements for deeper renewable generation in insular energy systems," *Renew. Sustain. Energy Rev.*, vol. 53, pp. 163–177, Jan. 2016.

[28] Centro Nacional de Control de Energía, "Código de Red," *D. Of. la Fed.*, p. 179, 2016.

CHAPTER 5

CONCLUSIONS AND FUTURE WORK

The previous chapters outline the main ideas behind this Ph.D. research project, giving account of the results achieved. As originally planned, the project has gone through several stages concerning the modeling recent power generation used in hybrid systems (HS) based renewable energy sources (RES). The models were integrated with forecast algorithm for later implementation in energy management systems (EMS) by means of model predictive control (MPC). The power management systems were successfully modeled, coded and implemented in the HSs to be embedded into a multiphase power flow program recreated in MATLAB ®.

The computational efficiency of the multiphase load flow program has been shown, in cases where the test networks have lines and cables with single-, two- and three-phases. Balanced and unbalanced test networks have been used to assess the operation of the models. Thus, EMS proposed are mass connected to a distribution network to test the impact in the grid characteristics as nodal voltage magnitude, power factor, and active power.

5.1   Conclusions

The forecast and MPC implementation in the EMS algorithm, proves to be capable of making the active power generation from a non-dispatchable into a semi-dispatchable energy source where the power trajectory can be modeled based on the final user's need. The semi-dispatchability of the HS depends significantly on the nominal total value of the FC and hydrogen storage. Consequently, the frequency of the system will not be compromised because of sudden changes in wind power. The proposed approach is meant to work in the distribution level for housing sectors and small stores.

In real life application, the EMS model proposed will help to keep the net frequency and power factor within its tolerance boundaries, given the fact that it will not be disturbed by the EMS approaches when connected as distributed generation (DG) into the network, thanks to the no uncertainty and no intermittence in the HS output power.

Prosumer management systems, can mitigate the adverse impacts of renewable energy electric generation when integrated into a distribution network. Additionally, it can improve the grid behavior.

When the priority is completely given to the FC generation, there is a high risk of running out of hydrogen and not meeting the full capacity of the RES.

Another finding is that to generate a completely constant output power; there is a need to "sacrifice" other features such as magnitude power, storage limits, and even the times to recharge

the hydrogen tank according to the needs of the end user. Thus, it is recommended to compromise the involved parties regarding the EMS design.

The implementation of forecast is demonstrated to be of great importance in planning the power dispatch, improving and taking contingency measurements as to avoid disturbing the network or even improving the network at the connection point if required.

The implementation of forecasting to compute the power trajectory of the generation system, concedes the benefit of prior planning of power dispatch; also, to inform the SO and not disturb the frequency of the network when connected as DG.

Forecast applied to wind and radiation for later used in the MPC, allows the manipulation of the devices that integrate the HS, to obtain the desired output power while avoiding penalties.

The designed Wind-Photovoltaic-Fuel cell system approach, using EMS algorithm and forecast implementation, allows adjusting the output power of the system to not disturb the original characteristics of the network.

The EMS flexibility helps to improve the distribution network characteristics. Thanks to the grid code considered in the EMS power dispatch, the frequency is not disturbed as consequence of sudden changes in the active power, and the prior knowledge of the SO concerning the one hour-ahead generation forecasted. Furthermore, it is proved the improvement of power

This research gives an idea for private generation to be decentralized into DG at distribution networks, making use of the proposed EMS generation approaches. It opens the energy market not just to prosumers with demand-side management, but also to mini- and micro-entrepreneurs for decentralized energy supply based on RES.

5.2 Future works

This research opens the doors in fields like market, statistics, technology development, energy and of course electric. Future works are considered like:

- Optimum DG location in distribution networks aimed to crowd concept.

- Integration of electric cost to the developed EMS approach, to improve the relation user-market.

- Long-term forecast analysis aimed at RES and market behavior, to be applied in the proposed EMSs.

- Communication support with the system operator or system controller, as to send updated information of the devices state and behavior, aimed mostly to mass DG integration, with the purpose of applying data mining concepts.

APPENDIX A

ROUGHNESS CLASSES AND ROUGHNESS LENGTH

Table A.1. Roughness Classes and Roughness Length [1]

Roughness Class	Roughness Length (m)	Energy Index (%)	Landscape Type
0	0.0002	100	Water surface
0.5	0.0024	73	Completely open terrain with a smooth surface, i.e. concrete runways in airports, mowed grass, etc.
1	0.03	52	Open agricultural area without fences and hedgerows and very scattered buildings. Only softly rounded hills
1.5	0.055	45	Agricultural land with some houses and 8 meter tall sheltering hedgerows with a distance of approx. 1250 meters
2	0.1	39	Agricultural land with some houses and 8 meter tall sheltering hedgerows with a distance of approx. 500 meters
2.5	0.2	31	Agricultural land with many houses, shrubs and plants, or 8 meter tall sheltering hedgerows with a distance of approx. 250 meters
3	0.4	24	Villages, small towns, agricultural land with many or tall sheltering hedgerows, forests and very rough and uneven terrain
3.5	0.8	18	Larger cities with tall buildings
4	1.6	13	Very large cities with tall buildings and skyscrapers

ACTIVE POWER-FREQUENCY AND VOLTAGE ANGLE RELATIONSHIP IN DISTRIBUTION NETWORKS

The power generation-load balance of the system gives the frequency stability in a power system; any unbalance will affect the frequency. The presence of DG does not create great variations in power in a timescale of minutes, where the primary control works. An indirect consequence of a large-scale amount of DG is that there will be less conventional generation available for providing the primary reserve and the primary control.

Any loss of primary reserves should be made up by the secondary reserves. The reduction in secondary reserves will be made up from the tertiary reserves, which cover all timescales from 15 minutes onward. The transmission system operator starts new production units or changes the set points of units already in operation to accommodate for any depletion of primary and secondary reserves.

In a timescale of hours, DG provides the largest variations in production [18]. The unpredictability of the production is what matters to the transmission system operation.

To explain the active power-frequency relation in a more understandable way, let us analyze the circuit from Fig. B.1, which shows the active and reactive power flowing into a line from point A to B.

(a)

(b)
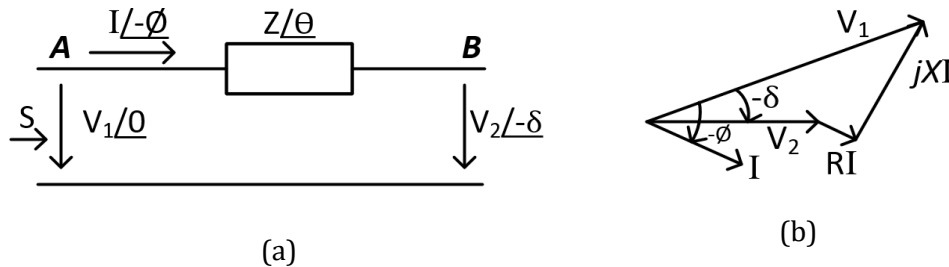
Fig. B.1. (a) Power flow through a line. (b) Phasor diagram.

Fig. B.**1** can be described mathematically as [19]

$$S = V_1 I^* = V_1 \left(\frac{V_1 - V_2}{Z} \right)^* \tag{B.15}$$

$$S = V_1 \left(\frac{V_1 - V_2 e^{j\delta}}{Z e^{-j\theta}} \right) \tag{B.16}$$

$$S = \frac{V_1^2}{Z} e^{j\theta} - \frac{V_1 V_2}{Z} e^{j(\theta + \delta)}. \tag{B.17}$$

Thus, the active and reactive power flowing into the line are

$$P = \frac{V_1^2}{Z} \cos(\theta) - \frac{V_1 V_2}{Z} \cos(\theta + \delta) \tag{B.18}$$

$$Q = \frac{V_1^2}{Z} \sin(\theta) - \frac{V_1 V_2}{Z} \sin(\theta + \delta) \tag{B.19}$$

with $\boldsymbol{Z e^{j\theta} = R + jX}$, (B.15) and (B.16) are rewritten as

$$P = \frac{V_1}{R^2 + X^2} [R(V_1 - V_2 \cos(\delta)) + XV_2 \sin(\delta)] \tag{B.20}$$

$$Q = \frac{V_1}{R^2 + X^2} [-RV_2 \sin(\delta) + X(V_1 - V_2 \cos(\delta))]. \tag{B.21}$$

For overhead lines $X \gg R$, therefore the resistance R may be neglected. If also the power angle is small, then $sin(\delta) = \delta$ and $cos(\delta) = 1$ [20]. In that case, equations (B.20) and (B.21) become

$$P \approx \frac{V_1 \ V_2}{X} \delta \tag{B.22}$$

$$Q \approx \frac{V_1^2}{X} - \frac{V_1 V_2}{X} \tag{B.23}$$

where for lines $X \gg R$ with small power angle δ and small voltage difference $V_1 - V_2$, the power angle δ depends mainly on active power P and voltage difference $V_1 - V_2$ depends mainly on reactive power Q. The control of frequency f dynamically controls the power angle δ and consequently also the active power P or, in other words, the control of active power P directly controls the power angle δ and thus the frequency f. While the control of reactive power Q directly controls the voltage V [19], [21].

By adjusting P and Q independently, frequency and amplitude of the grid voltage are determined. These conclusions form the basis for the well-known frequency and voltage droop regulation through respectively active and reactive power

$$f - f_0 = -k_p (P - P_0) \tag{B.24}$$

$$V_1 - V_o = -k_q (Q - Q_0) \tag{B.25}$$

f_0 and V_0 are rated frequency and grid voltage respectively, P_0 and Q_0 are the (momentary) set points for active and reactive power.

In this work, R is not neglected to accomplish employment in low voltage cable grids or microgrids, generally having a mainly resistive line impedance altering equations (B.22) and (B.23) as [22]

$$P' = \frac{V_1 \; V_2}{Z} \sin(\delta) \tag{B.26}$$

$$Q' = \frac{V_1^2}{Z} - \frac{V_1 V_2}{Z} \cos(\delta) \tag{B.27}$$

For a small power angle δ and voltage difference $V_1 - V_2$, (B.26) and (B.27) show that the power angle depends only on P', In other words, the angle δ can be controlled by regulating P', specifically attaining control over the load in the distribution level. To derive P' and Q', it suffices to know the ratio R/X [22].

APPENDIX C

DISTRIBUTION NETWORK COMPONENTS MODELING

Modeling is defined as a description of a system using mathematical concepts and languages. Mathematical models are used in the natural sciences, engineering disciplines, as well as in social sciences. A model helps to explain a system and to study the effects of different components, and to make predictions about behavior.

Mathematical models can take many forms, including dynamical systems, statistical models, differential equations, or game theoretic models. These and other types of models can overlap, with a given model involving a variety of abstract structures. In general, mathematical models may include logical models. In many cases, the quality of a scientific field depends on how well the mathematical models developed on the theoretical side agree with results of repeatable experiments. Lack of agreement between theoretical mathematical models and experimental measurements often leads to important advances as better theories are developed.

Mathematical models are usually composed of relationships and variables. Relationships can be described by operators, such as algebraic operators, functions, differential operators, etc. Variables are abstractions of system parameters of interest that can be quantified. Several classification criteria can be used for mathematical models according to their structure: Linear vs. nonlinear, Static vs. dynamic, Explicit vs. implicit, Discrete vs. continuous, Deterministic vs. probabilistic (stochastic) and Deductive, inductive, or floating. In this work the following can be found [2]

- Static vs. dynamic: A dynamic model accounts for time-dependent changes in the state of the system, while a static (or steady-state) model calculates the system in equilibrium, and thus is time-invariant. Dynamic models typically are represented by differential equations or difference equations.
- Discrete vs. continuous: A discrete model treats objects as discrete, such as the particles in a molecular model or the states in a statistical model; while a continuous model represents the objects in a continuous manner, such as the velocity field of fluid in pipe flows, temperatures and stresses in a solid, and electric field that applies continuously over the entire model due to a point charge.
- Deterministic vs. probabilistic (stochastic): A deterministic model is one in which every set of variable states is uniquely determined by parameters in the model and by sets of previous states of these variables; therefore, a deterministic model always performs the same way for a given set of initial conditions. Conversely, in a stochastic model randomness is present, usually called a "statistical model", and variable states are not described by unique values, but rather by probability distributions.

This chapter describes the different models implemented to develop the multiphase power flow program; the modeling of the elements required in a distribution network in single- to multi-phase

for overhead lines and underground cables, transformers, the power flow algorithm employed, and finally the validation of the base program.

C.1 Overhead line

C.1.1 Parameters and characteristics

Overhead line has four parameters which affect its behavior. These parameters are resistance, inductance, capacitance, and conductance. Fig. C.1 shows an open two-wire line and it is associated magnetic and electric fields. The lines of magnetic flux form closed loops linking the circuit, and the lines of the electric flux originate on the positive charges on one conductor and terminate on the negative charges on the other conductor. Variation of the current in the conductors causes a change in the number of lines of magnetic flux linking the circuit. Any change in the flux linking a circuit induces a voltage in the circuit, and the induced voltage is proportional to the rate of change of flux. Inductance is the property of the circuit that relates the voltage induced by changing flux to the rate of change of current [3].
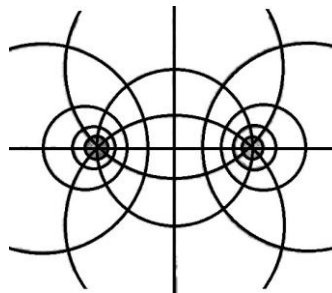
Fig. C.1. Magnetic and electric fields associated with a two-wire line.

The potential difference between the conductors of a line causes the conductors to be charged on the same manner as the plates of a capacitor are charged when there is a potential difference between the plates of the capacitor. The capacitance between conductors is the charge per unit of potential difference. Capacitance is a constant depending on the size and spacing of the conductors. For power lines less than about 50 mi (80.47 km) long, the effect of capacitance is slight and is usually neglected [3]. The conductance is usually ignored because it is very small compared to the capacitive susceptance [4].

The series impedance of a distribution line consists of the resistance of the conductors and the self and mutual inductive reactances resulting from the magnetic fields surrounding the conductors. The shunt admittance of a line consists of the conductance and the capacitive susceptance.

There are different conductor types with their own characteristics as seen in Table C.1, which has some of the conductors data from the datasheet. The conductors are made with materials as:

- AA: All aluminum

- ACSR: aluminum conductor steel reinforced

- CU: Copper

- Steel

<div align="center">Table C.1. Conductor Data</div>

Conductor size	Material	Resistance f=60 50°C (Ω/mile)	Diameter (inches)	GMR (Feet)	Ampacity at 50°C
1	AA	0.105	1.15	0.0368	698
556.5	ACSR	0.14859	0.927	0.0313	730
500	AA	0.206	0.813	0.026	483
336.4	ACSR	0.306	0.721	0.0244	530
250	AA	0.41	0.567	0.0171	329
# 4/0	ACSR	0.592	0.563	0.00814	340
# 2/0	AA	0.769	0.414	0.0125	230
# 1/0	ACSR	1.12	0.398	0.00446	230
# 1/0	AA	0.97	0.36	8 0.0111	310
# 2	AA	1.54	0.292	0.00883	156
# 2	ACSR	1.69	0.316	0.00418	180
# 4	ACSR	2.55	0.257	0.00452	140
# 10	CU	5.903	0.102	0.00331	80
# 12	CU	9.375	0.081	0.00262	75
# 14	CU	14.872	0.064	0.00208	20

The AA conductors have greater tension force than ordinary aluminum conductors. The ACSR is a type of high-capacity, high-strength stranded conductor, The outer strands are high purity aluminum and the center strand, or strands is/are of steel for additional strength to help support the weight of the conductor.

The spacing ID numbers and type for overhead lines are summarized in Table C.2.

<div align="center">Table C.2. Overhead Line Spacings ID</div>

Spacing ID	Type
500	Three-Phase, 4 wire
505	Two-Phase, 3 wire
510	Single-Phase, 2 wire

Fig. C.2 shows the spacing distances between the phase conductors and the neutral conductor in feet for spacing ID numbers for overhead lines [5].
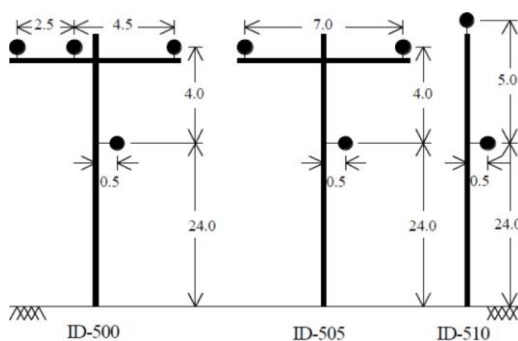
Fig. C.2. Overhead Line Spacings.

C.1.2 Modeling an overhead line

The series impedance is a basic step before the analysis of a distribution network. To accomplish the overhead line model, first the series impedance was computed by means of the Carson's method, and second the shunt admittance was calculated.

The Carson's method was the algorithm incorporated to calculate the impedances and admittances matrix of the line as explained in the following chapters. This method takes into account a penetration depth, which assumes that return currents are concentrated in a fictional plane beneath the surface of the Earth [4], [6]–[9].

The series impedance of a single-phase, two-phase or three-phase distribution line consists of the resistance of the conductors and the self and mutual inductive reactances resulting from the magnetic fields surrounding the conductors. The resistance and inductance uniformly distributed along the line form the series impedance. The resistance component will come from the conductor data as found in Table C.1.

The inductance is a function of the total magnetic fields surrounding a conductor as shown in Fig. C.1. The currents in all conductors are assumed to be flowing out of the page. That is $I_1 + I_2 + \ldots + I_n = 0$.

The total flux linking conductor i is

$$\lambda_i = 2 \cdot 10^{-7} \left(I_1 \ln\left(\frac{1}{D_{i1}}\right) + I_2 \ln\left(\frac{1}{D_{i2}}\right) + \ldots + I_i \ln\left(\frac{1}{GMR_i}\right) + \ldots + I_n \ln\left(\frac{1}{D_{in}}\right) \right) \ \text{[Wb-t/m]} \qquad \text{(C.1)}$$

where D_{in} is the distance between conductors i and n in meters and GMR_i represents the geometric mean radius of conductor i in meters.

The inductance of conductor i consists in the self-inductance of conductor i and the mutual inductance between conductor i and all the other conductors, given by

Self-inductance: $\qquad\qquad L_{ii} = \frac{\lambda_{ii}}{I_i} = 2 \cdot 10^{-7} \ln\frac{1}{GMR_i} \qquad \text{[H/m]} \qquad \text{(C.2a)}$

Mutual inductance: $\qquad\qquad L_{in} = \frac{\lambda_{in}}{I_n} = 2 \cdot 10^{-7} \ln\frac{1}{D_{in}} \qquad \text{[H/m]}. \qquad \text{(C.2b)}$

Distribution systems consist of single-phase, two-phase, and untransposed three-phase lines serving unbalanced loads, it is necessary to identify the self and mutual impedance of the conductors [4] and take into account the ground return path for the unbalanced currents [5].

As aforementioned, the impedance is computed by means of the Carson's method [9]

$$Z_s = R_k + jw\frac{\mu_0}{2\pi}\left[\ln\frac{2h}{r} + \int_0^\infty \frac{2e^{-2h\lambda}}{\lambda+\sqrt{\lambda^2+jw\mu_0\sigma}}d\lambda\right] \qquad \text{(C.3)}$$

$$Z_m = jw\frac{\mu_0}{2\pi}\left[\ln\frac{\sqrt{d_{kl}^2+(h_k+h_l)^2}}{\sqrt{d_{kl}^2+(h_k-h_l)^2}} + \int_0^\infty \frac{2e^{-(h_k+h_l)\lambda}}{\lambda+\sqrt{\lambda^2+jw\mu_0\sigma}}\cos\lambda\ d_{kl}d\lambda\right] \qquad \text{(C.4)}$$

where Z_s is the series impedance, Z_m represents the mutual impedance, R_k is the conductor resistance in Ω/m, h_k is the height of the k-th conductor above ground in meters, r_k is the radius of the k-th conductor in meters which is the GMR_k, d_{kl} is the horizontal distance between the k-th and the l-th conductors in meters, ω is equal to $2\pi f$ where f is the frequency in Hz, σ is the earth conductivity in Siemens and μ_0 represents the absolute permeability equivalent to $4\pi \cdot 10^{-7}$ in H/m.

Taking into account just the first terms of the infinite series

$$Z_s = R_k + \pi^2 f \cdot 10^{-4} + j2w10^{-4} \ln\frac{D_e}{r_k} \qquad [\Omega/m] \qquad (C.5)$$

$$Z_m = \pi^2 f \cdot 10^{-4} + j2w10^{-4} \ln\frac{D_e}{D_{kl}} \qquad [\Omega/km] \qquad (C.6)$$

where D_e is an equivalent depth of the fictitious return path of the earth current

$$D_e = 659\sqrt{\frac{\rho}{f}} \qquad [m] \qquad (C.7)$$

ρ is equal to $1/\sigma$ in $[\Omega \cdot m]$. This expression is not valid for higher frequencies than 60Hz [9]. Carson made use of conductor images and the distances between them, as in Fig. C.3; every conductor at a given distance above ground has an image conductor the same distance below ground.
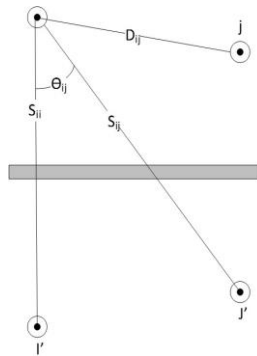
Fig. C.3. Conductors and images.

The formulas are based, assuming that return currents are concentrated in a fictional plane p, beneath the surface of the Earth as shown in Fig. C.4 [9].
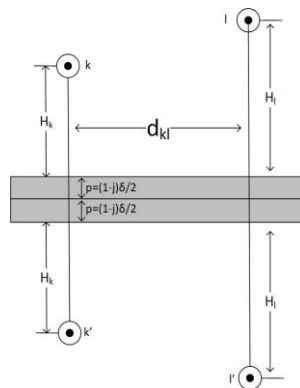
Fig. C.4. Complex penetration depth, as mirroring surface for conductor images.

$$p = (1-j)\frac{\delta}{2} = \frac{1}{\sqrt{jw\mu_0\sigma}} \tag{C.8}$$

in which δ is the penetration depth in meters.

The impedance calculations are performed by considering the distances of the images of the conductors, whereby the self and mutual impedance of the overhead line is obtained

$$Z_s = R_k + jw\frac{\mu_0}{2\pi}\ln\frac{2(h_k+p)}{r_k} \tag{C.9}$$

$$Z_m = jw\frac{\mu_0}{2\pi}\ln\frac{\sqrt{d_{kl}^2+(h_k+h_l+2p)^2}}{\sqrt{d_{kl}^2+(h_k-h_l)^2}} \tag{C.10}$$

the spaces are calculated considering Fig. C.4 [9].

The shunt admittance consists in the capacitive susceptance and conductance, the conductance is generally ignored because it is too small compared to the capacitive susceptance, as above-mentioned.

Considering that a charged conductor creates an electric field that emanates outward from the center, lines of equipotential are created that are concentric to the charged conductor. When the potential difference between two points is known, the capacitance between the two points can be computed. In case there is another charged conductors nearby, the potential between the two points will be a function of the distance to the other conductors and the charge on each conductor [4].

From Fig. C.4, the voltage drop between conductors i and j as a result of all the charged conductors is given by

$$V_{ij} = \frac{1}{2\pi\epsilon}(q_1\ln\frac{D_{ij}}{D_{1i}} + \cdots + q_i\ln\frac{D_{ij}}{RD_i} + \cdots + q_j\ln\frac{RD_j}{D_{ij}} + \cdots + q_N\ln\frac{D_{Nj}}{D_{Ni}}) \tag{C.11}$$

and in a general way is

$$V_{ij} = \frac{1}{2\pi\epsilon}\sum_{n=1}^{N}q_n\ln\frac{D_{nj}}{D_{ni}} \tag{C.12}$$

 is equal to $\epsilon_0\epsilon_r$ and represents the permittivity, ϵ_0 is the permittivity of free space (8.85x10^{-12} [μF/m]), ϵ_r represents the relative permittivity of the medium, q_n is the charge density on conductor n in cb/m, D_{ni} is the distance between conductors n and i in meters, D_{nj} is the distance between conductors n and j in meters, and RD_n is the radius of conductor n in meters.

In Fig. C.3 it is assumed that $q_i^0 = -q_i$ and $q_j^0 = -q_j$. Considering (C.12), the voltage drop between i and ground (V_{ig}) is given by

$$V_{ig} = \frac{1}{2\pi\epsilon}\left(q_i\ln\frac{S_{ii}}{RD_i} + q_j\ln\frac{S_{ij}}{D_{ij}}\right) \tag{C.13}$$

which can be expressed in a general form as

$$V_{ig} = \hat{P}_{ii}q_i + \hat{P}_{ij}q_j \tag{C.14}$$

where $\hat{P}_{ii}$ and $\hat{P}_{ij}$ are the self and mutual potential coefficients. From (C.13) and (C.14) it can be deduced

$$\hat{P}_{ii} = \frac{1}{2\pi\epsilon} \ln \frac{S_{ii}}{RD_i} \qquad [m/\mu F] \tag{C.15}$$

$$\hat{P}_{ij} = \frac{1}{2\pi\epsilon} \ln \frac{S_{ij}}{D_{ij}} \qquad [m/\mu F] \tag{C.16}$$

all the distances S_{ii}, S_{ij}, RD_i, and D_{ij} must be in the same units, in this case in meters.

For *n* conductors the primitive potential coefficient matrix will be

$$[\hat{P}_{primitiva}] = \begin{bmatrix} \hat{P}_{aa} & \hat{P}_{ab} & \hat{P}_{ac} & \cdot & \hat{P}_{an} \\ \hat{P}_{ba} & \hat{P}_{bb} & \hat{P}_{bc} & \cdot & \hat{P}_{bn} \\ \hat{P}_{ca} & \hat{P}_{cb} & \hat{P}_{cc} & \cdot & \hat{P}_{cn} \\ \cdot & \cdot & \cdot & \cdot & \cdot \\ \hat{P}_{na} & \hat{P}_{nb} & \hat{P}_{nc} & \cdot & \hat{P}_{nn} \end{bmatrix} \tag{C.17}$$

by adjusting the potential coefficient matrix in partitioned form, it becomes

$$[\hat{P}_{primitiva}] = \begin{bmatrix} [\hat{P}_{ij}] & [\hat{P}_{in}] \\ [\hat{P}_{nj}] & [\hat{P}_{nn}] \end{bmatrix} \tag{C.18}$$

because the neutral conductor is grounded, the matrix may be reduced by using Kron reduction, thus obtaining the phase potential coefficient; therefore the capacitance can be calculated

$$[P_{abc}] = [\hat{P}_{ij}] - [\hat{P}_{in}] \cdot [\hat{P}_{nn}]^{-1} \cdot [\hat{P}_{nj}] \quad \text{and} \quad [C_{abc}] = [\hat{P}_{abc}]^{-1} \tag{C.19}$$

and subsequently the shunt admittance is computed as

$$[Y_{shunt}] = jw \cdot [C_{abc}] \qquad [\mu S/m]. \tag{C.20}$$

With the series impedance and shunt admittance, the overhead line model can be computed considering Fig. 4.2 [8], [10]. To compute the impedance and admittance between lines, the series impedance matrix is inverted to compute the series admittance Y_{series}. The bus admittance matrix of a network is expressed as

$$Y_{bus} = N_{in}^T Y_{series} N_{in} \tag{C.21}$$

where N_{in} is the incidence matrix, which in case of three conductors is.

$$N_{in} = \begin{bmatrix} 1 & 0 & 0 & -1 & 0 & 0 \\ 0 & 1 & 0 & 0 & -1 & 0 \\ 0 & 0 & 1 & 0 & 0 & -1 \end{bmatrix} \qquad (C.22)$$

the rows represent each conductor and the columns are the beginning and the ending connection point per conductor, from sending (1) nodes 'A','B' and 'C' to receiving (−1) nodes 'a', 'b', and 'c' from Fig. 4.2. This model results in a matrix with the fictitious lines that represent the admittances between lines [8].

Once the three-phase model is calculated, the two-phase and single-phase model can be obtained with the same analysis from the three-phase line with the difference that the Y_{series} will have a size of 2x2 and a single element. These matrices can be expanded to 3x3 phase frame matrices by the addition of rows and columns consisting of zero elements for the mission phases [4]. For example a two-phase line consisting of phases 'a' and 'c', and a single-phase consisting in phase 'b' would be

$$Y_{bus} = \begin{bmatrix} Y_{aa} & Y_{ac} \\ Y_{ca} & Y_{cc} \end{bmatrix} \qquad Y_{bus} = \begin{bmatrix} Y_{aa} & 0 & Y_{ac} \\ 0 & 0 & 0 \\ Y_{ca} & 0 & Y_{cc} \end{bmatrix} \qquad Y_{bus} = \begin{bmatrix} 0 & 0 & 0 \\ 0 & Y_{bb} & 0 \\ 0 & 0 & 0 \end{bmatrix}. \qquad (C.23)$$

The obtained Y_{bus} is implemented in the power flow analysis program for distribution networks, being that Y_{bus} represents a three-phase overhead line. The data from the Y_{bus} matrix will interact with the power balance equations in the power flow program.

C.2 Underground line

The underground distribution is hidden from view compared to overhead routes. Underground circuits are applied in a distribution network, i.e. for underground residential distribution (URD); underground branches or loops supplying residential neighborhoods and utilities also used in underground construction for substation exits to pad-mounted transformers serving industrial or commercial customers, river crossings, among other uses [7]. The cables typically implemented in the distribution network are concentric neutral cable and tape-shielded cable.

The typical construction of a concentric neutral cable is shown in Fig. C.5. At the center of a cable is the phase conductor, then comes a semiconducting conductor shield, the insulation, a semiconducting insulation shield, the neutral or shield, and finally a covering jacket. Most distribution cables are single conductor. Two main types of cable are available: concentric neutral cable and power cable. Concentric-neutral cable normally has an aluminum conductor, an extruded insulation, and a concentric neutral. A concentric neutral is made from several copper wires wound concentrically around the insulation; the concentric neutral is a true neutral, meaning it can carry return current on a grounded system. Underground residential distribution normally has concentric neutral cables; concentric neutral cables are also used for three-phase mainline applications and three-phase power delivery to commercial and industrial customers. Because of their widespread use in URD, concentric neutral cables are often called URD cables [7].
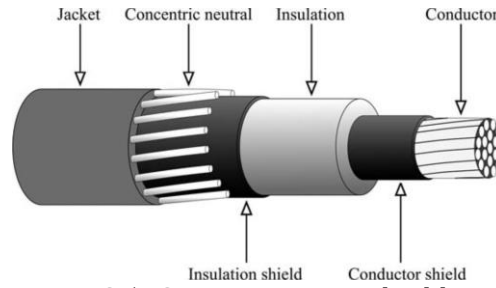
Fig. C.5. Concentric neutral cable.

Tape-shielded cable has a copper or aluminum phase conductor, an extruded insulation, and normally a thin copper tape shield. On utility distribution circuits, power cables are typically used for mainline feeder applications, network feeders, and other high current, three-phase applications. Many other types of medium-voltage cable are available. These are sometimes appropriate for distribution circuit application: three-conductor power cables, armored cables, aerial cables, fire-resistant cables, extra flexible cables, and submarine cables [4], [7].

Normal construction is a three-phase cable where separately insulated phase conductors are covered with a common screen and insulation. For applications where the load current demands are high, the use of single-phase cables becomes more convenient. If cables must run in places where exposed to impact damage, they are protected with flexible steel tape or wire armor, which may also be covered by a water-resistant jacket [11], [12].

The general configuration of three underground cables, concentric neutral or tape shield with additional neutral conductor, is shown in Fig. C.6.
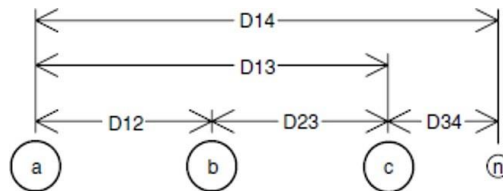
Fig. C.6. Three-phase underground with additional neutral.

C.2.1 Concentric neutral cable model

The cable consists of a central phase conductor covered by a thin layer of non-metallic semiconducting screen, to which is bonded the insulating material. The insulation is then covered by a semiconducting insulation screen as shown in Fig. C.7. The solid strands of concentric neutral are spiraled around the semiconducting screen with a uniform spacing between strands. Some cables will also have an insulating jacket encircling the neutral strands.
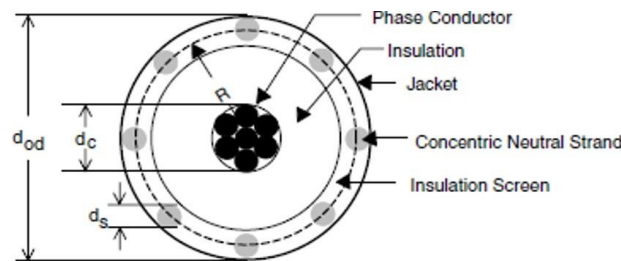
Fig. C.7. Concentric neutral cable.

For the series impedance, the modified Carson's equations were implemented in the same manner as was done with the overhead line. One must have information on the characteristics of the type of cable, such as GMR, resistance, phase conductor and neutral. There are different types of drivers classified by size characteristics, which can be found on the standardized datasheets. In order to compute the capacitance between the phase conductor and the ground to calculate the admittance matrix, the general voltage drop equation was implemented [3], [4], [7].

To calculate the cable impedance and admittance, the data needed are: phase conductor diameter (d_c), the nominal diameter over the concentric neutrals of the cable (d_{od}), the diameter of a concentric neutral strand (d_s), the GMR of the phase conductor (GMR_c), the GMR of the neutral strand (GMR_s), the resistance of the phase conductor (r_c), the resistance of a solid neutral strand (r_s), the number of concentric neutral strands (k_s), and the radius of a circle passing through the centers of the neutral strands (R_b), as observed in Table C.3.

In the case of concentric neutral cable, the datasheet provides the diameters required for series impedance calculation (C.3), and the GMR concentric neutral is calculated while considering the number of neutral strands

Table C.3. Concentric Neutral 15 kV Cable Conductor

Conductor size	Diameter over insulation (inches)	Diameter over screen (inches)	Outside Diameter (inches)	Copper neutral N° AWG	Ampacity at 50°C
Full neutral					
2(7x)	0.78	0.85	0.98	10 x 14	120
1(19x)	0.81	0.89	1.02	13 x 14	135
1/0(19x)	0.85	0.93	1.06	16 x 14	155
2/0(19x)	0.90	0.97	1.13	13 x 12	175
3/0(19x)	0.95	1.02	1.18	16 x 12	200
4/0(19x)	1.01	1.08	1.28	13 x 10	230
250(37x)	1.06	1.16	1.37	16 x 10	255
350(37x)	1.17	1.27	1.47	20 x 10	300
1/3 Neutro					
2(7x)	0.78	0.85	0.98	6 x 14	135
1(19x)	0.81	0.89	1.02	6 x 14	155
1/0(19x)	0.85	0.93	1.06	6 x 14	175
2/0(19x)	0.90	0.97	1.10	7 x 14	200
3/0(19x)	0.95	1.02	1.15	9 x 14	230
4/0(19x)	1.01	1.08	1.21	11 x 14	240
250(37x)	1.06	1.16	1.29	13 x 14	260
350(37x)	1.17	1.27	1.39	18 x 14	320
500(37x)	1.29	1.39	1.56	16 x 12	385
750(61x)	1.49	1.59	1.79	15 x 10	470
1000(61x)	1.64	1.77	1.98	20 x 10	550

$$GMR_{cn} = \sqrt[k_s]{GMR_s \cdot k_s \cdot R_c^{k_s-1}} \qquad R_c = \frac{d_{od}-d_s}{2} \, [m] \qquad r_{cn} = \frac{r_s}{k_s} \, [\Omega/m] \qquad \text{(C.24)}$$

in case of the conductor, Table C.3 has the required information.

The spacings between a concentric neutral and the phase conductors and other concentric neutrals are:

- Concentric neutral to its own phase conductor: $D_{ij} = R_c$ considering (C.24).

- Concentric neutral to an adjacent concentric neutral: D_{ij} = center-to-center distance of the phase conductors.

- Concentric neutral to an adjacent phase conductor:

$$D_{ij} = \sqrt[k_s]{D_{nm}^{k_s} - R_c^{k_s}}$$
(C.25)

where D_{nm} =center-to-center distance between phase conductors. For cables buried in a trench the distance between cables will be much greater than the radius R_c, and it may be assumed that D_{ij} from (C.25) is equal to D_{nm}. For cables in conduit that assumption is not valid [4].

The Carson's equation is then implemented to calculate the series impedance

$$z_{ii} = r_i + 0.0953 + j0.12134 \cdot \left[\ln\frac{1}{GMR_i} + 7.93402\right]$$
(C.26)

$$z_{ij} = 0.0953 + j0.12134 \cdot \left[\ln\frac{1}{D_{ij}} + 7.93402\right].$$
(C.27)

The shunt admittance for the concentric neutral cable is estimated similar to an overhead line, considering the characteristic and parameters like in the Fig. C.8.

The neutral cables are grounded so they have the same potential, and the potential drop difference between the conductor p and the *strand1* is determined by

$$V_{p1} = \frac{1}{2\pi\epsilon}\left(q_p \ln\frac{R_b}{RD_c} + q_1 \ln\frac{RD_s}{R_b} + q_2 \ln\frac{D_{12}}{R_b} + \cdots + q_i \ln\frac{D_{1i}}{R_b} + \cdots + q_k \ln\frac{D_{k1}}{R_b}\right)$$
(C.28)

where $RD_c = 0.5d_c$ and $RD_s = 0.5d_s$. It is assumed that each neutral strand carries the same charge as
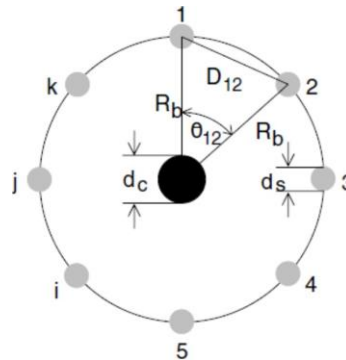
Fig. C.8. Concentric neutral cable parameters.

109

$$q_1 = q_2 = q_i = -\frac{q_p}{k}. \tag{C.29}$$

therefore (C.28) can be simplified to

$$V_{p1} = \frac{1}{2\pi\epsilon}\left[q_p \ln \frac{R_b}{R_c D_c} - \frac{q_p}{k_s}\left(\ln \frac{RD_s}{R_b} + \ln \frac{D_{12}}{R_b} + \cdots + \ln \frac{D_{1i}}{R_b} + \cdots + \ln \frac{D_{1k_s}}{R_b}\right)\right] \tag{C.30}$$

$$V_{p1} = \frac{q_p}{2\pi\epsilon}\left[\ln \frac{R_b}{RD_c} - \frac{1}{k_s}\left(\ln \frac{RD_s \cdot D_{12} \cdot D_{1i} \cdots D_{1k_s}}{R_b^{k_s}}\right)\right]. \tag{C.31}$$

the natural logarithms are the distances between line i other strands and the products between radios and distances considering Fig. C.8

$$\theta_{12} = \frac{2\pi}{k_s} \tag{C.32}$$

$$\theta_{13} = 2\theta_{12} = \frac{4\pi}{k_s} \tag{C.33}$$

in general, the angle between *strand 1* and any other *strand i* is given by

$$\theta_{1i} = (i-1)\theta_{12} = \frac{2\pi(i-1)}{k_s} \tag{C.34}$$

and the distances between the strands are

$$D_{12} = 2R_b \sin\left(\frac{\theta_{12}}{2}\right) = 2R_b \sin\left(\frac{\pi}{k_s}\right) \tag{C.35}$$

$$D_{13} = 2R_b \sin\left(\frac{\theta_{13}}{2}\right) = 2R_b \sin\left(\frac{2\pi}{k_s}\right) \tag{C.36}$$

in a general form (C.35) and (C.36) can be written as

$$D_{1i} = 2R_b \sin\left(\frac{\theta_{1i}}{2}\right) = 2R_b \sin\left(\frac{(i-1)\pi}{k_s}\right) \tag{C.37}$$

when the distances are considered in (C.31) it will the reduced as

$$V_{p1} = \frac{q_p}{2\pi\epsilon}\left[\ln \frac{R_b}{RD_c} - \frac{1}{k_s}\left(\ln \frac{k_s RD_s}{R_b}\right)\right] \tag{C.38}$$

therefore, the capacitance from phase to ground for a concentric neutral cable is given by

$$C_{pg} = \frac{q_p}{V_{p1}} = \frac{2\pi\epsilon}{\ln\frac{R_b}{RD_c} - \frac{1}{k_s}\left(\ln\frac{k_s RD_s}{R_b}\right)}. \tag{C.39}$$

The electric field of a cable is confined to the insulation material. Various types of insulation materials are used and each will have a range of values for the relative permittivity that can be seen from Table C.4.

110

Table C.4. Typical values of relative permittivity ϵ_r

Material	Range of values of relative permittivity
Polyvinyl Chloride (PVC)	3.4–8.0
Ethylene-Propylene Rubber (EPR)	2.5–3.5
Polyethylene (PE)	2.5–2.6
Cross-Linked Polyethlyene (XLPE)	2.3–6.0

With capacitance computed the shunt admittance is given by

$$y_{pg} = 0 + j \frac{2\pi\epsilon}{\ln\frac{R_b}{RD_c} - \frac{1}{k_s}\left(\ln\frac{k_s RD_s}{R_b}\right)} \quad [\mu S/mile] \tag{C.40}$$

C.2.2 Tape-shielded cable model

Unlike the concentric neutral cable that has strands, the tape-shielded cable, as its name indicates, has a shield instead of strands. The shield is bare copper tape helically applied around the insulation screen. To calculate the impedance and admittance to this cable, the data needed are: d_c the diameter of phase conductor, the outside diameter of the tape shield d_s, the outside diameter over jacket d_{od}, the thickness of the copper tape shield T_c, and the radius of a circle passing through the center of the tape shield GMR , as shown in Fig. C.9 [4], [13].
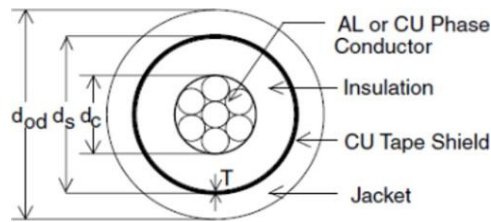
Fig. C.9. Tape-shielded cable internal distances.

The required parameters can be taken from the cable datasheet as in Table C.5.

Table C.5. Tape-shielded 15 kV cable data with 5 mils tape thickness

Conductor size	Diameter over insulation (inches)	Diameter over screen (inches)	Jacket thickness (mils)	Outside diameter (inches)
1/0	0.82	0.88	80	1.06
2/0	0.87	0.93	80	1.10
3/0	0.91	0.97	80	1.16
4/0	0.96	1.02	80	1.21
250	1.01	1.08	80	1.27
350	1.11	1.18	80	1.37
500	1.22	1.30	80	1.49
750	1.40	1.48	110	1.73
1000	1.56	1.66	110	1.91

For the tape-shielded cable, the impedance matrix was computed by applying the modified Carson's equations. In addition, the admittance matrix is calculated in the same way as the concentric neutral cable, with the difference that the number of strands tends to infinite [3], [4], [7].

For the series impedance of the tape-shielded cable, the modified Carson's equations were also applied, with the GMR and resistance of the phase conductor found in the Table C.1. The shield resistance is given by

$$r_{shield} = 7.9385x10^8 \frac{\rho}{d_s T_c} \ [\Omega/\text{mile}] \qquad (C.41)$$

where ρ is the resistivity expressed in ohm per meters at 50°D.

The GMR of the tape shield is the radius of a circle passing through the middle of the shield and is given by

$$GMR_{shield} = \frac{d_s - \frac{T_c}{1000}}{24} \ [\text{ft}]. \qquad (C.42)$$

The various spacings between a tape shield and the conductors and other tape shields are as follows

- Tape shield to its own phase conductor: $D_{ij} = GMR_{shield}$ = radius to midpoint of the shielE.

- Tape shield to an adjacent tape shield: D_{ij} = center-to-center distance of the phase conductors.

- Tape shield to an adjacent phase or neutral conductor: D_{ij} = center-to-center distance between phase conductors.

The shunt admittance is calculated with the same equation for the concentric neutral cable with the difference that now the tape-shielded cable can be viewed as a concentric neutral cable with infinite strands, as in Fig. C.10 [7]; this means that k_s is infinite, and when k_s approaches to infinite, the second term of (C.40) approaches zero

$$y_{ag} = 0 + j \frac{2\pi\epsilon}{\ln\frac{R_b}{RD_c}} \ [\mu S/\text{mile}]. \qquad (C.43)$$

Fig. C.10. Tape-Shielded conductor.

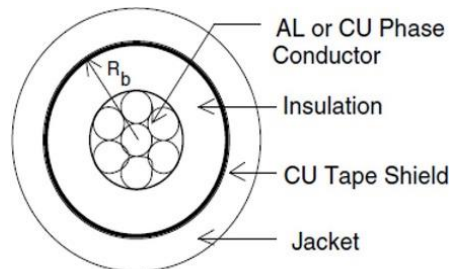## C.3 Transformer model

The power transformer is an essential component of the power system, providing interface between sections of the net with different rating voltages. A distribution transformer or service transformer provides the final voltage transformation in the distribution system, stepping down the voltage used in the distribution lines to the level used by the customer.

Power transformers are used in transmission network of higher voltages for step-up and stepdown application (400 kV, 200 kV, 110 kV, 66 kV, 33 kV) and are generally rated above 200 MVA. Distribution transformers are used for lower voltage distribution networks as a means to end user connectivity (11 kV, 6.6 kV, 3.3 kV, 440 V, 230 V) and are generally rated less than 200 MVA [14].

Distribution transformers are normally located at a service drop, where wires run from a utility pole or underground power lines to a customer's premises [15]. Distribution transformers normally have ratings less than 200 kVA, although some national standards can allow for units up to 5000 kVA to be described as distribution transformers. Since distribution transformers are energized for 24 hours a day (even when they do not carry any load), reducing iron losses has an important role in their design. As they usually do not operate at full load, they are designed to have maximum efficiency at lower loads. To have a better efficiency, voltage regulation in these transformers should be kept to a minimum. Hence they are designed to have small leakage reactance [16].

C.3.1 Single-phase two-winding transformer

The transformer model is developed from a single-phase two-winding transformer, taking into account the conventional equivalent circuit shown in Fig. C.11, where all quantities are in physical units of volts, amps and ohms. $Z_H = R_H + jX_H$, $R_H = HV$ winding resistance, $X_H = HV$ winding leakage reactance. R_1 =resistance representing core iron losses which are assumed to vary with the square of applied HV winding voltage, X_M =core magnetizing reactance referred to the HV side and representing the rms values of the magnetizing current, N_H and N_L are the actual number of turns of HV and LV winding number of turns at nominal tap positions, respectively.

(a)

(b)
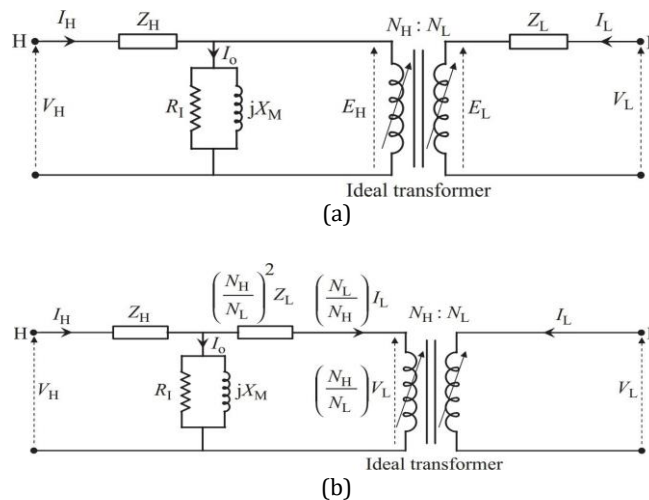
Fig. C.11. Single-phase transformer equivalent circuit in actual physical units: (a) basic equivalent circuit and (b) L winding impedance referred to H winding.

From basic transformer theory and since the same flux will thread both HV and LV windings, the induced voltage per turn on the high-voltage (HV) and low-voltage (LV) windings are equal

$$N_{HL} = \frac{E_H}{E_L} = \frac{N_H}{N_L} \tag{C.44}$$

Initially is neglected the ampere-turns (MMF - magnetomotive force, represented by a direct current of one ampere flowing in a single-turn loop) due to the exciting shunt branch that represents the very small core iron and magnetizing losses. The HV and LV windings MMFs, for the current directions shown in Fig. C.11a are related by

$$N_H I_H + N_L I_L = 0 \quad \text{or} \quad \frac{I_H}{I_L} = -\frac{1}{N_{HL}}. \tag{C.45}$$

The voltage drop equations for the transformer at both windings are

$$V_H - E_H = Z_H I_H \tag{C.46}$$

$$V_L - E_L = Z_L I_L. \tag{C.47}$$

Using (C.44) and (C.46), (C.47) can be written as

$$\frac{1}{N_{HL}}(V_H - Z_H I_H) = V_L - Z_L I_L \tag{C.48}$$

substituting (C.45) into (C.48) is deduced

$$V_H - Z_{HL} I_H = N_{HL} V_L \tag{C.49}$$

where

$$Z_{HL} = Z_H + N_{HL}^2 Z_L \tag{C.50}$$

which is the equivalent transformer leakage impedance referred to the HV side and $N_{HL}^2 Z_L$ is the LV impedance referred to the HV side. Fig. C.11b is drawn using (C.49) [17].

Normally the data nameplate of a transformer contains at least the rated power in VA ($kV\,A$), the rated frequency in Hz, the rated voltages on sides HV (E_H) and LV (E_L), the rated currents on both sides, the number of phases, the percentage of impedance (RT) and reactance (XT), the temperature, the year manufacture, the manufacturer's name and the serial number.

with the percent of resistance and reactance from the nominal data of the transformer, the primary and secondary nominal base impedance can be calculated by

$$Zb_H = \frac{E_H^2}{kV\,A} \tag{C.51}$$

$$Zb_L = \frac{E_L^2}{kV\,A} \tag{C.52}$$

taking into account the base impedance, the impedance of the transformer is deduced

$$Z_H = Zb_H \frac{RT + XT \cdot 1i}{100} \qquad (C.53)$$

$$Z_L = Zb_L \frac{RT + XT \cdot 1i}{100} \qquad (C.54)$$

the impedances are then converted to per unit (p.u.) with the base impedance used on network as follows

$$Z_{Hpu} = \frac{Z_H}{Z_{base}} \qquad (C.55)$$

$$Z_{Lpu} = \frac{Z_L}{Z_{base}} \qquad (C.56)$$

(a)

(b)
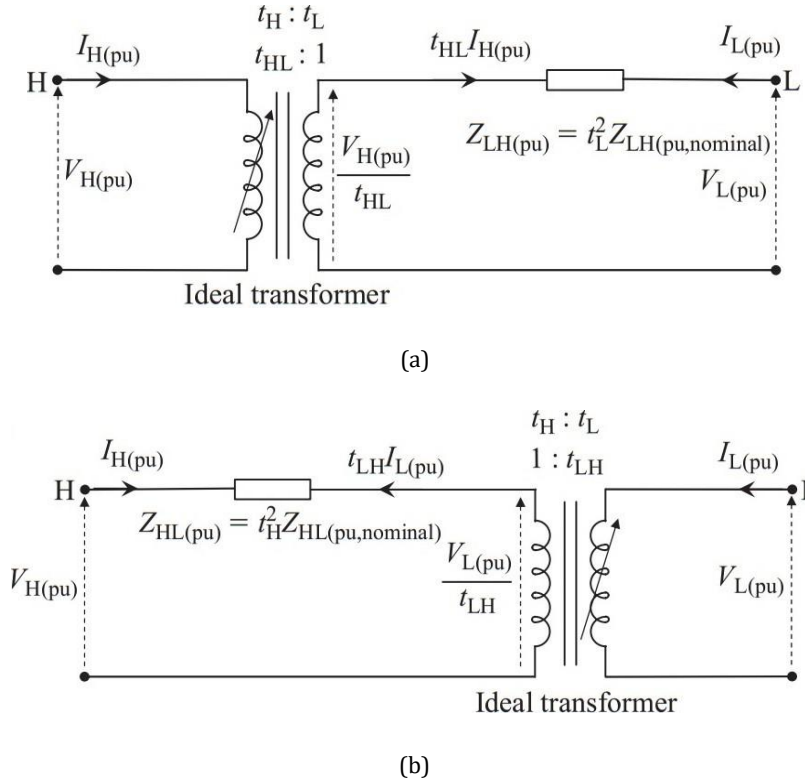
Fig. C.12. Transformer equivalent circuits in p.u. (a) p.u. equivalent circuit with H side off-nominal ratio (b) p.u. equivalent circuit with L side off-nominal ratio.

Applying Kirchhoff's voltage law (KVL) to the circuit of Fig. C.12a and remembering that all values are in per unit, it can be said that

$$I_L = \frac{V_L - \left(\frac{V_H}{t_{HL}}\right)}{Z_{LH}} \qquad (C.57)$$

where

$$-t_{HL} = \frac{I_L}{I_H} \tag{C.58}$$

comparing (C.58) with (C.45), it can be said that t_{HL} is the same N_{HL} with the difference that t_{HL} is given in per unit. Expressing (C.57) in terms of I_H it will be

$$I_H = \frac{V_H}{t_{HL}^2 Z_{LH}} - \frac{V_L}{t_{HL} Z_{LH}} \tag{C.59}$$

been in matrix form

$$\begin{bmatrix} I_H \\ I_L \end{bmatrix} = \begin{bmatrix} \dfrac{1}{t_{HL}^2 Z_{LH}} & -\dfrac{1}{t_{HL} Z_{LH}} \\ -\dfrac{1}{t_{HL} Z_{LH}} & \dfrac{1}{Z_{LH}} \end{bmatrix} \begin{bmatrix} V_H \\ V_L \end{bmatrix} \tag{C.60}$$

and for the circuit in Fig. C.12b expressed as

$$\begin{bmatrix} I_H \\ I_L \end{bmatrix} = \begin{bmatrix} \dfrac{1}{Z_{LH}} & -\dfrac{1}{t_{LH} Z_{HL}} \\ -\dfrac{1}{t_{LH} Z_{HL}} & \dfrac{1}{t_{LH}^2 Z_{HL}} \end{bmatrix} \begin{bmatrix} V_H \\ V_L \end{bmatrix} \tag{C.61}$$

t_{LH} : 1 is the tap ratio [17], [18]. (C.61) can be rewritten as

$$\begin{bmatrix} I_p \\ I_s \end{bmatrix} = \begin{bmatrix} Y_p & Y_m \\ Y_m & Y_s \end{bmatrix} \begin{bmatrix} V_p \\ V_s \end{bmatrix} \tag{C.62}$$

where Y_p and Y_s are the self-admittance for primary and secondary windings respectively, and Y_m is the mutual admittance.

C.3.2 Three-phase transformer model

The multiphase transformers can be derived based on nodal analysis [18]. Fig. C.13 describes a 12-terminal coupled primitive network used later for deducing the matrix of primitive parameters.
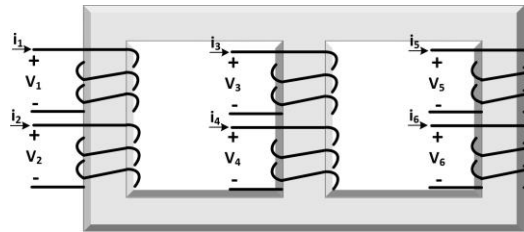
Fig. C.13. 12-terminal coupled primitive network.

The short-circuit primitive parameters of the three identical single-phase transformer shown in Fig. C.11 is

$$\begin{bmatrix} i_1 \\ i_2 \\ i_3 \\ i_4 \\ i_5 \\ i_6 \end{bmatrix} = \begin{bmatrix} Y_{11} & Y_{12} & Y_{13} & Y_{14} & Y_{15} & Y_{16} \\ Y_{21} & Y_{22} & \cdot & \cdot & \cdot & Y_{26} \\ Y_{31} & \cdot & Y_{33} & \cdot & \cdot & \cdot \\ Y_{41} & \cdot & \cdot & \cdot & \cdot & \cdot \\ Y_{51} & \cdot & \cdot & \cdot & \cdot & \cdot \\ Y_{61} & Y_{62} & \cdot & \cdot & \cdot & Y_{66} \end{bmatrix} \begin{bmatrix} V_1 \\ V_2 \\ V_3 \\ V_4 \\ V_5 \\ V_6 \end{bmatrix} \qquad \text{where} \quad Y_{ki} = \frac{i_k}{v_i}$$

$$(C.62)$$

The coils 1, 3 and 5 are considered primary windings and coils 2, 4 and 6 are considered secondary windings.

The circuit from Fig. C.13 does not have the connections presented in a three-phase transformer. The primitive parameters of three identical single-phase transformers with no connection in terminals is

$$\begin{bmatrix} i_1 \\ i_2 \\ i_3 \\ i_4 \\ i_5 \\ i_6 \end{bmatrix} = \begin{bmatrix} Y_p & -Y_m & 0 & 0 & 0 & 0 \\ -Y_m & Y_s & 0 & 0 & 0 & 0 \\ 0 & 0 & Y_p & -Y_m & 0 & 0 \\ 0 & 0 & -Y_m & Y_s & 0 & 0 \\ 0 & 0 & 0 & 0 & Y_p & -Y_m \\ 0 & 0 & 0 & 0 & -Y_m & Y_s \end{bmatrix} \begin{bmatrix} V_1 \\ V_2 \\ V_3 \\ V_4 \\ V_5 \\ V_6 \end{bmatrix} \qquad (C.64)$$

represented in the form $I_k = Y_{prim} V_k$.

A terminal pairs of a three-phase transformer have different connections found like star-star, delta-delta, star-delta and delta-star. The connection of the transformer has to be contemplated when deducing the nodal admittance matrix (Y_{nodal}), with this purpose a matrix connection C and Y_{nodal} can be deduced as

$$Y_{nodal} = C' Y_{prim} C. \qquad (C.65)$$

The matrix connection of the delta-delta transformer shown in Fig. C.14, given in the form $V_k = C_{kL} V_L$, is

Fig. C.14. Delta-delta connection.

$$\begin{bmatrix} V_1 \\ V_2 \\ V_3 \\ V_4 \\ V_5 \\ V_6 \end{bmatrix} = \begin{bmatrix} 1 & -1 & 0 & 0 & 0 & 0 \\ 0 & 0 & 0 & 1 & -1 & 0 \\ 0 & 0 & -1 & 0 & 0 & 0 \\ 0 & 0 & 0 & 0 & 1 & -1 \\ -1 & 0 & 1 & 0 & 0 & 0 \\ 0 & 0 & 0 & -1 & 0 & 1 \end{bmatrix} \begin{bmatrix} V_A \\ V_B \\ V_C \\ V_a \\ V_b \\ V_c \end{bmatrix} \tag{C.66}$$
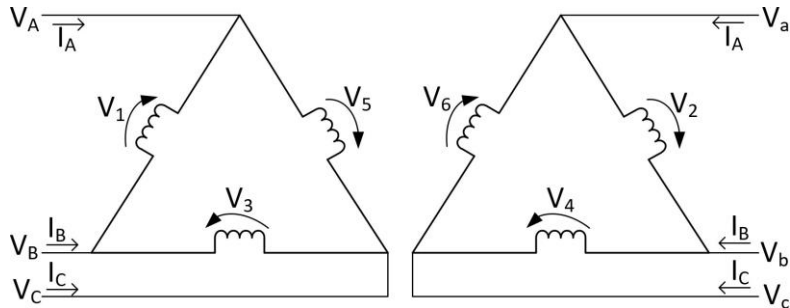
taking into account the existing relationships in the delta connection between voltages and currents in the connected and unconnected circuits $V_k = \frac{1}{\sqrt{3}} C_{kL} V_L$, $\sqrt{3} I_L = C_{Lk} I_k$ [6], and applying (C.65), the resulting nodal admittance matrix is computed as

$$\begin{bmatrix} I_A \\ I_B \\ I_C \\ I_a \\ I_b \\ I_c \end{bmatrix} = \frac{1}{3} \begin{bmatrix} 2Y_p & -Y_p & -Y_p & -2Y_m & Y_m & Y_m \\ -Y_p & 2Y_p & -Y_p & Y_m & -2Y_m & Y_m \\ -Y_p & -Y_p & 2Y_p & Y_m & Y_m & -2Y_m \\ -2Y_m & Y_m & Y_m & 2Y_s & -Y_s & -Y_s \\ Y_m & -2Y_m & Y_m & -Y_s & 2Y_s & -Y_s \\ Y_m & Y_m & -2Y_m & -Y_s & -Y_s & 2Y_s \end{bmatrix} \begin{bmatrix} V_A \\ V_B \\ V_C \\ V_a \\ V_b \\ V_c \end{bmatrix} \tag{C.67}$$

Three-phase transformer admittance matrices

A single three-phase transformer is approximated by three identical single-phase transformer connected appropriately as aforementioned [4], [17], [19]. Based upon this assumption, a characteristic connection matrix exists and by comparing the admittance matrices resulting for each transformer connection, the Table C.6 [10] can be deduced.

Table C.6. Characteristic submatrices used in forming the three-phase transformer admittance matrices

Transformer connection		Self-admittance		Mutual admittance	
Bus p	Bus s	Y_{pp}	Y_{ss}	Y_{ps}	Y_{sp}
Wye-G	Wye-G	Yi	Yi	-Yi	-Yi
Wye-G	Wye	Yii	Yii	-Yii	-Yii
Wye-G	Delta	Yi	Yii	Yiii	$Yiii^T$
Wye	Wye-G	Yii	Yii	-Yii	-Yii
Wye	Wye	Yii	Yii	-Yii	-Yii
Wye	Delta	Yii	Yii	Yiii	$Yiii^T$
Delta	Wye-G	Yii	Yi	$Yiii^T$	Yiii
Delta	Wye	Yii	Yii	$Yiii^T$	Yiii
Delta	Delta	Yii	Yii	-Yii	-Yii

where

$$Y_i = Y_{sc} \begin{bmatrix} 1 & 0 & 0 \\ 0 & 1 & 0 \\ 0 & 0 & 1 \end{bmatrix} \quad Y_{ii} = \frac{Y_{sc}}{3} \begin{bmatrix} 2 & -1 & -1 \\ -1 & 2 & -1 \\ -1 & -1 & 2 \end{bmatrix} \quad Y_{iii} = \frac{Y_{sc}}{\sqrt{3}} \begin{bmatrix} -1 & 1 & 0 \\ 0 & -1 & 1 \\ 1 & 0 & -1 \end{bmatrix} \tag{C.68}$$

moreover, the admittance matrix is expressed as

$$Y_{nodal} = \begin{bmatrix} Y_{pp} & Y_{ps} \\ Y_{sp} & Y_{ss} \end{bmatrix}. \qquad (C.69)$$

If the transformer has an off-nominal tap ratio $t_H : t_L$ between the primary and secondary windings, the submatrices are modified [10] as follows

- Divide the self-admittance matrix of the primary by $t^2{}_H$
- Divide the self-admittance matrix of the primary by $t^2{}_L$
- Divide the mutual admittance matrices by $t_H t_L$.

NEWTON-RAPHSON METHOD

The N-R method is a traditional algorithm for solving simultaneous non-linear equations. The larger the system, the difficult it becomes to solve a power flow analysis. Hence, this method is used to improve the convergence time.

Consider a function with one variable, such

$$f(x) = 0 \tag{D.1}$$

by applying Taylor series expansion

$$f(x_0 + \Delta x) = f(x_0) + \frac{\partial f}{\partial x}\bigg|_{x_0} \Delta x + \frac{1}{2!}\frac{\partial^2 f}{\partial^2 x}\bigg|_{x_0} (\Delta x)^2 + \cdots + \frac{1}{n!}\frac{\partial^n f}{\partial^n x}\bigg|_{x_0} (\Delta x)^n \tag{D.2}$$

ignoring the second and higher order terms will be

$$f(x_0 + \Delta x) = f(x_0) + \frac{\partial f}{\partial x}\bigg|_{x_0} \Delta x \approx 0 \tag{D.3}$$

The application of Taylor series allows to find the $f(x)$ value for a variable value $x_0 + \Delta x$, where Δx is an infinitesimal increment in function of $f(x_0)$ and its derivatives. The purpose is to find the Δx value to obtain $f(x_0 + \Delta x)$ approximately equal to zero as shown in Fig. D.1.
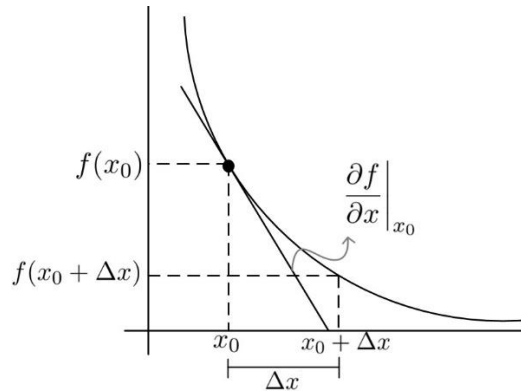
Fig. D.1. Iterative solution for $f(x) = 0$.

Representing (D.3) in matrix form is

$$[J][\Delta x] = -[F(x)] \qquad\qquad (D.\,4)$$

where $[J]$ is the Jacobian matrix of F evaluated at x. (D. 4) defined for simultaneous non-linear equations is expressed as

$$
\begin{bmatrix}
\dfrac{\partial f_1(x)}{\partial x_1} & . & . & . & \dfrac{\partial f_1(x)}{\partial x_n} \\
. & . & & & . \\
. & & . & & . \\
. & & & . & . \\
\dfrac{\partial f_n(x)}{\partial x_1} & . & . & . & \dfrac{\partial f_n(x)}{\partial x_n}
\end{bmatrix}
\begin{bmatrix}
\Delta x_1 \\ . \\ . \\ . \\ \Delta x_n
\end{bmatrix}
= -
\begin{bmatrix}
f_1(x) \\ . \\ . \\ . \\ f_n(x)
\end{bmatrix}.
\qquad (D.\,5)
$$

which when solving, a check for convergence is needed applying $\| f(x_0 + \Delta x_n) \| \le \varepsilon$, where ε is the tolerance. If converged the process ends, otherwise performs another iteration.

APPENDIX E

IEEE 13 NODE TEST FEEDER DATA

Fig. E.1. IEEE 13 Node Test Feeder.

Table E.1. Overhead Line Configurations data IEEE 13 nodes

Configuration	Phasing	Phase (ACSR)	Neutral (ACSR)	Spacing ID
601	B A C N	556,500 26/7	4/0 6/1	500
602	C A B N	4/0 6/1	4/0 6/1	500
603	C B N	1/0	1/0	505
604	A C N	1/0	1/0	505
605	C N	1/0	1/0	510

Table E.2. Underground Line Configuration data IEEE 13 nodes

Configuration	Phasing	Phase (ACSR)	Neutral (ACSR)	Spacing ID
606	A B C N	250,000 AA, CN	None	515
607	A N	1/0 AA, TS	1/0 Cu	520

Table E.3. Line segment data IEEE 13 nodes

Node A	Node B	Length(ft.)	Config.
632	645	500	603
632	633	500	602
633	634	0	XFM-1
645	646	300	603
650	632	2000	601
684	652	800	607
632	671	2000	601
671	684	300	604
671	680	1000	601
671	692	0	Switch
684	611	300	605
692	675	500	606

Table E.4. Transformer data IEEE 13 nodes

	kVA	kV-high	kV-low	R - \%	X - \%
Substation	5,000	115 - D	4.16 Gr. Y	1	8
XFM -1	500	4.16 – Gr.W	0.48 – Gr.W	1.1	2

Table E.5. Capacitor data IEEE 13 nodes

Node	Ph-A (kVAr)	Ph-B (kVAr)	Ph-C (kVAr)
675	200	200	200
611			100
Total	200	200	300

Table E.6. Regulator data IEEE 13 nodes

Regulator ID	1		
Line Segment	650 - 632		
Location	50		
Phases	A-B-C		
Connection	3-Ph,LG		
Monitoring Phase	A-B-C		
Bandwidth	2.0 volts		
PT Ratio	20		
Primary CT Rating	700		
Compensator Settings	Ph-A	Ph-B	Ph-C
R - Setting	3	3	3
X - Setting	9	9	9
Voltage Level	122	122	122

Table E.7. Spot load data IEEE 13 nodes

Node	Load Model	Ph-1 kW	Ph-1 kVAr	Ph-2 kW	Ph-2 kVAr	Ph-3 kW	Ph-3 kVAr
634	Y-PQ	160	110	120	90	120	90
645	Y-PQ	0	0	170	125	0	0
646	D-Z	0	0	230	132	0	0
652	Y-Z	128	86	0	0	0	0
671	D-PQ	385	220	385	220	385	220
675	Y-PQ	485	190	68	60	290	212
692	D-I	0	0	0	0	170	151
611	Y-I	0	0	0	0	170	80
Total		1158	606	973	627	1135	753

Table E.8. Distributed load data IEEE 13 nodes

Node A	Node B	Load Model	Ph-1 kW	Ph-1 kVAr	Ph-2 kW	Ph-2 kVAr	Ph-3 kW	Ph-3 kVAr
632	671	Y-PQ	17	10	66	38	117	68
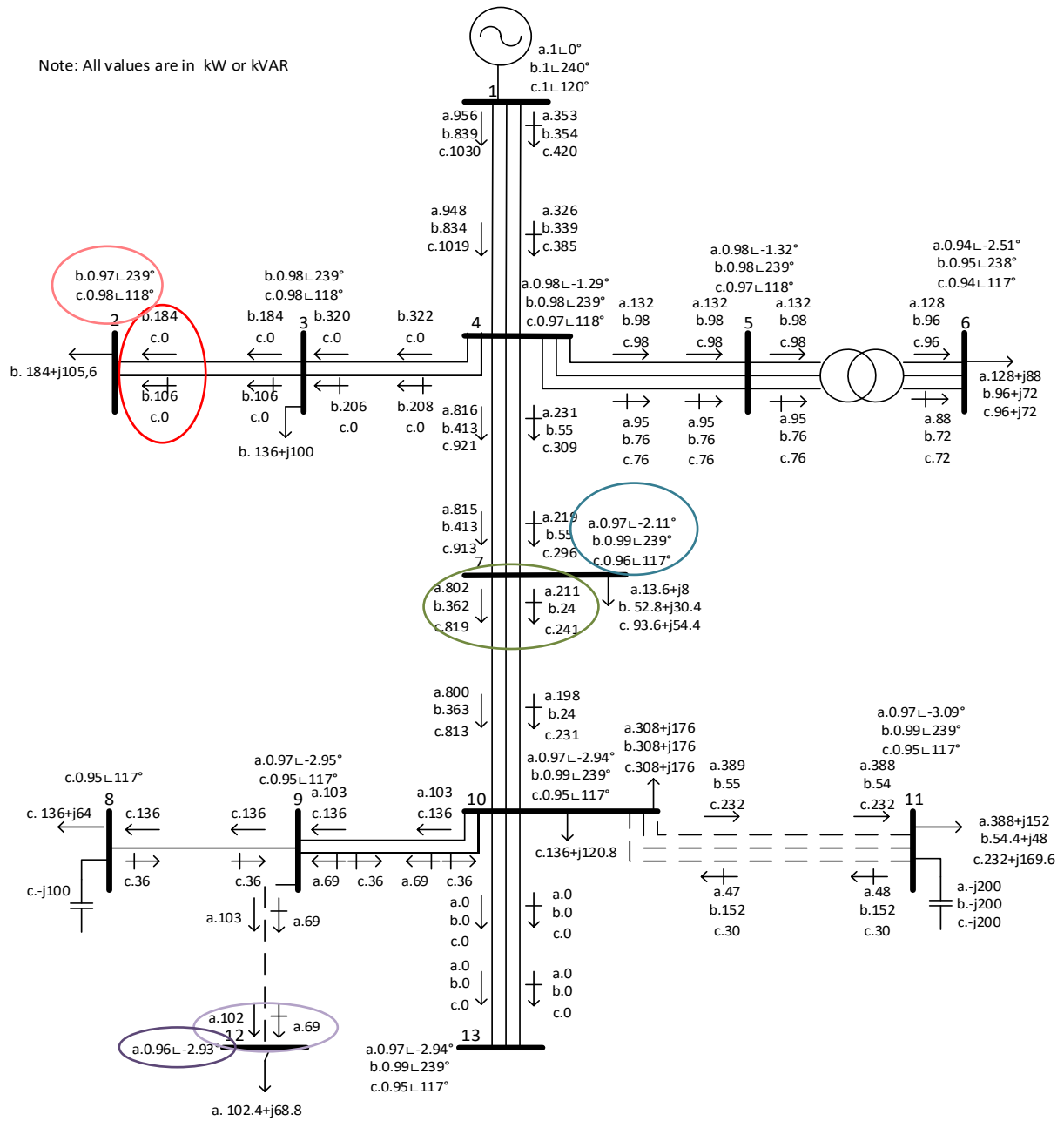
Fig. E.2. IEEE 13-node distribution network, Power flow analysis results from the program developed in MATLAB ®.
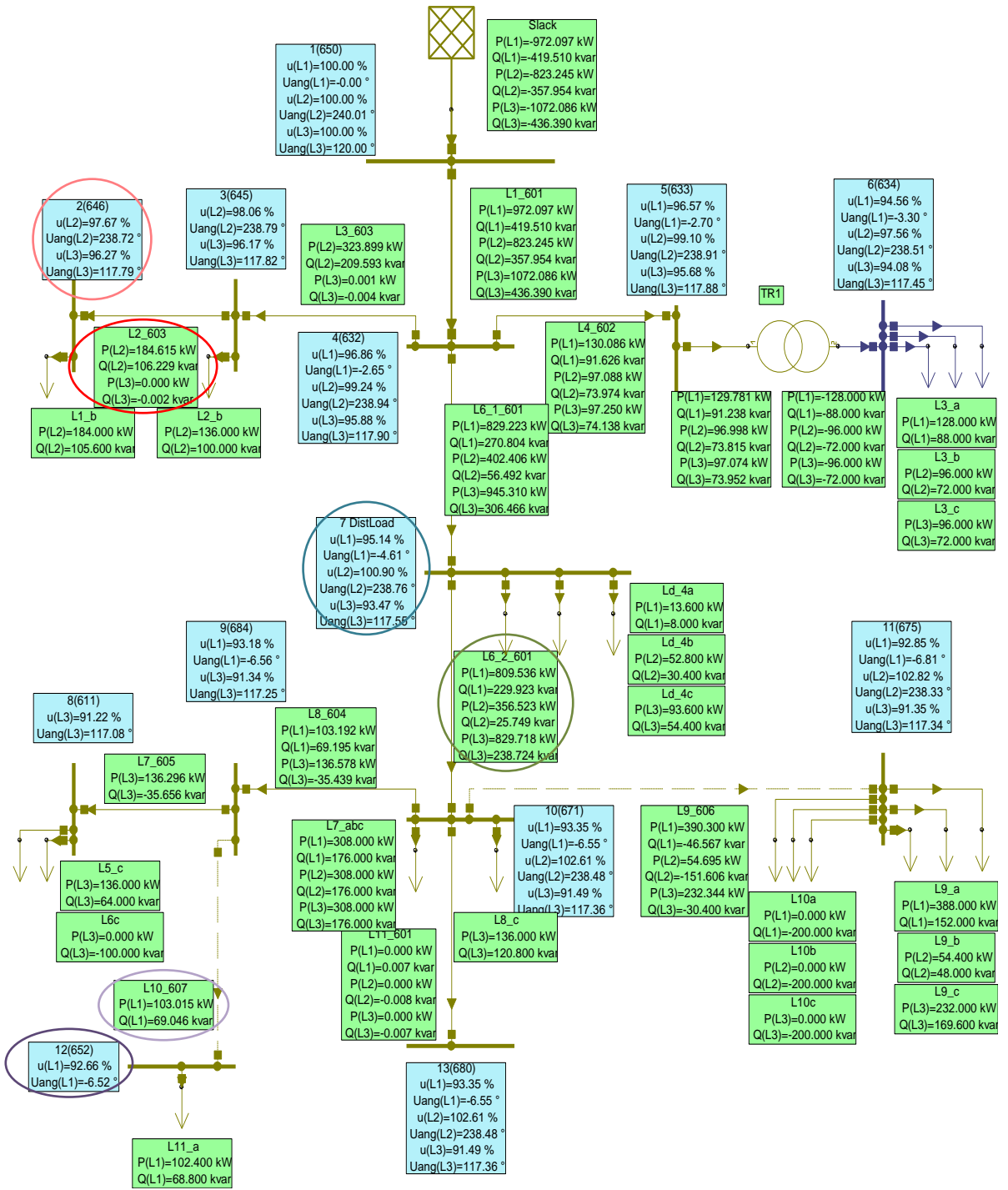
Fig. E.3. IEEE 13-nodes distribution network Power Flow analysis results from NEPLAN ®.

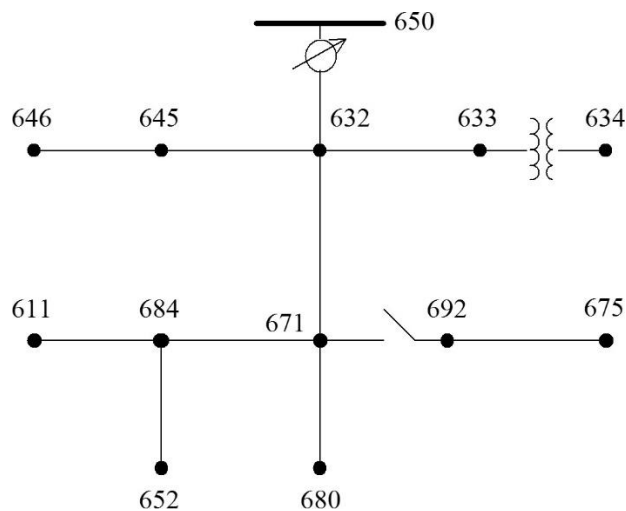# APPENDIX F

IEEE 34 NODE TEST FEEDER DATA
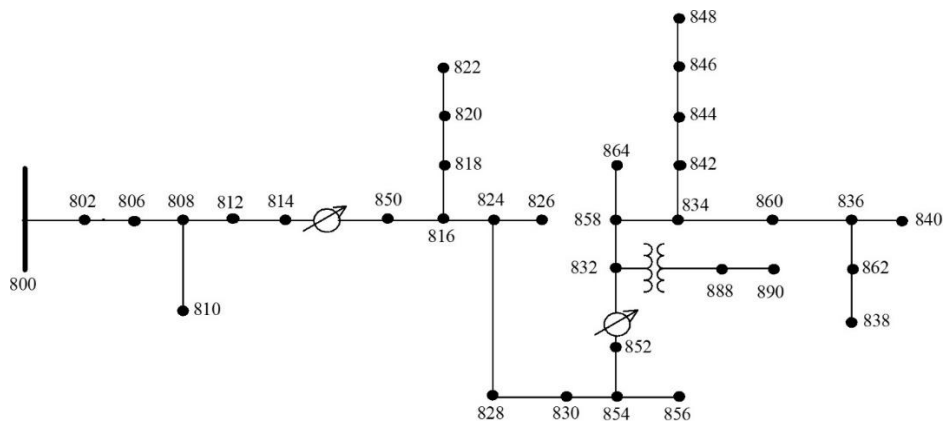
Fig. F.1. IEEE 13 Node Test Feeder.

Table F.1: Overhead Line Configurations data IEEE 34 nodes

Configuration	Phasing	Phase (ACSR)	Neutral (ACSR)	Spacing ID
300	B A C N	1/0	1/0	500
301	B A C N	# 2 6/1	# 2 6/1	500
302	A N	# 4 6/1	# 4 6/1	510
303	B N	# 4 6/1	# 4 6/1	510
304	B N	# 2 6/1	# 2 6/1	510

Table F.2. Transformer data IEEE 34 nodes

	kVA	kV-high	kV-low	R - \%	X - \%
Substation	2500	69 - D	24.9 Gr. W	1	8
XFM -1	500	24.9 – Gr.W	4.16 – Gr.W	1.9	4.08

Table F.3. Line segment data IEEE 34 nodes

Node A	Node B	Length(ft.)	Config.
800	802	2580	300
802	806	1730	300
806	808	32230	300
808	810	5804	303

127

808	812	37500	300
812	814	29730	300
814	850	10	301
816	818	1710	302
816	824	10210	301
818	820	48150	302
820	822	13740	302
824	826	3030	303
824	828	840	301
828	830	20440	301
830	854	520	301
832	858	4900	301
832	888	0	XFM-1
834	860	2020	301
834	842	280	301
836	840	860	301
836	862	280	301
842	844	1350	301
844	846	3640	301
846	848	530	301
850	816	310	301
852	832	10	301
854	856	23330	303
854	852	36830	301
858	864	1620	302
858	834	5830	301
860	836	2680	301
862	838	4860	304
888	890	10560	300

Table F.4. Capacitor data IEEE 34 nodes

Node	Ph-A (kVAr)	Ph-B (kVAr)	Ph-C (kVAr)
844	100	100	100
848	150	150	150
Total	250	250	250

Table F.5. Regulator data IEEE 34 nodes

Regulator ID	1		
Line Segment	814 - 850		
Location	814		
Phases	A-B-C		
Connection	3-Ph,LG		
Monitoring Phase	A-B-C		
Bandwidth	2.0 volts		
PT Ratio	120		
Primary CT Rating	100		
Compensator Settings	Ph-A	Ph-B	Ph-C
R - Setting	2.7	2.7	2.7
X - Setting	1.6	1.6	1.6
Voltage Level	122	122	122
Regulator ID	2		
Line Segment	852 - 832		
Location	852		
Phases	A-B-C		
Connection	3-Ph,LG		
Monitoring Phase	A-B-C		
Bandwidth	2.0 volts		
PT Ratio	120		
Primary CT Rating	700		
Compensator Settings	Ph-A	Ph-B	Ph-C
R - Setting	2.5	2.5	2.5
X - Setting	1.5	1.5	1.5
Voltage Level	124	124	124

Table F.6. Spot load data IEEE 34 nodes

Node	Load Model	Ph-1 kW	Ph-1 kVAr	Ph-2 kW	Ph-2 kVAr	Ph-3 kW	Ph-3 kVAr
860	Y-PQ	20	16	20	16	20	16
840	Y-I	9	7	9	7	9	7
844	Y-Z	135	105	135	105	135	105
848	D-PQ	20	16	20	16	20	16
890	D-I	150	75	150	75	150	75
830	D-Z	10	5	10	5	25	10
Total		344	224	344	224	359	229

Table F.7. Distributed load data IEEE 34 nodes

Node A	Node B	Load Model	Ph-1 kW	Ph-1 kVAr	Ph-2 kW	Ph-2 kVAr	Ph-3 kW	Ph-3 kVAr
802	806	Y-PQ	0	0	30	15	25	14
808	810	Y-I	0	0	16	8	0	0
818	820	Y-Z	34	17	0	0	0	0
820	822	Y-PQ	135	70	0	0	0	0
816	824	D-I	0	0	5	2	0	0
824	826	Y-I	0	0	40	20	0	0
824	828	Y-PQ	0	0	0	0	4	2
828	830	Y-PQ	7	3	0	0	0	0
854	856	Y-PQ	0	0	4	2	0	0
832	858	D-Z	7	3	2	1	6	3
858	864	Y-PQ	2	1	0	0	0	0
858	834	D-PQ	4	2	15	8	13	7
834	860	D-Z	16	8	20	10	110	55
860	836	D-PQ	30	15	10	6	42	22
836	840	D-I	18	9	22	11	0	0
862	838	Y-PQ	0	0	28	14	0	0
842	844	Y-PQ	9	5	0	0	0	0
844	846	Y-PQ	0	0	25	12	20	11
846	848	Y-PQ	0	0	23	11	0	0
Total			262	133	240	120	220	114
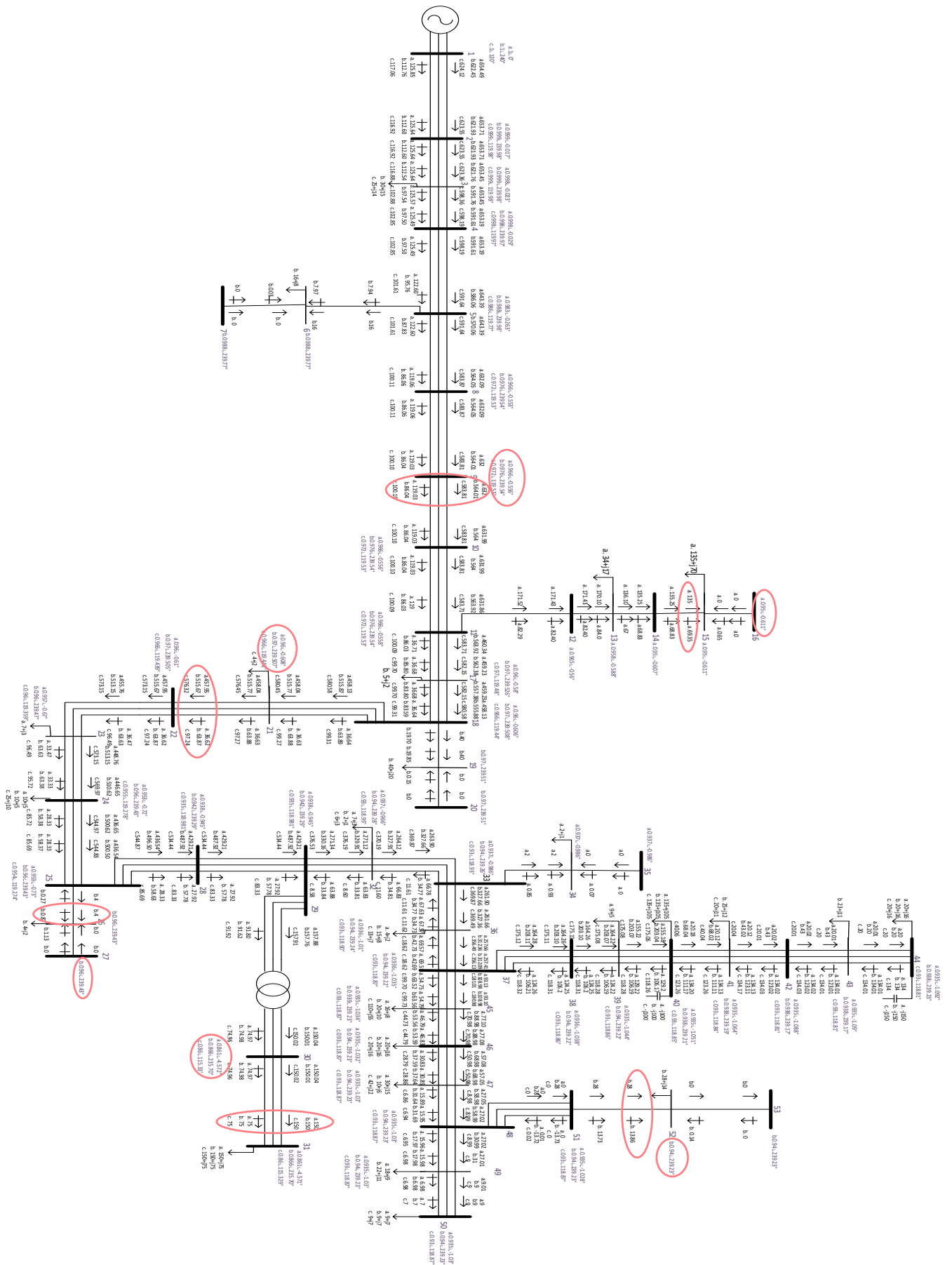
Fig. F.2. Obtained results from coded program in Matlab ® for IEEE 34 Node Test Feeder.

Fig. F.3. IEEE 34-nodes distribution network Power Flow analysis results from NEPLAN ®.

Appendix References

[1]   Danish Wind Industry Association, "Wind Energy Concepts," 2003. [Online]. Available: http://drømstørre.dk/wp-content/wind/miller/windpower web/en/stat/unitsw.htm#roughness. [Accessed: 05-Jul-2017].

[2]   V. . Gertsev and V. . Gertseva, "Classification of mathematical models in ecology," *Ecol. Modell.*, vol. 178, no. 3, pp. 329–334, 2004.

[3]   J. W. Stevenson, D., *Elements of power system analysis*, 4th ed. New York: McGraw-Hill, 1982.

[4]   W. H. Kersting, *Distribution system modeling and analysis*. CRC Press, 2012.

[5]   W. H. Kersting, "Radial distribution test feeders," in *2001 IEEE Power Engineering Society Winter Meeting. Conference Proceedings (Cat. No.01CH37194)*, vol. 2, pp. 908–912.

[6]   C. Acha, Enrique.; Fuerte-Esquivel, Claudio; Ambriz-Pérez, Hugo; Angeles-Camacho, *FACTS : modeling and simulation in power networks*. Wiley, 2004.

[7]   T. A. Short, *Electric power distribution handbook*, 2nd ed. CRC Press, 2014.

[8]   H. A. Smolleck and R. R. Shoults, "A straightforward method for incorporating mutually-coupled circuits into the bus admittance matrix using the concept of artificial branches," *IEEE Trans. Power Syst.*, vol. 5, no. 2, pp. 486–491, May 1990.

[9]   Á. Déri and G. Tevan, "Mathematical verification of Dubanton's simplified calculation of overhead transmission line parameters and its physical interpretation," *Arch. für Elektrotechnik*, vol. 63, no. 4–5, pp. 191–198, Jul. 1981.

[10]   T.-H. Chen, M.-S. Chen, T. Inoue, P. Kotas, and E. A. Chebli, "Three-phase cogenerator and transformer models for distribution system analysis," *IEEE Trans. Power Deliv.*, vol. 6, no. 4, pp. 1671–1681, 1991.

[11]   ABB, "Distribution Automation Handbook. Section 3 Power distribution systems," in *Distribution Automation Handbook*, ABB, 2013, p. 120.

[12]   I. E. S. T. I. ABB Power T & D Company, *Electrical Transmission and Distribution Reference Book*. ABB Power T & D Company, 1997.

[13]   G. F. (George F. . Moore and BICC Cables Ltd., *Electric cables handbook*. Blackwell Science, 1997.

[14]   Jignesh Parmar, "Difference between Power Transformer and Distribution Transformer | EEP," *2011-08-27*, 2011. [Online]. Available: http://electrical-engineering-portal.com/difference-between-power-transformer-and-distribution-transformer. [Accessed: 27-Mar-2017].

[15]   J. H. Harlow, *Electric Power Transformer Engineering, Third Edition*, 3rd ed. CRC Press, 2012.

[16]   M. V. B. U. A. Bakshi, *Transformers & Induction Machines*. Technical Publications, 2009.

[17]   N. D. Tleis, *Power systems modeling and fault analysis : theory and practice*. Elsevier/Newnes, 2008.

[18]   Mo-Shing Chen and W. E. Dillon, "Power system modeling," *Proc. IEEE*, vol. 62, no. 7, pp. 901–915, 1974.

[19]   R. C. Dugan, "Modeling Multi-Winding Transformers," 2013.